Dissertation
submitted to the
Combined Faculties of the Natural Sciences and
Mathematics
of the Ruperto-Carola University of Heidelberg, Germany
for the degree of
Doctor of Natural Sciences

Put forward by
Andrea Bergschneider
Born in Oberviechtach
Oral examination: July 26th, 2017

Strong correlations in few-fermion systems

Strong correlations in few-fermion systems:

In this thesis, I report on the deterministic preparation and the observation of strongly correlated few-fermion systems in single and double-well potentials. In a first experiment, we studied a system of one impurity interacting with a number of majority atoms which we prepared in a single potential well in the one-dimensional limit. With increasing number of majority particles, we observed a decrease in the quasi-particle residue which is in agreement with expectations from the Anderson orthogonality catastrophe. In a second experiment, we prepared two fermions in a double-well potential which represents the fundamental building block of the Fermi-Hubbard model. By increasing the repulsion between the two fermions, we observed the crossover into the antiferromagnetic Mott-insulator regime. Furthermore, I describe a new imaging technique, which allows spin-resolved single-atom detection both in in-situ and in time-of-flight. We use this technique to investigate the emergence of momentum correlations of two repulsive fermions in the ground state of the double well. With the methods developed in this thesis, we have established a framework for quantum simulation of strongly correlated many-body systems in tunable potentials.

Starke Korrelationen in Systemen mit wenigen Fermionen:

Diese Arbeit beschreibt die deterministische Präparation von stark korrelierten Wenig-Teilchen Systemen und deren Untersuchung. Zunächst wurde ein System mit einem Minoritätsteilchen und einer variierenden Anzahl an Majorität-steilchen im eindimensionalen Grenzfall präpariert. Mit steigender Anzahl an Majoritätsteilchen beobachteten wir eine Verringerung des Quasiteilchen-Residuums in Übereinstimmung mit den Erwartungen der Anderson Orthogonal-itätskatastrophe. In einem zweiten Experiment präparierten wir zwei Fermionen in einem Doppelmuldenpotential. Dieses System repräsentiert den fundamen-talen Baustein des fermionischen Hubbardmodells. Durch Vergrößerung der repulsiven Wechselwirkung zwischen den beiden Teilchen konnten wir den Über-gang in den antiferromagnetischen Mott-Isolator-Bereich beobachten. Weiter-hin wird eine neue Abbildungsmethode vorgestellt, die es ermöglicht einzelnen Atome spinaufgelöst sowohl in-situ als auch nach einer Flugzeit zu detektieren. Wir benutzen diese Methode um die Entstehung von Impulskorrelationen zwischen zwei repulsiven Teilchen im Grundzustand eines Doppeltopfes zu untersuchen. Die in dieser Arbeit entwickelten Methoden legen den Grund-stein für die Quantensimulation von stark korrelierten Vielteilchensystemen in einstellbaren optischen Potentialen.

Contents

Chapter 1

Introduction

In Newtonian physics, particles are characterized by a trajectory in phase space that precisely determines the position and momentum of each particle. In quantum mechanics, this deterministic description is replaced by the framework of wave functions. As a consequence assigning trajectories to particles and distinguishing them from each other becomes meaningless. Instead a system which contains many particles has to be described in terms of a many-body wave function.

From the indistinguishability follows two kinds of particles that show different quantum statistics. A system of identical bosons is described by a total wave function that is symmetric under exchange of two particles and consequently a quantum state can be occupied by an arbitrary number of bosons. Identical fermions, however, cannot occupy the same quantum mechanical state – known as Pauli's exclusion principle – as their total wave function is anti-symmetric. Two identical (spinless) particles, for instance, are described by the following wave function

$$\Psi(r_1, r_2) = \frac{1}{\sqrt{2}} \left(\psi(r_1)\phi(r_2) \pm \psi(r_2)\phi(r_1) \right) \tag{1.1}$$

where the upper sign (lower sign) describes bosonic (fermionic) particles and $\psi(r)$ and $\phi(r)$ denote orthogonal single-particle wave functions. In experiments the different exchange symmetries of bosons and fermions result in different correlation function, as first demonstrated by Hanbury Brown and Twiss in 1956 [Han56]. Since then several key discoveries, such as the Bell inequality [Bel64], the Hong-Ou Mandel experiment [Hon87] or the observation of antibunching in single-photon sources [Kim77] and identical fermions [Oli99], have established that correlations lie at the heart of quantum physics.

Despite the required symmetrization of the total wave function, quantum many-body systems without interactions can be described in a simple way. In a metal, for example, where 10^{26} electrons in two different spin states move in a periodic potential formed by the ionic cores, most of the bulk properties can be computed using a single-particle description.

a

$$= \frac{1}{\sqrt{2}} \left(\quad - \quad \right)$$

b
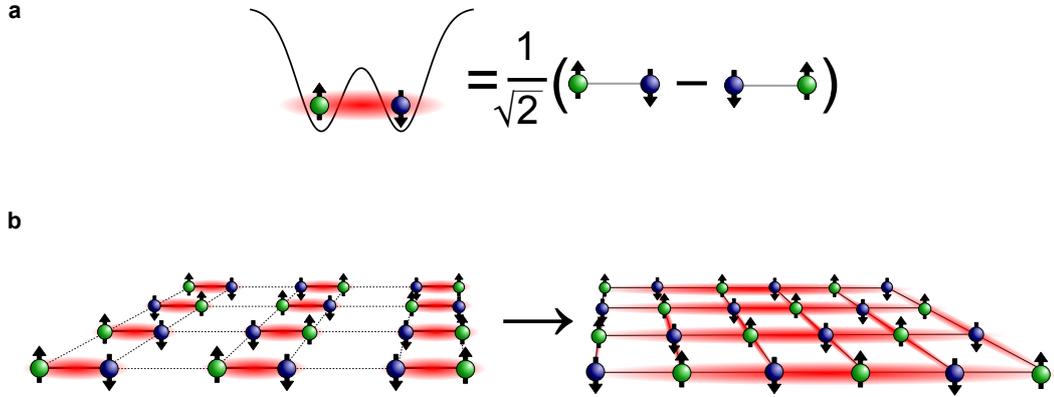
Figure 1.1: Valence-bond state as a building block of solid state systems. a The valence-bond state is a paradigmatic example for a correlated state. Due to its spatially symmetric state, it is energetically favorable compared to a spin triplet. In our experiment, we realize it with two fermions in a double-well potential. **b** It represents the fundamental building block of a dimerized lattice system. By increasing the coupling between the double wells the system crosses the phase transition into an anti-ferromagnetically ordered ground state [Sac08].

When electrons with different spins interact with each other, a description in terms of a single-particle basis is no longer possible as these interactions in addition to the quantum statistics may lead to correlations that are hard to describe. If the wave functions of the particles are overlapping, the correlations become physically relevant, i.e. they alter the energy of the quantum state. A simple system, where these concepts become immediately apparent, is the hydrogen molecule [Hei27]. It consists of two protons that create a double-well potential in which two electrons are confined. The electrons can be described by a two-particle wave function where spin wave function and spatial wave function factorize. This leads to two possible quantum states. If the two electrons arrange in a spin wave function that is symmetric under particle exchange, the spatial part of the wave function is anti-symmetric. If they form a spin singlet where the spin wave function is anti-symmetric, the spatial wave function is symmetric. When calculating the energy of the two possible states, one finds that the spin singlet state has a lower energy which is why the hydrogen molecule is stable.

This so-called valence-bond state is not only relevant to the hydrogen molecule, but also plays a major role in understanding complex phenomena in chemistry and solid state systems [Sac08]. For example, in a system of interacting electrons in a

lattice, valence-bond states are energetically favored. Consequently the ground state of the system is one where the electron spins anti-align which is the essence of quantum magnetism.

The understanding of many-body states in terms of strong correlations is an outstanding problem in these fields [Qui09]. General insight into this complexity can be gained by formulating toy models that contain the essential aspects of the underlying physical processes. For electrons in a lattice, the Hubbard model [Hub63] is a paradigmatic example of such a toy model. It describes fermions moving and interacting in a periodic potential and so it reduces the physics to a competition between the kinetic energy of the fermions and their interaction energy. Despite its simplicity, the Hubbard model exhibits a rich phase diagram and the large complexity makes it hard to solve.

Apart from lattice systems, also bulk materials can exhibit strong correlations. A key example is a system with a single impurity interacting with a surrounding Fermi sea. For weak interaction, this system can be described in terms a quasi-particle that consists of the impurity dressed with the Fermi sea, commonly know as the Fermi polaron. For a spin-imbalanced system with strong interaction, this picture can break down. The system of one impurity in a Fermi sea represents the conceptually simplest realization of a strongly-interacting quantum many-body system.

Solving systems with strong correlations is in general a difficult task. The reason is that their complexity increases exponentially with the number of particles and exceeds the capabilities of classical computers. Instead of simulating the quantum many-body system with a classical computer, one can, as Feynman pointed out [Fey82], approach the problem by building a quantum mechanical system that realizes the Hamiltonian of interest.

Ultracold quantum gases are promising candidates to perform analog quantum simulation. As they use bosonic or fermionic neutral atoms the quantum statistics is inherent in these systems. In addition, they offer excellent control on the interparticle interaction [Chi10] and the trapping potential [Gri00] and many observables can be accessed in the lab even on the single-particle level [Bak09, She10, Omr15, Par15, Che15, Edg15, Hal15, Mir15].

To study interesting phases, for instance in the Hubbard model, low temperatures have to be reached as the relevant mechanisms in these phases have extremely small energy scales. The conventional approach to this problem is to start with a large number of atoms and cool them down using different techniques such as evaporative or sympathetic cooling. However, the temperatures obtained so far have not been low enough to enter the interesting temperature regime and therefore cooling the system to sufficiently low temperatures remains to be a major challenge [McK11].

In our experiment, we take a different approach. Instead of using the complete ensemble, we select a small subset of the system, that has extremely low entropy. From this low-entropy systems we engineer fundamental building blocks of the Hamiltonian of interest. By then merging several building blocks adiabatically, we want to assemble larger systems while maintaining full control on the quantum state.

In this thesis, I will present major steps in this bottom-up approach of preparing fundamental building blocks as well as developing detection methods that can fully characterize all possible correlations in the system.

All our experiments start with the preparation of a well-defined number of particles in a single potential well. Achieving this preparation of fermions in the absolute ground state with a fidelity above 90% delivers quantum systems with extremely low entropy [Ser11b]. In this way we obtain two fermions in the ground state of the potential well forming a spin singlet.

In a first experiment [Mur15b], we realized the fundamental building block of the Hubbard model by adding a second potential well to the system and preparing two fermions in its ground state. By tuning the tunnel coupling and the on-site interaction in the system, we could explore the properties of the ground state in different regimes of the Hubbard model.

In a second experiment, we prepare spin-imbalanced one-dimensional systems of one impurity and a variable number of fermions in a different spin state. In this system, the interaction between the impurity and the majority particles can be described by correlations which lead to the Anderson orthogonality catastrophe in the limit of infinitely many majority particles. We study the emergence of the orthogonality as a function of particle number by measuring the wave function overlap between the interacting and the non-interacting state.

Finally, we developed a new imaging technique to detect the position of individual atoms and resolve their hyperfine state. We combine this new method with an expansion in time-of-flight which allows us to measure the momentum wave function with single-atom resolution. We apply this new imaging technique to a system of two fermions in a double well and extract the full momentum wave function which reveals strong correlations present in the two-site Hubbard model.

In the future we want to prepare several building blocks next to each other and adiabatically assemble larger quantum states. By using the new imaging technique which is easily scalable to larger particle numbers, we aim to study higher-order correlation functions in complex systems and explore the emergence of quantum phases.

Outline

In this thesis, we report on the preparation and detection of strongly correlated systems consisting of few fermionic atoms in one or two potential wells.

- In Chapter 2 we give a theoretical background on correlations functions and introduce the Hubbard model. Furthermore, we explain how interactions can be tuned in systems of ultracold gases and present the influence of a confinement on the interaction energy of few particles.

- In Chapter 3 we explain the basic experimental steps in the preparation, manipulation and detection of few-fermion systems. After that, we give an overview on the apparatus and the optical setup to create multiple potential wells.

- In Chapter 4 we report on a *novel imaging technique*, which allows us to detect single atoms and resolve their hyperfine state. By combining it with an expansion in time-of-flight we can measure the momentum wave function of a prepared quantum state. We use the technique in Chapter 7 to reveal correlations in two-fermion systems.

- In Chapter 5 we present two experimental results on few fermions in a single well using radio-frequency spectroscopy. In the first measurement, we show that two fermions prepared in the ground state of the microtrap form a *spin singlet*. In the second set of experiments, we prepare spin-imbalanced systems consisting of one impurity and an increasing number of majority particles and study the emergence of the *orthogonality catastrophe* in a one-dimensional system.

- In Chapter 6 we realize the fundamental building block of the Hubbard model, that is two fermions in a tunable double-well potential. We characterize the system parameters and prepare the two fermions in overall ground state. We measure the super exchange energy gap and demonstrate our control on the quantum states by driving transitions between the spin singlet and the spin triplet state.

- In Chapter 7 we use our imaging technique to investigate *correlations between two fermions in the double well*. We detect generic correlations between identical fermions and watch the emergence of strong correlations between distinguishable fermions while increasing the interparticle interactions.

- Finally, we summarize the experimental findings and give an outlook on the new possibilities that are available due to the achievements presented in this thesis.

Chapter 2

Strongly correlated fermions in optical potentials

Quantum statistics has a major influence on the physics of many-body systems. Due to the restrictions in the total wave function, bosons behave differently than fermions. The description of these systems is hampered when interparticle interactions lead to additional correlations. The stronger these correlations are, the more intractable the problem becomes.

The simplest model which includes strong correlations is the Hubbard model. Due to its generic nature, it serves as a toy model in many fields from solid-state physics to quantum chromodynamics. It can be realized with ultracold quantum gases in optical lattices, where interparticle interactions can be tuned at will. The unprecedented possibilities of probing quantum gas can help to gain a deeper understanding in correlations and the complex phases that emerge in low-entropy systems.

In Section 2.1 we will first introduce bosons and fermions by explaining the symmetry restrictions on their total wave functions on the example of two particles. In Section 2.2, we present the concept of quantum correlations along the lines of their discovery by Hanbury-Brown and Twiss. These correlations play a major role for the emergence of magnetic phases. In Section 2.3, we introduce the Hubbard model being the paradigmatic model to capture electron-electron correlations. In ultracold quantum gases, these correlated systems are experimentally realized in optical potentials. The technique which allows the introduction of interparticle interaction between neutral particles is presented in Section 2.4.

2.1 Quantum statistics of bosons and fermions

Until the end of the 19th century, massive particles were considered as point-like objects that are localized at a position $\mathbf{x}$ and move with a momentum $\mathbf{p}$. Light, in contrast, was considered as an electromagnetic wave described by Maxwell's

equations. At the beginning of the 20th century, it was realized that light also has particle-like properties. The discovery of the particle-wave duality for light inspired deBroglie in 1924 to postulate the same concept for massive particles. He suggested that the momentum of the particle p is connected with its wavelength λ by the Planck constant $\lambda = h/p$.

Two years later, Schrödinger published an equation [Sch26] that describes the behavior of the postulated matter wave. In that way, a particle can be described in terms of a wave function $\Psi(\mathbf{r}, t)$ by

$$H\Psi(\mathbf{r}, t) = i\hbar \frac{\partial}{\partial t} \Psi(\mathbf{r}, t) \tag{2.1}$$

where H is the Hamiltonian of the system. The eigenstates of the system solve this equation.

Equivalent to the superposition principle for electromagnetic waves, the matter wave can also be in a linear superposition of allowed quantum states

$$\Psi = c_1 \Psi_1 + c_2 \Psi_2 + \dots \tag{2.2}$$

where $\{\Psi_i\}$ form an orthonormal basis and the coefficients c_i are complex numbers.

The wave nature of massive particles can be demonstrated in a double-slit experiment. A single particle is then traveling through the two slits at the same time which leads to an interference of the two paths. On the screen, particles are detected at distinct positions but the measured distribution of many events reveals the interference pattern. In that way, the wave-nature of massive particles has been demonstrated in many beautiful experiments from electrons (e. g.[Ton89]) to large molecules (e. g. [Arn99]).

Exchange symmetry in many-body states

A quantum state Ψ can also describe systems containing more than one particle. If their single-particle wave functions overlap, one cannot distinguish the particles them anymore. This indistinguishability has important consequences on the quantum statistics of the system.

If the particles are considered as indistinguishable, an exchange of two particles shall not change the outcome of a measurement which depends on the absolut square of the wave function. Therefore the only thing that can change is the sign of the wave function. From this follows two different kinds of particles.

For *Bosons*, which carry an integer spin, the total wave function Ψ is symmetric under exchange of two particles

$$\Psi_B(..., x_m, ..., x_n, ...) = +\Psi_B(..., x_n, ..., x_m, ...) \quad . \tag{2.3}$$
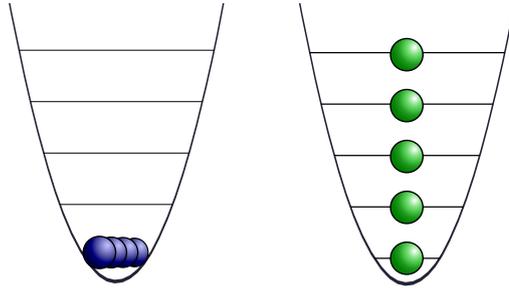
Figure 2.1: Quantum statistics of bosons and fermions. Based on the exchange symmetry of the total wave function one distinguishes two kinds of particles with different quantum statistics. *Bosons* (left) have a symmetic total wave function and can therefore all occupy the same quantum state in the system. For *fermions* (right) the Pauli principle applies, which states that a quantum state can never be occupied by more than one fermion.

As a consequence, several bosons can occupy the same mode. At low enough temperatures, a macroscopic occupation of the same mode leads to the formation of a Bose-Einstein condensate.

Particles with half-integer spin are called *Fermions*. Their total wave function is anti-symmetric under particle exchange

$$\Psi_F(..., x_m, ..., x_n, ...) = -\Psi_F(..., x_n, ..., x_m, ...). \tag{2.4}$$

This anti-symmetry of the total wave function is the origin of the Pauli exclusion principle where one mode can be at most occupied by one fermion. The total wave function for N identical fermions that occupy N different single-particle modes ψ_i can be constructed using the Slater determinant[1]. For instance, the total wave function of two identical fermions can be written as

$$\Psi_F(1, 2) = \frac{1}{\sqrt{2}} \left(\psi(1)\phi(2) - \psi(2)\phi(1) \right) \tag{2.5}$$

where ψ and ϕ describe two orthogonal single-particle wave functions. They can for example describe spatial wave functions of single particles. Calculating the probability density of the two-fermion state reveals that the probability to find the fermions at the same position vanishes.

---

[1]Based on the total anti-symmetry of the many-body wave function of fermions, Dirac and Fermi independently derived the Fermi-Dirac distribution that describes the occupation of energy modes at low temperatures. We will utilize it to prepare few-fermion systems, presented in Chapter 3

	Spatial wave function Φ	Spin wave function χ	
$\Phi^{(S)}$	$\|\phi_1\phi_1\rangle$ $\frac{1}{\sqrt{2}}\left(\|\phi_1\phi_2\rangle + \|\phi_2\phi_1\rangle\right)$ $\|\phi_2\phi_2\rangle$	$\frac{1}{\sqrt{2}}\left(\|\uparrow\downarrow\rangle - \|\downarrow\uparrow\rangle\right)$	$\chi^{(A)}$
$\Phi^{(A)}$	$\frac{1}{\sqrt{2}}\left(\|\phi_1\phi_2\rangle - \|\phi_2\phi_1\rangle\right)$	$\|\uparrow\uparrow\rangle$ $\frac{1}{\sqrt{2}}\left(\|\uparrow\downarrow\rangle + \|\downarrow\uparrow\rangle\right)$ $\|\downarrow\downarrow\rangle$	$\chi^{(S)}$

Table 2.1: Possible combinations of spatial and spin wave function for two non-interacting fermions. For two particles the spatial and the spin wave function can be symmetric (S) or anti-symmetric (A). For two fermions with two possible spin degrees of freedom $\|\uparrow\rangle$ and $\|\downarrow\rangle$ as well as two different spatial modes $\phi_{1,2}$ the following six combinations are possible. The first row corresponds to a spin singlet and the second row describes a spin triplet configuration. Taken from [Foo11]

Spatial and spin degree of freedom

A quantum state can have several degrees of freedom that are described by a set of quantum numbers. Examples for this are the spatial modes or the spin degree of freedom. As the exchange symmetry applies to all quantum numbers, the introduction of a certain symmetry in one degree of freedom also has an influence on the symmetry in another degree of freedom.

Electrons, for example, can be described by a spatial wave functions and have a spin of $s = 1/2$. The spin can take two different projections $m_s = \pm 1/2$ which we denote as $\|\uparrow\rangle$ and $\|\downarrow\rangle$. In absence of a coupling between spin and spatial degree of freedom, we can write the total wave function of two particles as a product of the spatial Φ and the spin wave function χ

$$\Psi = \Phi(\mathbf{x_1}, \mathbf{x_2})\chi_{1,2} \tag{2.6}$$

As electrons are fermions, their total wave function has to be anti-symmetric. This can be achieved in two different ways. Either a symmetric spatial wave function is combined with an anti-symmetric spin wave function $\Phi^{(S)}\chi^{(A)}$, or an anti-symmetric spatial wave function with a symmetric spin wave function $\Phi^{(A)}\chi^{(S)}$. Table 2.1 shows the possible combinations of spatial and spin wave function for two fermions. Similarly, for two bosons the spatial and spin wave function have to be either both symmetric or anti-symmetric.

In our experiment, we can prepare all of these combinations. We use fermionic neutral atoms in two different hyperfine states which correspond to two different

spin states. The two particles can then occupy the two different wells in a double-well potential.

2.2 Correlations in quantum systems

The consequence of quantum statistics can be observed in many systems. The best example, where the Pauli exclusion principle governs the system, is the occupations of electronic shells in an atom[2]. Only much later, the quantum statistics of photons was directly observed in an experiment by Hanbury Brown and Twiss which led to the birth of a the field of quantum optics. Their observation of two-particle correlations is nowadays used in various fields [Bay98].

2.2.1 Hanbury-Brown Twiss effect for photons

The interference of light was known since the experiments of Young [You02]. Already at the end of the 19th century, it was for example used to measure the size of stars [Fox06]. In a so-called Michelson stellar interferometer light of a bright star is captured with two mirrors that have a large distance to each other and is then directed towards two slits. If the light is spatially coherent, one observes an interference pattern on a screen. By studying the visibility of this interference pattern as a function of the distance between the two mirrors one can infer the angular spread of the light source.

The resolution of this method is proportional to the distance of the two mirrors. To observe the interference pattern, the phase difference has to be very stable. Mechanical instabilities therefore limit the resolution of the interferometer. To circumvent this problem, Hanbury Brown and Twiss developed a new scheme to measure the coherence of light.

Instead of comparing the amplitudes at different points by interference, they measured the light intensity at both detectors and correlated the electronic signal. In this way, they observed the star Sirius with two spatially separated parabolic mirrors that focused the light of Sirius onto two photomultipliers [Han56] and measured the normalized correlation for several different distances. They could observe that the correlation decreased when increasing the distance and could conclude that the decrease of the correlations was consistent with the known size of Sirius.

---

[2]It was actually this observation, based on spectroscopic data, that inspired Pauli to suggest what was later called the Pauli exclusion principle. Only later, it was shown, that it has a physical basis.
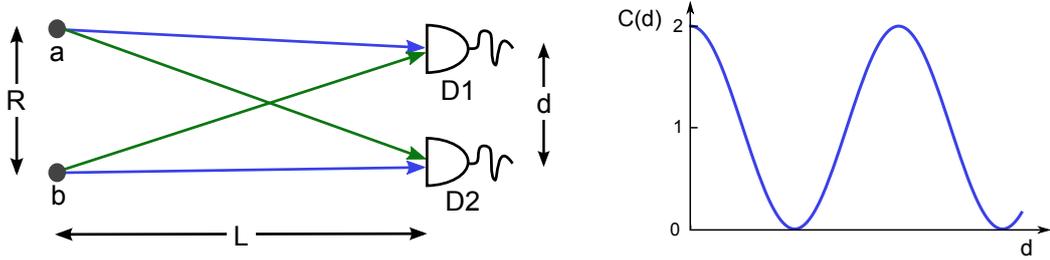
Figure 2.2: Setup of the Hanbury Brown-Twiss experiment. Two electromagnetic waves travel from two points a and b towards two detectors $D1$ and $D2$ where they incident. By calculating the correlation between the two detected intensities one obtains an oscillating normalized correlation function $C(d)$.

Hanbury Brown and Twiss observation is expected for a classical description of light. As shown e. g. in [Bay98] one can simply assume that two electromagnetic waves are traveling from two points a and b towards two detectors $D1$ and $D2$, as shown in Figure 2.2 where the amplitudes of the waves can be described as spherical wave. Originating from point a follows the expression $\alpha \mathrm{e}^{ik|\mathbf{r}-\mathbf{r}_a|+i\phi_a}/|\mathbf{r}-\mathbf{r}_a|$ and from point b the wave propagates like $\beta \mathrm{e}^{ik|\mathbf{r}-\mathbf{r}_b|+i\phi_b}/|\mathbf{r}-\mathbf{r}_b|$, where ϕ_a and ϕ_b are random phases of the thermal source. On each detector, both waves are incident. The resulting intensity on detector $D1$ can be written as

$$I_1 = \frac{1}{L^2}\left(|\alpha|^2 + |\beta|^2 + \alpha^*\beta \mathrm{e}^{i(k(r_{1b}-r_{1a})+\phi_b-\phi_a)} + \alpha\beta^* \mathrm{e}^{-i(k(r_{1b}-r_{1a})+\phi_b-\phi_a)}\right) \quad (2.7)$$

where r_{1a} describes distance from the source a to the detector $D1$. The intensity for the detector $D2$ can be written similarly. When we average the signal over time, the randomly fluctuating phases vanish and we are left with the simple expression for the intensity on detector $D1$ which is not varying with the distance between the detectors

$$\langle I_1 \rangle = \frac{1}{L^2}\langle(|\alpha|^2 + |\beta|^2)\rangle. \quad (2.8)$$

The correlation between the two signals can be calculated by $\langle I_1 I_2 \rangle$. Performing the averaging over time after the multiplication leads to an additional term such that the normalized correlation function can be written as

$$C(d) = \frac{\langle I_1 I_2 \rangle}{\langle I_1 \rangle \langle I_2 \rangle} = 1 + 2\frac{\langle|\alpha|^2\rangle \langle|\beta|^2\rangle}{(\langle|\alpha|^2\rangle + \langle|\beta|^2\rangle)^2}\cos(k(r_{1a} - r_{2a} - r_{1b} + r_{2b})). \quad (2.9)$$

We can simplify the expression above by assuming that the distance between the light source and the detector L is much larger than the distance between the two

observed points of the star R and obtain $k(r_{1a} - r_{2a} - r_{1b} + r_{2b}) \to \mathbf{R}(\mathbf{k_2} - \mathbf{k_1})$. The wave vector of the light incident on the detector D_i is denoted by $\mathbf{k_i}$.

Consequently, the normalized correlation function depends on the distance between the two detectors and for very small distances, it can reach a maximum value of 2. To model the correlation function of a star, one rather assumes a distribution of light sources [Bay98]. The resulting correlation function for this distribution turns out to be the Fourier transform of the source distribution. Consequently, for distances of the two detectors, that are larger than the coherence length, the correlation function decreases towards 1, which is equivalent to uncorrelated light.

2.2.2 Quantum theory of correlation functions

When Hanbury Brown and Twiss published their findings, the community was puzzled because their observation seemed to not be compatible with the existence of individual photons. After an explanation following a semiclassical picture [Pur56], Glauber developped a formalism based on the language of quantum field theory that described the photon field in terms of propagation modes [Gla62, Gla63a, Gla63b] and could explain the observation of Hanbury Brown and Twiss. But more than that, it led to the development of quantum optics. In the following, we present quantum field theoretical formalism to describe correlation functions following the notation of [CT11].

In quantum field theory, many-particle states are described in the so-called Fock space where $\{|\phi_\alpha\rangle\}$ is an orthonormal single-particle basis. The Fock basis can then be written as $|\ldots n_\alpha \ldots n_\beta \ldots\rangle$ where n_α defines the occupation number of the single-particle state $|\phi_\alpha\rangle$. For bosons the Fock state consists of non-negative integer occupations. For fermions, at most one particle occupying the state is allowed, i.e. $n_\alpha = 0$ or $n_\alpha = 1$.

One then introduces creation and annihilation operators $\hat{a}_\alpha^\dagger$ and $\hat{a}_\alpha$ that act on the single-particle state ϕ_α. To account for the bosonic and fermionic quantum statistics of the state, one defines the commutation relations

$$\left[\hat{a}_\alpha , \hat{a}_\beta^\dagger\right]_\mp = \delta_{\alpha\beta}, \quad \text{and} \quad \left[\hat{a}_\alpha , \hat{a}_\beta\right]_\mp = \left[\hat{a}_\alpha^\dagger, \hat{a}_\beta^\dagger\right]_\mp = 0 \qquad (2.10)$$

where $[\hat{A}, \hat{B}]_\mp = \hat{A}\hat{B} \mp \hat{B}\hat{A}$ denotes the commutation and anti-commutation relations for bosons and fermions respectively.

Combining the single-particle basis states and the annihilation and creation operators, one can introduce field operators $\hat{\Psi}^\dagger(\mathbf{r})$ and $\hat{\Psi}(\mathbf{r})$ that play the role of creation and annihilation operators for particles at position $\mathbf{r}$

$$\hat{\Psi}^\dagger(\mathbf{r}) = \sum_\alpha \phi_\alpha^*(\mathbf{r})\,\hat{a}_\alpha^\dagger \quad \text{and} \quad \hat{\Psi}(\mathbf{r}) = \sum_\alpha \phi_\alpha(\mathbf{r})\,\hat{a}_\alpha \qquad (2.11)$$

with $\phi_\alpha^* = \langle \phi_\alpha | \mathbf{r} \rangle$. It is straight forward to show that the field operators satisfy the commutation relations presented before.

From the field operators one can directly construct the spatial density operator $n(\mathbf{r_0}) = \hat{\Psi}^\dagger(\mathbf{r_0}) \hat{\Psi}(\mathbf{r_0})$ and its average value, as well as the average spatial density correlator $\langle n(\mathbf{r}, \mathbf{r}') \rangle$ which is the first-order spatial correlation function

$$G^{(1)}(\mathbf{r}, \mathbf{r}') = \langle \hat{\Psi}^\dagger(\mathbf{r}) \hat{\Psi}(\mathbf{r}') \rangle \tag{2.12}$$

To calculate the probability to find one particle at position $\mathbf{r}$ and the second one at position $\mathbf{r}'$, one uses the second-order spatial correlations function

$$G^{(2)}(\mathbf{r}, \mathbf{r}') = \langle \hat{\Psi}^\dagger(\mathbf{r}) \hat{\Psi}^\dagger(\mathbf{r}') \hat{\Psi}(\mathbf{r}') \hat{\Psi}(\mathbf{r}) \rangle \tag{2.13}$$

The normalized versions of the density-density correlation functions are defined like

$$g^{(2)}(\mathbf{r}, \mathbf{r}') = \frac{\langle \hat{\Psi}^\dagger(\mathbf{r}) \hat{\Psi}^\dagger(\mathbf{r}') \hat{\Psi}(\mathbf{r}') \hat{\Psi}(\mathbf{r}) \rangle}{\langle \hat{\Psi}^\dagger(\mathbf{r}) \hat{\Psi}(\mathbf{r}) \rangle \langle \hat{\Psi}^\dagger(\mathbf{r}') \hat{\Psi}(\mathbf{r}') \rangle} \tag{2.14}$$

In a similar way, higher correlation functions have been defined. They are used to characterize the correlations between more than two particles.

To understand why Hanbury Brown and Twiss detected intensity correlations, one can consider two identical photons at positions a and b, similar to Figure 2.2. In the Fock basis, the state can be written as $\hat{a}_b^\dagger \hat{a}_a^\dagger |0\rangle$. The propagation along L which is much larger than their distance R corresponds to a fourier transform of the spatial state such that in the detection plane, the photons are described by their initial momentum distribution and the probability distributions of the photons overlap.

To calculate the two-point correlation function, we use the annihilation and creation operators in momentum space

$$\hat{b}_i = \sum_j e^{ik_i x_j} \hat{a}_j \tag{2.15}$$

where $\hat{a}_j$ ($\hat{a}_j^\dagger$) denotes the annihilation (creation) operator in real space. Inserting this into 2.13 results in a sum with exponential terms and a combination of annihilation and creation operators which can be rewritten [Rom09] using the commutation relation

$$\langle \hat{a}_j^\dagger \hat{a}_k^\dagger \hat{a}_l \hat{a}_m \rangle = \delta_{jm}\delta_{kl} \langle n_j \rangle \langle n_k \rangle + \delta_{jl}\delta_{km} \langle n_j \rangle \langle n_k \rangle - \{\langle n_j \rangle (\delta_{jk}\delta_{jl}\delta_{jm} + \delta_{jk}\delta_{jl}\delta_{jm})\}. \tag{2.16}$$

The first and the second term describe the direct detection and the exchanged detection of the two photons in the two detectors. In Figure 2.2 the two terms are

shown as the blue and green paths. As a consequence, the second term carries the information about the exchange symmetry of the two particles. The third term will be neglected as it only adds an offset.

Inserting this result into equation 2.14 and considering only the relative distances $d = \mathbf{r} - \mathbf{r}'$ results in an expression that is very similar to equation 2.9. For two photons with $\langle n_a \rangle = \langle n_b \rangle = 1$, we obtain a one-dimensional correlation function of

$$C(d) = 1 + \left[\frac{1}{2} + \frac{1}{2} \cos(\Delta k \, d) \right]. \tag{2.17}$$

The observation of photon bunching in the Hanbury Brown-Twiss experiment can be understood as a result of the symmetric spatial wave function of the photons. In case of two identical fermions, the term in brackets in equation 2.17 would be negative. As a consequence, one expects anti-bunching for identical fermions.

Fermionic antibunching was first observed in the form of current fluctuations in an electron system [Oli99] and later shown for free electrons in an experiment similar to the setup that Hanbury Brown and Twiss used [Kie02]. With the creation of ultracold quantum gases, correlation functions became an important experimental tool in quantum many-body physics. The demonstration of bosonic bunching and fermionic antibunching was revisited in free space [Sch05, Jel07] and noise correlation analysis allowed to extract two-point correlation functions from cold bosonic and fermionic atoms in periodic potentials [Fö05, Rom06].

The last experiments were based on the motivation that the analysis of correlation functions allows to describe quantum many-body states. These states, consisting of a number of particles become extremely challenging to describe, if the particles do not only obey the quantum statistics but also interact with each other. A full description of the quantum many-body function of such a complex state requires an exponentially large amount of information. Alternatively, one can, similar to the work of Glauber, use the language of quantum field theory and express the quantum state in terms of all possible multi-particle correlation functions [Hod11, Fan16, Hod17, Sch17] to characterize the strongly correlated many-body state.

2.3 From correlations to quantum magnetism

In many systems the physical behavior can be captured by a single-particle description. For example, if electrons are moving in a shallow periodic potential created by the ions in a crystal, their mean free path is large. So the electrons can be considered as non-interacting and every electron moves independently through the lattice. However, if the periodic potential created by the ions is deep, as it is

the case in transition metals, the Coulomb repulsion between the electrons has to be taken into account and a many-body description is required.

The description of a solid-state system is simplified by using models that only contain the basic ingredients. The simplest model that describes interacting electrons which move in a periodic potential, is the Hubbard model [Hub63]. The motion of the electrons is discretized and described by a hopping term and the particles are only interacting if they occupy the same site. The interplay between the kinetic energy and interaction energy leads to strong correlations which are of non-local nature. The correlations are the reason why the Hubbard model is still not completely solved.

The Hubbard model is of high interest in condensed matter physics. At low enough temperatures and half filling (one electron per ion) it exhibits an anti-ferromagnetic phase [Aue98]. Away from half filling, it is still an open question whether the model can capture d-wave superconductivity. To answer this quesion, one wants to use quantum simulation.

In the following, we will first introduce the Hubbard model for fermions and explain the mechanism that is responsible for quantum magnetism before we come to the approach of using analog quantum simulators to solve the Hubbard model.

2.3.1 The Hubbard model

The Hubbard model is the simplest model to describe strongly-correlated systems. It was suggested in 1963 [Hub63] in the context of condensed matter physics to describe the properties of transition metals where the valence electrons occupy the d and f orbitals. Electrons in these orbitals feel a deep periodic potential from the ionic cores. This gives rise to narrow energy bands. As a consequence, the Coulomb interaction between electrons is not negligible anymore and causes electron correlations.

Due to is paradigmatic role, the Hubbard model plays a central role in the theoretical description of many-body system in different fields [Qui09] and thus a lot of literature is available on this subject. Here, we introduce the simplest version of the Hubbard model following [Aue98].

The system of valence electrons that move in a periodic potential and interaction with each other can be described by the following Hamiltonian which consists of two parts

$$H = H_{\text{crystal}} + H_{\text{int}} \tag{2.18}$$

The first term H_{crystal} denotes the single-particle Hamiltonian containing the kinetic energy term and the periodic potential due to the ionic crystal[3]. The second term

---

[3]$H_{\text{crystal}} = -\frac{\hbar^2}{2m}\nabla^2 + V^{\text{ion}}(\mathbf{x})$
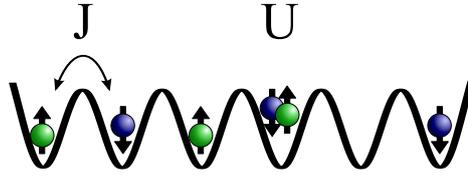
Figure 2.3: Schematic of the Hubbard Model. The description of fermions in two different spin states, indicated in blue and green, moving in a periodic potential is reduced to two parameters, the tunnel coupling J and the on-site interaction U. The interplay between these two processes leads to strong correlations and a rich phase diagram.

H_{int} denotes the screened Coulomb interaction involving two electrons[4].

First, we take a look at the solution of the Hamiltonian without the interaction term. Due to the periodicity of the underlying potential, we choose periodic functions $\phi_{\alpha\mathbf{k}}(\mathbf{x})$ as a basis. The periodic potential leads to a band structure where α indexes the individual bands. As the potential depth is large, the bands are narrow in energy. For this reason, the particles are localized to the positions of the ions. We can therefore describe the localized electrons using the orthogonal Wannier basis

$$\phi_{\alpha i}(\mathbf{x}) = \frac{1}{\sqrt{\mathcal{N}}} \sum_{\mathbf{k}} \mathrm{e}^{-i\mathbf{k}\mathbf{x_i}} \phi_{\alpha\mathbf{k}}(\mathbf{x}) \tag{2.19}$$

where $\mathcal{N}$ denotes the number of lattice sites, α is band index, i index of lattice site. In a deep lattice, one can use the *tight-binding approximation* and the Wannier states can be approximated by a set of states localized at the position of one ion $\phi_i(\mathbf{x}) = \phi_\alpha(\mathbf{x} - \mathbf{x_i})$. These approximated Wannier states are not orthogonal anymore. However, they simplify the calculations. Additionally, we restrict the Hubbard model to the lowest band $\alpha = 0$. This is justified as long as the Fermi energy lies within this single band.

From the Wannier function and the creation and annihilation operators, one constructs the field operators

$$\hat{\psi}_\sigma^\dagger(\mathbf{x}) = \sum_i \phi_i^*(\mathbf{x}) \, \hat{a}_{i\sigma}^\dagger \tag{2.20}$$

where $a_{i\sigma}^\dagger$ and $a_{i\sigma}$ obey the anti-commutation rules for fermions (see Section 2.2.2) and σ denotes the spin degree of freedom. Using the field operators we can write

---

[4]H_{int} denotes an interaction term. In general this can be Coulomb interaction or also short-range interaction.

the Hubbard Hamiltonian

$$H = -J \sum_{\sigma,\langle i,j \rangle} a_{i\sigma}^\dagger a_{j\sigma} + U \sum_j n_{j\downarrow} n_{j\uparrow} \tag{2.21}$$

where $\langle \rangle$ denotes the summation over adjacent sites and $n_{j\sigma} = a_{j\sigma}^\dagger a_{j\sigma}$ is the occupation number operator. The first term of the Hamiltonian H_J describes a particle hopping from site j to the neighboring site i and the second term H_U describes the interaction energy, if two particles occupy the same site. The Hubbard parameter J and U can be calculated by

$$J = \int \phi_i^*(\mathbf{x}) H_{\text{crystal}}\, \phi_j(\mathbf{x})\, \mathrm{d}\mathbf{x} \tag{2.22}$$

$$U = \iint |\phi_i(\mathbf{x_1})|^2 H_{\text{int}}\, |\phi_i(\mathbf{x_2})|^2\, \mathrm{d}\mathbf{x_1}\mathrm{d}\mathbf{x_2} \tag{2.23}$$

The competition between the kinetic and the interaction term dictates the quantum phases in the Hubbard model. In the limit of no interaction between the fermions, the metallic phase of a free-electron gas is recovered. For increasing interaction and half filling (in average one fermion per lattice site) the interaction energy suppresses the occupation of one lattice site by more than one particle. If $U \gg J$ this leads to an insulating phase where each site is occupied by exactly one fermion which is known as the *Mott insulator*. We will see in the next section that for low temperature $k_{\text{B}} T < J^2/U$, the system shows anti-ferromagnetic ordering.

In the limit of large interaction strength $U \gg J$, the Hubbard model at half filling can be reduced to the Heisenberg model with the spin-spin coupling driven by the super exchange. Away from half filling, the so-called *t-J*-model describes the physics[5]. Currently, it is subject of intense investigation in the context of high-tc super conductivity.

2.3.2 Superexchange driving magnetic correlations

Magnetism is characterized by the collective ordering of the magnetic moments of many electrons in a material. The mechanism behind this ordering cannot be explained by the dipole-dipole interaction as it is much too weak. Instead it is a mechanism called *exchange* that can give rise to magnetic phases.

To understand this mechanism [Blu01], we consider two electrons pinned at two different points in space x_1 and x_2. As already mentioned in Section 2.1, the total

---

[5]The name originated in the condensed-matter community, where t is used for the tunnel coupling and J denotes the spin-spin coupling in the Heisenberg model. In the community of ultracold quantum gases, however, t is used for the time.

wave function of the two fermions has to be anti-symmetric which leads to two different possibilities

$$\Psi_S = \frac{1}{\sqrt{2}} \left(\psi_a(\mathbf{r_1})\psi_b(\mathbf{r_2}) + \psi_a(\mathbf{r_2})\psi_b(\mathbf{r_1}) \right) \chi_S \qquad (2.24)$$

$$\Psi_T = \frac{1}{\sqrt{2}} \left(\psi_a(\mathbf{r_1})\psi_b(\mathbf{r_2}) - \psi_a(\mathbf{r_2})\psi_b(\mathbf{r_1}) \right) \chi_T \qquad (2.25)$$

where $\psi(\mathbf{r})$ describes the orbital single-particle wave function. χ_T describes the spin wave function of aligned spins with the total spin $S = 1$ (triplet) and χ_S describes the anti-aligned singlet spin wave function with $S = 0$.

We calculate the energy expectation value of the two states E_S and E_T using the Hamiltonian given in equation 2.18. As the Hamiltonian is not acting on the spin wave function, the difference in the energies is only dependent on the spatial wave functions. The *exchange integral* can be written as

$$E_S - E_T = 2 \iint \psi_a^*(\mathbf{r_1})\psi_b^*(\mathbf{r_2})H\psi_a(\mathbf{r_2})\psi_b(\mathbf{r_1}) \, \mathrm{d}\mathbf{r_1}\mathrm{d}\mathbf{r_2} \,. \qquad (2.26)$$

Depending on the specific situation either the singlet or the triplet state has the lower energy. For two electrons at separate locations one finds that the symmetric spatial wave function is lower in energy as it lowers the kinetic energy in the system. Consequently, the spins of two fermions are anti-aligned[6] and the ground state favors anti-ferromagnetic coupling. This behavior has first been described for the H_2-molecule by Heitler and London [Hei27].

We can express the alignment of the magnetic moments with an effective spin Hamiltonian [Aue98] where the energy difference $E_S - E_T$ due to the exchange plays the role of the spin coupling J^{ex}. A generalization for this model to more then two particles leads to the Heisenberg model.

$$H = -\sum_{i,j} J_{ij}^{ex}\mathbf{S}_i \cdot \mathbf{S}_j \qquad (2.27)$$

where i and j are describing the location of the spins and J_{ij}^{ex} is the coupling between the ith and the jth spin.

We want to use the Hubbard model to calculate the spin coupling constant that favors the anti-ferromagnetic alignment of the spins. The Heisenberg model becomes the effective model for large on-site interaction. If the interaction term H_U is much larger than the kinetic term H_J in the Hamiltonian, we can use second order perturbation theory to calculate the size of the spin-spin coupling. To simplify the

---

[6]For two bosons, the parallel alignment of the two spins in a triplet spin wave function is favored.
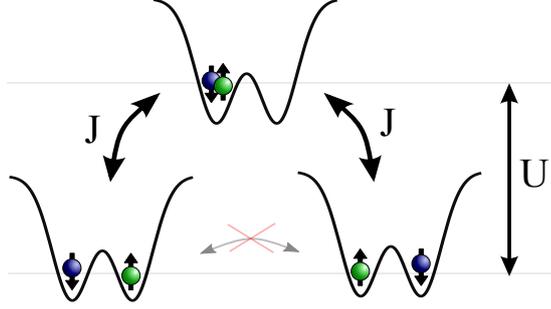
Figure 2.4: Super exchange mechanism in a two-site Hubbard model.
Strong interparticle interaction leads to single occupancy of the individual
sites in the lattice, as tunneling to the neighboring site is off-resonant by the
interaction energy U. Atoms in a spin singlet have lower the kinetic energy,
as they can virtually populate the doubly occupied states to change position.
This exchange process lowers the energy by $4J^2/U$.

calculation we again use the minimal example of two fermions with $s_i = \{|\uparrow\rangle, |\downarrow\rangle\}$
located at two different positions $i = 1, 2$. The manifold of single occupation
$\mathcal{S} = \{|\uparrow, \uparrow\rangle, |\uparrow, \downarrow\rangle, |\downarrow, \uparrow\rangle, |\downarrow, \downarrow\rangle\}$ is degenerate in energy and states where two
particles with different spin occupy the same position $\mathcal{D} = \{|\downarrow\uparrow, \cdot\rangle, |\cdot, \downarrow\uparrow\rangle\}$ have
additional on-site energy U.

We calculate [Aue98] the energy shift of the spatially symmetric state $|\Psi_S\rangle = \frac{1}{\sqrt{2}}(|\uparrow, \downarrow\rangle + |\downarrow, \uparrow\rangle)$ in second order perturbation theory by

$$\Delta E_S = - \sum_{d \in \mathcal{D}} \frac{\langle \Psi_S | H_J | d \rangle \langle d | H_J | \Psi_S \rangle}{\langle d | H_U | d \rangle} \tag{2.28}$$

where the sum goes over all possible states d of the submanifold $\mathcal{D}$. Figure 2.4
shows one possible exchange path for the example of two fermions in a double-well
potential with lowers the energy by J^2/U. From equation 2.28, we obtain eight
such paths. Four of them actually exchange the two particles so that one obtains
a energy reduction of $\Delta E_S = -4J^2/U$. Due to the Pauli principle, fermions in
the triplet configuration cannot occupy the same mode and consequently their
energy is not lowered. Consequently, the exchange integral lowers the energy
of the antiferromagnetic configuration by $J^{ex} = -4J^2/U$ with respect to the
ferromagnetic configuration.

This exchange mechanism was originally suggested by Kramers [Kra34] in order
to explain the anti-ferromagnetic alignment of magnetic moments of electrons on
the Mn^{2+}-ions in MnO. In the antiferromagnetic ground state, the electrons of the
oxygen orbitals can virtually occupy the singly occupied state of the Mn^{2+}-ions and

decrease the kinetic energy. For this reason, the mechanism is called *superexchange.* Later, it was further developed by Anderson [And50] and is nowadays of great relevance in copper-oxide antiferromagnets.

2.3.3 Simulating the Hubbard model with ultracold gases

Although the Hubbard model substantially simplifies the description of a strongly-correlated system by reducing it to only two competing processes, it has not been solved completely. Especially, whether away from half filling, it can describe d-wave superconductivity is still an open question. Instead of solving this complex system with classical computers, one can use analog quantum simulation with an experimental system.

Ultracold quantum gases represent a promising candidate to study strongly correlated quantum many-body systems. Along this idea, Jaksch and coworkers [Jak98] proposed the simulation of the Bose-Hubbard model using cold neutral bosons. With a combination of retroreflected far-detuned laser beams of wavelength λ one can create conservative potential given by $V_{\text{latt}}(x) = V_0 \sin^2(2\pi x/\lambda)$ in which atoms are trapped. These periodic potentials mimic the periodic crystal of ions that valence electrons in a transition metal experience [Blo05]. In addition, interactions between the neutral atoms can be introduced and controlled using s-wave scattering (see Section 2.4.1).

In that way, many experimental parameters can be controlled to a high precision. The potential landscape seen by the neutral atoms can be tuned with laser optics and the interparticle interaction can be changed over a wide range. Therefore, these systems offer a sophisticated playground [Jak05] for quantum simulation.

Since then, the predicted Mott-insulator has been observed first with bosons [Gre02] and later also with fermionic atoms [Jör08, Sch08]. High-resolution imaging allowed a little later to observe the quantum phase on a single-particle level [Bak09, She10, Gre16]. The experiments using quantum gases even allowed to observe the super exchange in double-well potentials [Föl07, Tro08]. However, achieving low enough temperatures to realizing the anti-ferromagnetic phase remained challenging [McK11]. After observing short-range correlations in several experiments [Gre11, Har15, Bol16] the recent observation of long-range antiferromagnetic correlations over more than 10 sites [Maz16] represents a major breakthrough.

2.4 Interactions in ultracold gases

Correlations in model systems are often created by strong interactions between the particles. The non-linear term in the Hamiltonian leads to a coupling between

the two particles and makes the system difficult to solve. In contrast to solid-state systems, where electrons interact via Coulomb repulsion, experiments with ultracold gases use neutral atoms. Nevertheless, there are possibilities to make the atoms strongly interacting. Additionally, these interactions can be tuned and controlled to a very high level, with makes the systems well suited for quantum simulations.

In ultracold quantum gases, interactions are tunable by magnetic Feshbach resonances. This technique is well extablished and details can be found in [Dal99, Ket08, Chi10]. In the following, we introduce the scattering mechanism between neutral particles that leads to interparticle interaction and explain how the interaction strength can be changed in the system. After that, we describe the influence of a confining potential on the interaction energy.

2.4.1 Scattering of two particles

In general, scattering in a particle sample is a very complex process as it is influenced by many parameters like the number of involved particles, the energy of the collisions, etc. In ultracold gases, the description of a scattering process simplifies substantially.

Ultracold samples are usually very dilute. With densities of 1 to 1000 particles per μm^3 the scattering can be considered as a two-body process [Chi10]. The interaction potential of two colliding particles is described by a central potential $V_{\text{int}}(\mathbf{r})$. At large distances it follows a van der Waals potential $\propto -C_6/r^6$ whereas at distances of a few Bohr radii, the potential is strongly repulsive [Ket08]. The typical size of the potential is about $r_0 \approx 50a_0 = 2.5\text{nm}$, where a_0 denotes the Bohr radius. Consequently, the probability to find more than two particles within the typical volume is negligible.

The scattering process of two particles can be described in the center-of-mass frame where $\mathbf{r} = \mathbf{r_1} - \mathbf{r_2}$ denotes the relative coordinate where the Schrödinger equation is given by

$$\left(\frac{p^2}{2m_r} + V_{\text{int}}(\mathbf{r})\right)\Psi_k(\mathbf{r}) = E_k\Psi_k(\mathbf{r}). \tag{2.29}$$

Here, m_r denotes the reduced mass, V_{int} describes the interaction potential and E_k is the collision energy. As for temperatures lower than $T < 1\text{mK}$ the de Broglie wavelength is much larger than the microscopic scattering potential. At large distances, one can therefore asymptotically describe the wave funcion by an incoming plane wave with momentum $\mathbf{k}$ and an outgoing scattered wave function

$$\Psi_k(\mathbf{r}) \propto \text{e}^{i\mathbf{k}\mathbf{r}} + f(\mathbf{k}', \mathbf{k})\frac{\text{e}^{ikr}}{r}. \tag{2.30}$$

The prefactor $f(\mathbf{k}', \mathbf{k})$ describes the scattering amplitude and as we consider elastic collisions, the energy in the scattering process is conserved ($k = k'$).

As our problem is spherically symmetric, we can use an expansion into partial waves $\Psi_l(\mathbf{r}) = R_l(r)Y_{lm}(\theta, \phi)$ where Y_{lm} are the spherical harmonics and $R_l(r)$ denotes the radial wave function with different angular momenta l. This has two interesting consequences. First of all, the exchange symmetry of the wave function depends on the angular momentum state l. For even angular momenta, the symmetry is positive and particles with a symmetric spatial wave function, like identical bosons or fermions in a spin singlet, can scatter with $l = 0, 2, \ldots$ (e.g. s-wave, d-wave etc.). In contrast to that, particles with an antisymmetric spatial wave function, like identical fermions, can only scatter with $l = 1, 3, \ldots$ (e.g. p-wave, etc.).

Secondly, as the angular momentum is conserved, only the radial part of the equation has to be solved. Its solution has an additional term proportional to $\hbar^2 l(l + 1)/r^2$. For $l > 0$, the interatomic potential therefore features an additional centrifugal barrier. This barrier is higher than the typical temperatures in ultracold gases and consequently, only s-wave scattering can occur[7] between particles with symmetric spatial wave function. Identical fermions cannot scatter at all. Additionally, the scattering amplitude has no angular momentum dependency and reduces to

$$f(\mathbf{k}', \mathbf{k}) \approx f_s = \frac{1}{k \cot \delta_s(k) + ik} \tag{2.31}$$

where f_s denotes the scattering amplitude and δ_s is a phase shift, which is the only change that the asymptotic wave function can experience for low momenta k at angular momentum $l = 0$. Therefore, this phase shift describes the entire collision process. By expanding $k \cot \delta_s(k)$ in a power series of k^2 which can be truncated for $k \ll 1/r_0$, we see that the collision process can be described by the so-called scattering length

$$a_{\text{sc}} = -\lim_{k \ll 1/r_0} \frac{\tan \delta_s}{k} \, . \tag{2.32}$$

If the scattering process did not cause a phase shift, the scattering length is zero. However, it becomes infinitely large for $\delta_s \to \pm\pi/2$. Its exact value is determined by the microscopic details of the scattering potential and very difficult to predict ab initio but whenever, the potential reaches a depth where it just supports another bound state, the phase shift of the outgoing wave function approaches $\pi/2$ and the scattering length diverges.

During the scattering process the internal structure of the potential is not probed as the de Broglie wave length is much larger than the potential range.

---

[7]p-wave collisions can only happen when they are resonantely enhanced.

Therefore, an exact knowledge of the potential is not necessary to describe the interaction between two particles. Instead, the actual potential can be replaced by the pseudo-potential

$$V_{\text{int}}(\mathbf{r}) = g_{\text{3D}}\delta(\mathbf{r})_{\text{reg}} = \frac{2\pi\hbar^2 a_{3D}}{m_r}\delta(\mathbf{r})_{\text{reg}}. \tag{2.33}$$

The delta potential has to be regularized in three dimensional systems to avoid a divergence[8] [Ket08]. With the help of the pseudo-potential the scattering of two particles can be described.

From the formula one can see, that the contact interaction can be represented by a repulsive potential or an attractive potential, only depending on the scattering length. For a positive scattering length, the potential becomes repulsive, whereas for a negative scattering length, the interaction between two particles is attractive.

2.4.2 Tuning the interaction using Feshbach resonances

The strength and sign of the scattering between two particles is determined by the microscopic details of the potential. To change the scattering length, one has to tune the depth of the potential to shift or create a bound state close to the continuum. For ultracold gases, this is not possible. Despite this, the scattering length can be changed in systems with ultracold atoms by using a magnetic Feshbach resonance. This phenomenon is described in detail in [Chi10]. So, we only give a short explanation of the mechanism.

In the scattering process that we just discussed, a large phase shift of the out-going wave function causes strong interaction. Such a phase shift can not only be accumulated by a bound state close to the continuum but also by one in a energetically higher molecular potential. This situation is shown in Figure 2.5. Two particles with a small energy E enter the open channel. A molecular potential of a different spin configuration is not accessible energetically and thereby denoted as a closed channel. If a bound state in the closed channel E_c is resonant to the energy of the colliding particles and if the two states couple weakly, the state can virtually occupy the bound state in the closed channel for a finite time and the out going wave function accumulates a phase shift.

In ultracold atoms, the different channels are molecular potentials of different spin configurations with different magnetic moments μ_o and μ_c. By applying a magnetic offset field, the energy difference between the two potentials can be tuned $\Delta E = (\mu_o - \mu_e)B$ and the resonance can be engineered.

---

[8]$\delta(\mathbf{r})_{\text{reg}} \cdots = \delta(\mathbf{r})\frac{\partial}{\partial r}r \ldots$
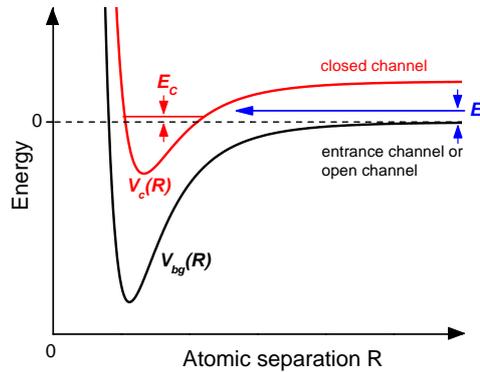
Figure 2.5: Schematic of a Feshbach resonance. The open channel describes the accessible scattering potential of two particles. If the collision energy E is in resonance with a bound state in a higher lying closed-channel potential, a phase shift can be accumulated by a virtual occupation of the resonant state. This leads to a change of the scattering length. In ultracold gases, the energy difference between the two particles can be tuned via a magnetic offset field. Taken from [Chi10]

The diverging scattering length as a function of the magnetic offset field B can be described by the empirical formula [Chi10]

$$a_{\mathrm{sc}}(B) = a_{\mathrm{bg}} \left(1 - \frac{\Delta B}{B - B_0} \right) \tag{2.34}$$

where a_{bg} describes the background scattering length, B_0 is the magnetic field, where the resonance occurs and ΔB describes the width of the resonance.

Feshbach resonances in ^{6}Li

In our experiment, we work ^{6}Li atoms in the three lowest hyperfine states $|1\rangle$, $|2\rangle$ and $|3\rangle$. Between all three states, ^{6}Li exhibits Feshbach resonances with widths on the order of $100\,\mathrm{G}$. Figure 2.6 shows the scattering lengths as a function of the magnetic offset field for all three combinations. The resonances are around $830\,\mathrm{G}$ and $690\,\mathrm{G}$ and at fields around $550\,\mathrm{G}$, all three combinations have zero crossings which allow us to create non-interacting two-component Fermi gases. The resonance positions where corrected and determined with higher precision in [Zü13]. In our experiment, we use the Feshbach resonances to tune the interaction strength in a two-component Fermi-gas.
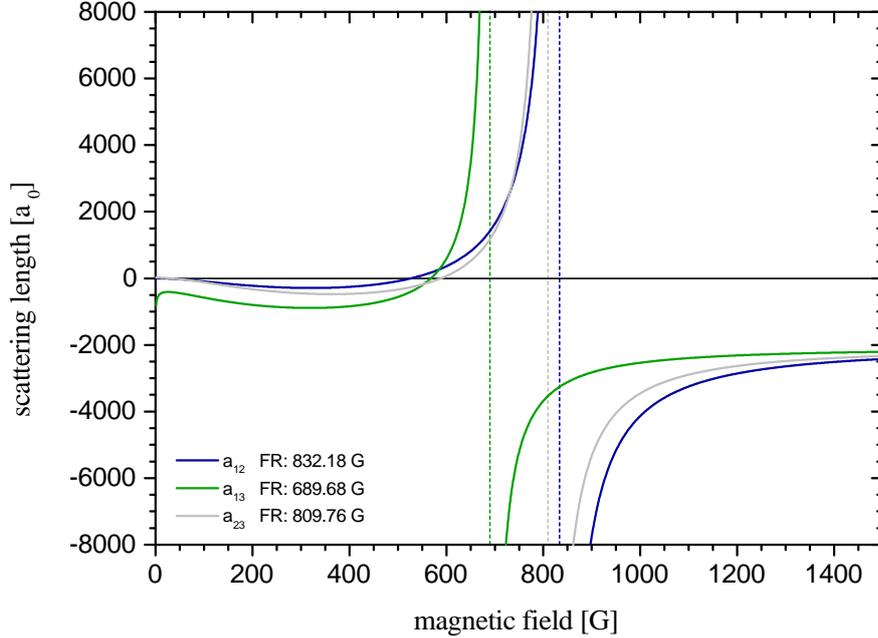
Figure 2.6: Feshbach resonances of ^{6}Li. All combinations of the three lowest hyperfine states exhibit a broad Feshbach resonance around 700 - 850 G. The interactions strength can be tuned to zero below the Feshbach resonances. Taken from [Ber13].

2.4.3 Interaction in a trapping potential

In presence of a trapping potential, the scattering process between two particles can significantly change. The description of asymptotic ingoing and outgoing waves becomes meaningless and the confinement results in a discrete energy spectrum. In several papers, the influence of an underlying potential of different kinds has been studied [Bus98, Ols98, Ber03, Idz06]. The results are of high importance for the calculation of the interaction strength in one or several microtraps. In the following, we give a short introduction along these publications. We will first present a full three-dimensional solution of the scattering problem in a cigar-shaped potential and then reduce the description to one dimension.

Two interacting particles in a cigar shaped harmonic potential

In our experiment, we trap particles in optical tweezers formed by Gaussian beams. These trapping potentials can be approximated by three-dimensional harmonic oscillators. Due to their creation from focusing a Gaussian beam, the tweezers are

axially elongated. We can describe the trapping potential by

$$V_t(\mathbf{r}) = \frac{1}{2} m \left(\omega_\perp^2 \rho^2 + \omega_z^2 z^2 \right) \tag{2.35}$$

where $\omega_\perp$ and ω_z denote the radial and axial trapping frequencies. From this, one can define the aspect ratio $\eta = \omega_\perp / \omega_z$ to characterize the shape of the potential.

For weak interactions, the wave function of the atoms in a microtrap can be approximated by Wannier functions but as soon as we approach the Feshbach resonance, this description is not valid anymore. Under certain approximations, the interaction energy between two particles in such a trapping potential can be calculated analytically at any scattering length [Idz06]. Here we only show the most important steps in this calcuation. For details, we refer to [Idz06] and to [Zü12a, Mur15a].

The two-particle Hamiltonian of the system is given by

$$H = -\frac{\hbar^2}{2m} \nabla_\mathbf{1}^2 - \frac{\hbar^2}{2m} \nabla_\mathbf{2}^2 + V_t(\mathbf{r_1}) + V_t(\mathbf{r_2}) + V_{\text{int}}(\mathbf{r_1} - \mathbf{r_2}) \tag{2.36}$$

where $\mathbf{r_1}$ and $\mathbf{r_2}$ denote the position of the two particles, m is the mass of a particle and the interaction potential $V_{\text{int}}(\mathbf{r})$ is described according to equation 2.33. For a harmonic potential $V_t(\mathbf{r})$, we can decouple the center-of-mass motion and the relative motion. We introduce the center-of-mass coordinate $\mathbf{R} = (\mathbf{r_1} + \mathbf{r_2})/2$ and the relative motion coordinate $\mathbf{r} = \mathbf{r_1} - \mathbf{r_2}$ of the two particles and obtain

$$H_{\text{COM}} = -\frac{\hbar^2}{2M} \nabla_\mathbf{R}^2 + \frac{M}{m} V_t(\mathbf{R}) \tag{2.37}$$

$$H_{\text{REL}} = -\frac{\hbar^2}{2m_r} \nabla_\mathbf{r}^2 + \frac{m_r}{m} V_t(\mathbf{r}) + V_{\text{int}}(\mathbf{r}) \quad . \tag{2.38}$$

As a consequence of the separation, the interaction potential is only present in the equation for the relative motion with m_r describing the relative mass. The center-of-mass Hamiltonian H_{COM} describes a simple harmonic oscillator with twice the mass $M = 2m$ and its eigenfunctions are the usual harmonic oscillator wave functions. In order to describe the eigenfunctions of the relative motion, we chose the basis of two-dimensional harmonic oscillator wave functions in polar coordinates $\Phi_{n,m}$ with n is the radial and m the angular quantum number and the one-dimensional harmonic oscillator wave function $\Theta_k(z)$ with the quantum number k. The eigenfunctions can then be written as a superposition of the basis states

$$\Psi(\mathbf{r}) = \sum_{n,k} c_{n,k} \Phi_{n,0}(\rho, \phi) \Theta_k(z) \tag{2.39}$$

where only the summation over the angular quantum states $m = 0$ is necessary. Solving for the coefficients $c_{n,k}$ and inserting it into the Schrödinger equation results in an implicit formula for the eigenenergy

$$-\frac{\sqrt{\pi}}{a_{\mathrm{sc}}} = \mathcal{F}(-\mathcal{E}/2). \tag{2.40}$$

Here, a_{sc} is expressed in units of the harmonic oscillator length $a_z = \sqrt{\hbar/(m_r \omega_z)}$ and $\mathcal{E} = E - E_0$ describes the energy of the system in units of the harmonic oscillator energy $\hbar \omega_z$ on top of the ground state energy $E_0 = 1/2 + \eta$.

If the harmonic trapping potential is cigar shaped, i. e. the aspect ratio $\eta > 1$, $\mathcal{F}(x)$ can be calculated for $\mathcal{E} < 0$ and analytically continued to $\mathcal{E} > 0$. The energy shift in a cylindrically symmetric trap is described by the exact formula

$$\mathcal{F}(x) = -2\sqrt{\pi}\frac{\Gamma(x)}{\Gamma(x-1/2)} + \sqrt{\pi}\frac{\Gamma(x)}{\Gamma(x+1/2)}\sum_{m=1}^{n-1} F(1, x; x+1/2; \mathrm{e}^{i\frac{2\pi m}{n}}) \tag{2.41}$$

where $F(a, b; c; x)$ is the hypergeometric function $_2F_1$, $\Gamma(x)$ denotes the Euler gamma function. Equation 2.41 can be simplified[9] for aspect ratios much larger than one $\eta \gg 1$. This makes it interesting to compare the result with the true one-dimensional model solved in [Bus98].

One-dimensional solution and confinement-induced resonance

For the one-dimensional system, the interaction pseudo-potential can be written as $V_{\mathrm{int,1D}}(r) = g_{\mathrm{1D}}\delta(r)$. The Schrödinger equation can then be solved by again separating the center of mass motion from the relative motion. After another lengthy calculation one obtains an implicit formula for the eigenenergy

$$-\frac{1}{g_{\mathrm{1D}}} = \frac{m_r}{2\hbar^2}\frac{\Gamma(-\mathcal{E}/2)}{\Gamma(-\mathcal{E}/2 + 1/2)}. \tag{2.42}$$

By comparing this with the solution for the three-dimensional cigar shaped potential with large aspect ratio, we find the relation between the one-dimensional coupling strength and the scattering length, that was deduced in [Ols98]

$$g_{\mathrm{1D}} = \frac{2\hbar^2 a_{\mathrm{sc}}}{m_r a_\perp^2}\frac{1}{1 - Ca_{\mathrm{sc}}/(a_\perp)} \tag{2.43}$$

---

[9] Equation 2.41 can be simplified to $\mathcal{F}(x) \approx \sqrt{\pi}\eta\zeta_H\left(\frac{1}{2}, 1 + \frac{x}{\eta}\right) + \eta\sqrt{\pi}\frac{\Gamma(x)}{\Gamma(x+1/2)}$, where $\zeta_H(s, a) = \sum_{k=0}^{\infty}(k + a)^{-s}$ denotes the Hurwitz zeta function [Idz06].
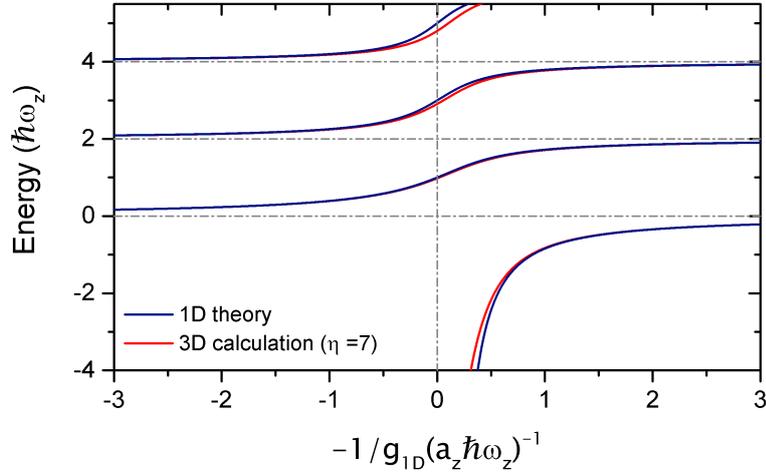
Figure 2.7: Energy spectrum for a three-dimensional cigar-shaped trap and the one-dimensional solution. Plotted is the additional energy, that two particles can gain by interacting in a one-dimensional system (blue) or in a three-dimensional cigar-shaped potential with an aspect ratio of $\eta = 7$ (red).

where $C \approx 1.46035$ and $a_\perp = \sqrt{\hbar/(m_r \omega_\perp)}$. One observes that the one-dimensional coupling strength g_{1D} diverges when the scattering length has the same scale than the harmonic oscillator length in the direction of the confinement $C\, a_{sc} = a_\perp$.

Figure 2.7 shows a comparison of the eigenenergies for two particles in a cigar-shaped trap and the true one-dimensional solution. Differences in the eigenenergies are only noticable in the strong-coupling regime of $-1 < -1/g_{1D} < 1$. In the attractive branch the deviations increase with the coupling strength as the one-dimensional model only exhibits a molecular state on the attractive side, in contrast to the three-dimensional system. In the lowest repulsive branch, the two solutions deviate only by 2% from each other. Only for higher excitations the eigenenergy gets significantly influenced by the dimensionality and the deviations increase. This means that especially in the repulsive branch and for large aspect ratios our system can be described in a one-dimensional framework.

Fermionization of two distinguishable Fermions

In the repulsive branch of the one-dimensional model, the energy of two particles increases with increasing interaction strength (see Figure 2.8 b). At the point where the one-dimensional coupling strength g_{1D} diverges, the energy of the relative motion is exactly $\hbar\omega_z$. This means that the energy of the two interacting particles
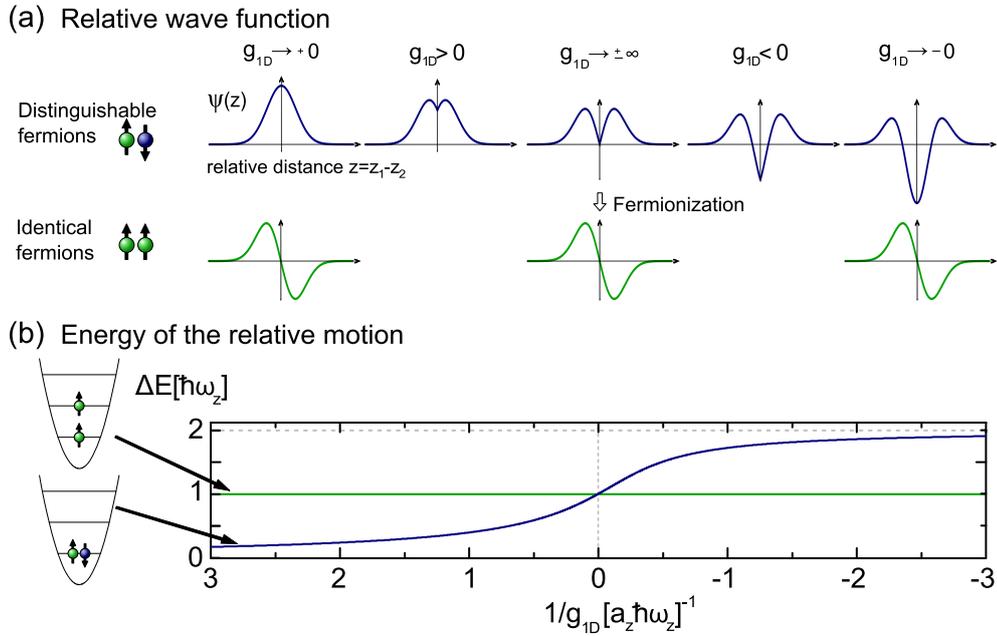
Figure 2.8: Fermionization of two distinguishable fermions. a) The relative wave function of two interacting particles is plotted over the interaction strength of a contact interaction. In the non-interacting case, it is described by a simple Gaussian wave function, but as soon as the repulsion is increased the particles tend to avoid being at the same position, which is visible as a cusp in the wave function. The extreme case is reached when the one-dimensional coupling strength g_{1D} diverges. Then the relative wave function looks like the one of inpenetrable particles and the modulo square is identical to the modulo square of two identical fermions. This point is named *fermionization* and allows for a mapping of the system on identical fermions. **b)** Consequently also the energy of the two systems is the same. The state of the interacting fermions continues to exist at the attractive side where it becomes an excited state. At weak attraction, its energy eventually reaches $2\hbar\omega_z$. Taken from [Wen13b]

with a spin wave function of $\chi = \frac{1}{\sqrt{2}}(|\uparrow\downarrow\rangle - |\downarrow\uparrow\rangle)$ coincides with the energy of two identical fermions with a spin wave function $|\uparrow\uparrow\rangle$.

This phenomenon, which holds in one dimension for a delta-like interaction potential, is known as *fermionization*. Originally, it was formulated for interacting bosons [Gir60]. However, also two interacting fermions can be fermionized [Gir10] as was shown in[Zü12b]. The fermionization can be easily understood by comparing the relative wave functions of two identical fermions and two distinguishable interacting fermions (see Figure 2.8 a). The spatial relative wave function of two identical fermions is antisymmetric and the two particles are inpenetrable. For two interacting particles the same situation can be generated with repulsive short-range interaction. At $z = 0$, the repulsion generates a cusp in the relative wave function as the particles avoid each other. This cusp increases with the interaction strength until it eventually goes to zero $\Psi(z = 0) = 0$ and the two particles become completely impenetrable. At the fermionization point, the modulo square of the wave function is identical to the one of two identical fermions.

The repulsive branch continues at the attractive side as an excited state. Looking at the wave function, the cusp continues in the relative wave function becomes negative at the origin $\Psi(z = 0) < 0$. Following this branch the attractive interaction decreases until it reaches the $g_{1\mathrm{D}} = 0$ where the relative wave function is identical to the second excited harmonic oscillator wave function and the system has gained another $\hbar\omega_z$.

On the interaction resonance, the particles are inpenetrable. Around the interaction resonance, the system is in the strong coupling regime and the system is highly correlated [FA03]. In [Deu14] it was shown that this regime can be described by a spin chain model. In the special case of a two-component Fermi system, it can be described by the Heisenberg model with a spin coupling term $J \propto 1/g_{1\mathrm{D}}$. This holds for even more than two particles and was demonstrated experimentally by Murmann et al. [Mur15c].

Solutions for more than two fermions

For a homogeneous system, the thermodynamic limit of infinitely many identical fermions interacting with one impurity was already analytically solved by McGuire [McG65]. A few years later, the one-dimensional problem of a two-component Fermi gas was exactly solved [Yan67].

We just saw that there exists an analytic solution for two harmonically trapped interacting particles in a one-dimensional system [Bus98], but for larger particle numbers, only numerical methods are available. They can still predict the energy spectrum up to 8 particles with a high precision [Gha12, Bro13, Gha13, Sow13, Gha14, Gha15] but solving larger systems is very hard. Quasi-analytical

approaches, which are not limited in particle number, can describe the system only in the strong-coupling region [Gua09, Lev14, Vol14].

In our experimental setup, we prepare few-fermion systems in one or several elongated microtraps with high control on the prepared atom number. In addition, we can tune the interaction strength at will. This allows us to study quasi-one dimensional system and systems with few sites in the crossover from few to many particles. The necessary tools and the experimental preparation will be the subject of the next chapter.

Chapter 3

Preparing few-particle systems with high fidelity

After the first experimental demonstration [Ser11b], the deterministic preparation of few-particle systems became central for all our experiments. Preparing small quantum systems in a distinct quantum state with unprecedented fidelity enables us to study systems with low entropy at a high level of control.

We create samples containing few fermions by starting with an ultracold degenerate Fermi gas of several thousand particles. This serves as a reservoir for filling a small but deep potential well with a few atoms. The high quantum degeneracy leads to a large occupation probability in the lowest levels. We then deterministically spill all but the lowest-lying states and thereby obtain few-fermion system in the overall ground state of the system.

This chapter describes the experimental methods to realize and probe few-particle systems. First, the experimental sequence to prepare few-particle systems and our methods of manipulate and detect the quantum states will be explained. After that, a short overview on the experimental setup to reach a quantum degenerate Fermi gas is given, followed by a detailed description about the tools to create and control one or several microtraps.

3.1 Preparing, manipulating and probing few fermions

The preparation of few-fermion system is routinely done in our group. Due to the small particle number a lot of repetitions are necessary to gain enough statistics. Therefore, the experimental challenge is to provide a reliable experimental setup that has a short cycle time. As postselection of the data is often not possible, the preparation and detection of the quantum state have to be robust and the parameters have to be stable in order to guarantee the preparation of systems

with low entropy.

The experimental sequence is completely automatized. We use an experimental control (ADwin Pro II, Jäger Messtechnik) that provides a time resolution of several microseconds for the digital and analog channels. One cycle of the sequence takes 10 to 12 seconds and consists of four basic parts: The preparation of an atom reservoir, the preparation of the few-particle system, its manipulation and detection.

3.1.1 Preparation of an atom reservoir

The preparation of a reservoir containing a degenerate Fermi gas is achieved in several experimental steps and takes about 8 seconds of every experimental cycle. We start with an atomic beam of Lithium atoms exiting an oven. In a first step, we slow the atoms down using a Zeeman slower. After this, they are captured and laser cooled in a magneto-optical trap (MOT). After about 2 seconds of loading time we end up with about 1×10^8 atoms at a temperature of around 400μK and a phase space density of 10^{-6} [Ser11a]. To increase the phase space density further, we directly transfer the atoms into a crossed-beam optical dipole trap with a transfer efficiency of around 1%. By applying a long high-power radio frequency pulse between the two lowest hyperfine levels we create a balanced two-component sample. This allows us to perform evaporative cooling with a single-species Fermi gas. We first evaporate at a magnetic offset field close to the Feshbach resonance where the scattering length between the two hyperfine spin states is several thousand Bohr radii. In that way we maximize the thermalization rate. As soon as the temperature of the ensembles is on the order of the binding energy of dimers, we change the magnetic field to $300\,$G to allow the preparation of a weakly interacting Fermi gas. There, the scattering is not more than 1000 a_0 and negative. After 6s of evaporation time we end up with 6×10^4 atoms per spin state at a temperature of $250\,$nK. This corresponds to a degeneracy of about $T/T_\mathrm{F} \approx 0.5$ [Ser11a].

3.1.2 Preparation of a few-fermion system

For systems with identical fermions, the Pauli principle holds and each quantum state can be at most occupied by one fermion. If the atom sample has a low temperature, the atoms occupy the bound states of the potential according to the Fermi-Dirac distribution where the lowest states have the highest probabilities to be occupied. We exploit this to prepare few-fermion systems. A more detailed description of the preparation technique can be found in [Ser11a, Ser11b, Zü12a].
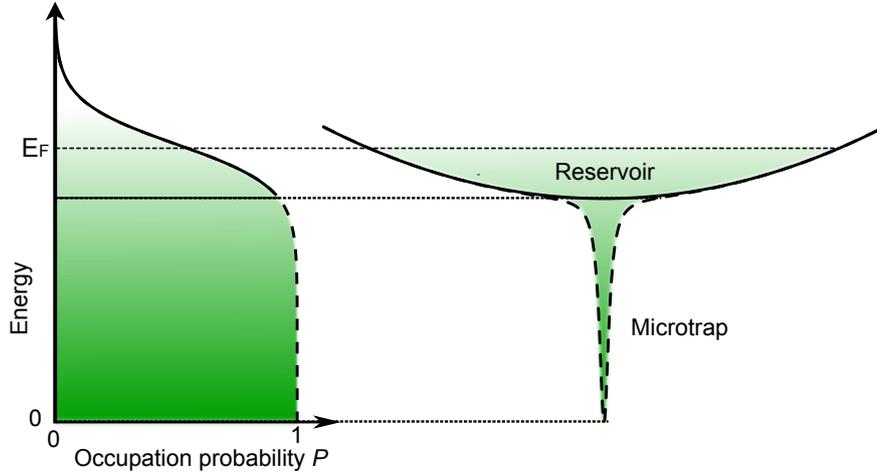
Figure 3.1: The dimple trick. We prepare a Fermi gas in a large optical
dipole trap with a temperature of 250 nK and a degeneracy of $T/T_F \approx 0.5$.
By overlapping a tightly focused microtrap with a depth much larger than the
depth of the reservoir trap, the Fermi energy is locally significantly increased.
As the microtrap only contains a small fraction of the total atom number,
the temperature of the combined system does not change. In that way, the
degeneracy of the Fermi gas can be increased to $T/T_F \approx 0.05$ which leads to
a occupation probability of the lowest state of $P(E_0) >$99.99%. Figure taken
from [Ser11a] and adapted.

The degenerate Fermi gas in the crossed beam dipole trap serves as a reservoir
for this step. In order to increase the degeneracy of the system, we make use of
the dimple trick [SK98] and superimpose a tightly focused optical dipole trap with
the reservoir trap (see Figure 3.1). Due to its waist size of roughly 1μm we call it
microtrap.

To avoid heating up the Fermi gas, we slowly ramp on the microtrap and let the
system thermalize. As the microtrap only contains a fraction of the atoms in the
reservoir, the overall temperature of the system is determined by the temperature
of the reservoir. However, the presence of the microtrap leads to a local increase of
the Fermi energy E_F. In this way, the occupation probability of the lowest state
E_0 can be increased to

$$P(E_0) = \frac{1}{\exp(\frac{E_0-\mu}{k_B T}) + 1} \approx \frac{1}{\exp(\frac{E_0/k_B - T_F}{T_{\text{ODT}}}) + 1} \tag{3.1}$$

where the energy of the lowest state is E_0 and the chemical potential $\mu \approx k_B T_F$.
The Fermi temperature in the combined system is $T_F = T_{F,\text{res}} + T_{F,\text{MT}} \approx 7\mu$K.
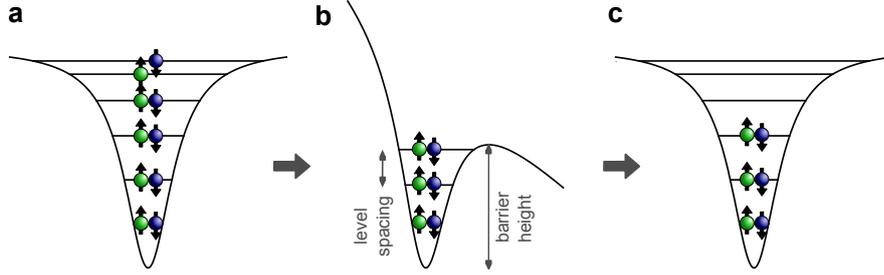
Figure 3.2: The spilling scheme. a Using the dimple trick, the microtrap
is filled with several hundred fermions in two hyperfine states at a degeneracy
of $T/T_F \approx 0.05$. **b** To prepare a few-particle systems in a deterministic way,
we apply a magnetic field gradient of about $30\,\text{G/cm}$ and thereby deform
the trapping potential that the atoms experience. Additionally, we tune
the barrier height to a precision higher than the level spacing to control
the number of bound states in the potential. **c** After a typical spill time of
$25\,\text{ms}$, we decrease the magnetic field gradient again. In this way, we achieve
a well-defined number of atoms in the ground state of the system with a
fidelity above 90%.

This results in an occupation probability of $P(E_0) >99.99\%$ of the lowest state in
the microtrap.

After the thermalization, we can switch off the reservoir trap and are left with a
few hundred particles in the microtrap. They occupy the tight trapping potential
according to the Pauli principle. As our initial sample contained fermions in two
different hyperfine states, each quantum state is filled with two particles. This is
schematically shown in Figure 3.2 a.

To initialize a few-fermion system, we deterministically remove atoms from the
higher lying states by deforming the trapping potential. As schematically shown
in Figure 3.2 b, we do this by applying a magnetic field gradient B' on the order
of 30G/cm along one direction of the trapping potential. Due to the interaction
with the magnetic moment μ this leads to a tilt of the overall potential

$$V(z) = V_0 \left(1 + \left(\frac{z}{z_R}\right)^2\right) + \mu B' \tag{3.2}$$

where V_0 denotes the depth of the potential, which is created by a focused Gaussian
laser beam with a Rayleigh length denoted by z_R. The tilt of the trap results in
a reduction of bound states in the trap. As a consequence, the atoms above the
barrier leave the trap.

We prepare few-fermion systems with distinct atom numbers by tuning the
barrier height and thus chosing the number of bound states in the potential. For

a precise control, the large level spacing in the microtrap in combination with a small heating rate during the spilling process is crucial.

We perform this spilling technique at a magnetic offset field where the fermions in the two different hyperfine states are non-interacting and thus behave independently from each other. In addition their magnetic moments are similar and consequently they experience the same tilt[1]. In this way, we prepare even atom numbers of up to 10 particles with fidelities above 90% with full control over the motional state.

3.1.3 Manipulation of the few-fermion system

After the initialization of few fermions in the overall ground state of a microtrap, we manipulate the few-fermion system. We can control the scattering length between all the three lowest hyperfine states $|1\rangle$, $|2\rangle$ and $|3\rangle$ by means of a broad Feshbach resonance, described in Section 2.4. For this, we change the magnetic offset field in the system using the Feshbach coils and thereby tune the interaction strength in the system. In this way, we could study few strongly repulsive distinguishable fermions [Zü12b, Mur15c] and weakly attractive fermions [Zür13].

In addition, we can change the hyperfine state of an atom by applying a radio-frequency field. The transition between two hyperfine states is well-described by a two-level system. This allows us to drive coherent Rabi oscillations and perform precise measurements of the interaction energy. For ^{6}Liatoms the necessary transition frequencies are around 80 MHz for magnetic fields higher than 100 G. In the past, we used RF-spectroscopy to study systems with increasing particle number at various interaction regimes [Wen13b]. Furthermore, it was used to perform a high-precision measurement of the scattering length around the Feshbach resonance. In Chapter 5 we use coherent Rabi oscillations to measure the total spin state of a few-fermion system and study a one-dimensional system of one impurity immersed in a Fermi sea of few majority particles.

After an upgrade in 2013, our setup also allows us to change the trapping potential by adding one or even more optical tweezers to the system [Kli12, Ber13]. To do this, we use an acousto-optic deflector that allows to create more potential wells and change their distance and relative depths at will. The technical requirements to do this will be explained in detail in Section 3.3.2. In [Mur15b] we demonstrated the experimental control over the individual wells by preparing the atoms in the ground state of a coupled double well and thereby realized the fundamental building block of the Fermi-Hubbard model. A description of the experiments is given in Section 6.

---

[1]By performing the spilling at a magnetic offset field of around 27 G, we can prepare spin-polarized samples of atoms in state $|2\rangle$. At these offset fields their magnetic moment is zero and consequently they are not spilled from the trap.
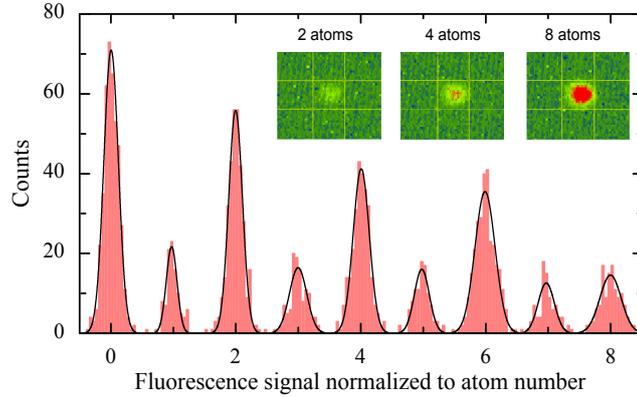
Figure 3.3: Fluorescence signal from single atoms. To image the atoms in the microtrap, we recapture them in the MOT and detect the fluorescence of single atoms with a CCD camera. To achieve the single-atom sensitivity, we decrease the size of the MOT by applying a MOT gradient of $250\,\mathrm{m/s}$ and detuning of the MOT beams of only -2Γ. We integrate the fluorescence signal in a region-of-interest for 0.5 seconds (inset). The histogram of the fluorescence signal shows peaks that correspond to integer atom numbers. For 2 atoms (6 atoms) we detect a signal width of $\sigma = 0.11$ ($\sigma = 0.16$), which results in a separation of 9σ (6σ) from the neighboring peak and corresponds to a detection fidelity larger than 99%. Figure taken and adapted from [Mur15a].

3.1.4 Readout with single-atom sensitivity

For the experiments presented in this thesis, two different imaging techniques were used. Our traditional way of measuring few atoms is to recapture them in the MOT where we detect their fluorescence [Hu94, Ser11a, Hum13]. For this we apply a magnetic field gradient of 250G/cm and a detuning of the MOT beams of -2Γ. We collect about 0.8% of the emitted fluorescence during 0.5 seconds and image it on a CCD camera [Ser11a]. From the recorded signal, we can then deduce the exact atom number with a fidelity better than 98% for more than 10 atoms (see Figure 3.3).

However we lose information about the occupation number per site, the spin state and the energy level the atoms were in. In order to gather this information we have to perform selective spillings before the detection in the MOT. For experiments with several optical tweezers this means that we have to uncouple the wells and switch off all but one well to measure quantities like the occupation number site selectively. This is very time consuming especially for system with more than two wells.

①	Titanium sublimator	④	Zeeman Slower
②	Ion pump	⑤	Octagon
③	Lithium oven	⑥	Gate valve
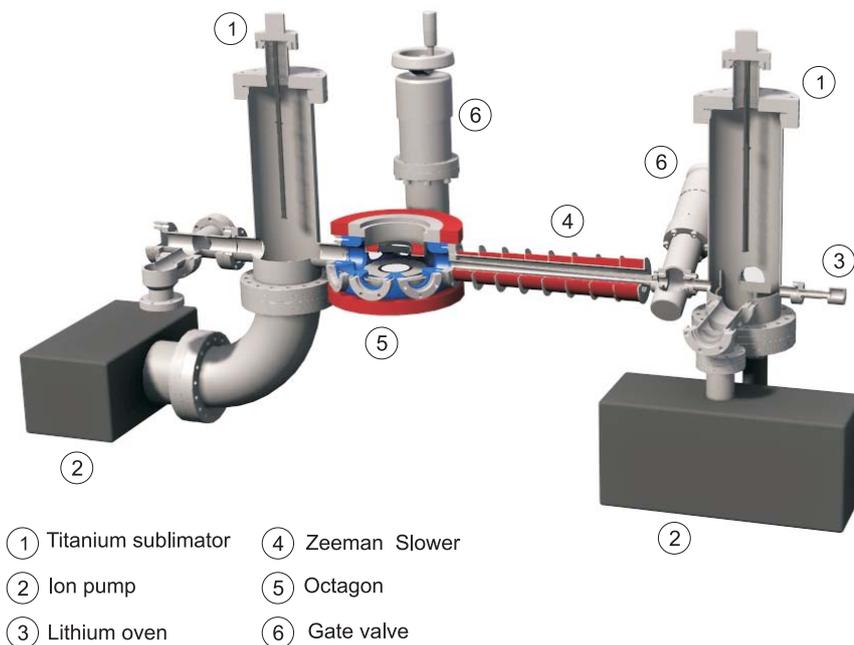
Figure 3.4: Vacuum chamber. The vacuum chamber of the table-top experiment has a length of about 1.5 m. Two ion pumps and two titanium sublimators create ultrahigh vacuum conditions. The atoms are heated up in the oven section and travel towards the octagon. To slow down the atoms, we use a Zeeman slower. We trap the atoms in the octagon, where the cooling, preparation, manipulation and detection takes place. Figure taken from [Ser07].

In order to overcome this limitation, we developed a novel imaging technique that allows single-atom detection with spatial and spin resolution. It is based on fluorescence imaging and not restricted to the localization of the atoms in one potential well. Chapter 4 reports on this new technique that allows us to resolve the momenta of individual atoms. This paves the way to measuring momentum correlations of complex many-body states.

3.2 Experimental steps towards a degenerate Fermi gas of ^{6}Li-atoms

The starting point for the preparation of few fermions is a degenerate Fermi gas. Its production is routinely done in our group and described already in several

theses [Lom11, Ser11a] as well as in the general literature [Ket08]. The details on the production of the degenerate Fermi gas do not influence the steps thereafter and so this section will only provide an overview on the experimental setup.

3.2.1 Vacuum chamber and oven

Experiments with ultracold quantum gases are inherently decoupled from the surrounding environment. Reaching temperatures in the range of hundred nanokelvin requires ultrahigh vacuum conditions. A sketch of our vacuum chamber is shown in Fig.3.4. Two ion getter pumps ② in combination with two titanium sublimators ① are necessary to reach pressures on the order of 10^{-12} mbar which are crucial for the preparation of few-fermion systems.

In the oven section ③ a few grams of solid Lithium are heated up to $350\,°C$ to form a hot gas of lithium atoms. They travel along a 30-cm long drift tube, that serves as a differential pumping stage towards the science chamber. To provide optical access the science chamber consists of an octagon ⑤ with 6 small viewports at the sides. Two reentrant viewports at the top and bottom allow for optical access of NA=0.65.

3.2.2 MOT and Zeeman slower

The atoms leaving the oven have an average speed of 1000m/s. To decelerate them in the drift tube, a resonant laser beam is counterpropagating the atom beam. The light force of several thousand absorption and re-emission events, each changing the momentum of the atoms by $\hbar\mathbf{k}$, can slow them down to a few m/s. During this slow-down the Doppler effect leads to a change of the resonance frequency of the atoms $\Delta\omega = kv$ as a function of their velocity v. To compensate for the frequency change, we use a so-called Zeeman slower [Met99]. It provides a spatially varying magnetic field designed such that the resulting Zeeman effect compensates the changing resonance frequency along the deceleration. After passing the Zeeman slower the atoms enter the science chamber with a velocity lower than $50\,m/s$ where they can be captured by the Magneto-optical trap [Met99]. It consists of three pairs of counterpropagating red-detuned laser beams that cause a frictional force on the atoms in combination with an additional spatially dependent magnetic field provided by the MOT coils that makes the light force spatially dependent and confines the atoms in the magnetic field zero.

We load the MOT for 2 seconds and end up with 1×10^8 atoms. The ensemble has a temperature of $400\,\mu K$ which is limited by the Doppler temperature and reaches a phase space density of 10^{-6} [Ser07].

3.2.3 Optical-dipole trap

Quantum degeneracy sets in at a phase space density on the order of 1. In order to reach this regime, we have to confine the atoms in a trapping potential that does not involve resonant photon scattering. There are two different approaches to provide a conservative potential for neutral atoms: One method uses the fact that a magnetic field gradient can create a force acting on the atoms due to its coupling to the magnetic moment of the particles[2]. By creating a magnetic field with a minimum, one can thus trap low-field seeking atoms around this minimum. The second way, the method we are using, is the creation of a trapping potential by a far-detuned laser beam.

In an optical dipole trap [Gri00], a force acting on neutral atoms is created by the oscillating electric part of the laser field $\mathbf{E}(\mathbf{r}, \mathbf{t})$. This field induces an electric dipole moment $\mathbf{p}$ on the atom, which interacts with the electric field and creates a potential of the form $V_{\text{dipole}} = -\frac{1}{2}(\mathbf{Ep})$. Similar to a driven harmonic oscillator, the induced dipole moment $\mathbf{p}$ will oscillate in phase with the electric field if the driving frequency ω is lower that the resonance frequency of the atom ω_0. This results in an attractive dipole potential. For driving frequencies higher than the resonance frequency, the potential becomes repulsive. The potential created by the far-red detuned laser beam is described by

$$V_{\text{dipole}}(\mathbf{r}) = -\frac{3\pi c^2}{2\omega_0^3} \left(\frac{\Gamma}{\omega_0 - \omega} + \frac{\Gamma}{\omega_0 + \omega} \right) I(\mathbf{r}) \qquad (3.3)$$

where c is the speed of light and Γ denotes the transition linewidth. The intensity distribution of the laser field $I(\mathbf{r})$ thus fully determines the shape of the trapping potential. The potential depth scales with $(\omega_0 - \omega)^{-1}$, but small detunings from the resonance frequency lead to a significant rate of photon scattering. At the expense of lower potential depths one therefore choses large detunings where the photon scattering rate Γ_{sc} scales with $(\omega_0 - \omega)^{-2}$.

Our optical dipole trap is detuned 400nm from the ^{6}Li resonance. In order to provide sufficient depth and spatial overlap to directly transfer the atoms from the MOT, we use a Ytterbium-doped fiber laser (YLR-200-LP, IPG Photonics) with about 200 Watt power[3]. The trap is formed by two laser beams (see Figure 3.5) with a waist of $w_0 = 50\mu$m which intersect in an angle of 14°. This results in an aspect ratio of about 1:8 and a gaussian profile along the intersection of $\sigma_{\text{z}} = 200\mu m$.

---

[2]Note that we use this for spilling our microtrap, see section 3.1.2.

[3]In the course of this thesis, we had to replace the laser and found out that 100 Watt is sufficient for the efficient transfer and evaporation of the atoms. Note also that the dimensions for the beams slighly changed after this exchange due to a different fiber laser collimator.
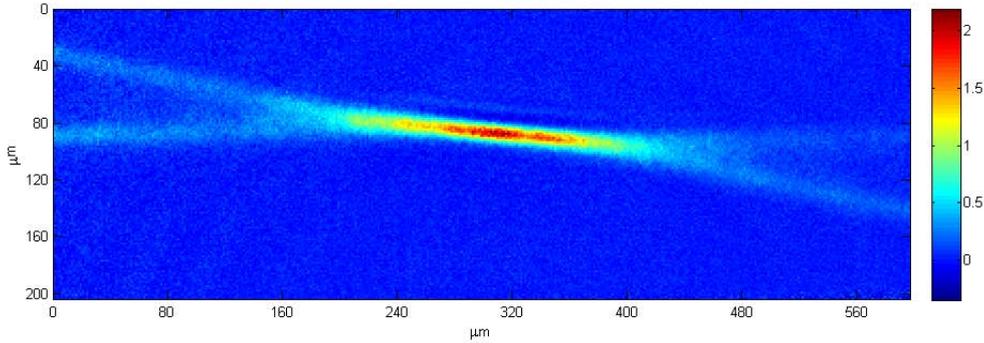
Figure 3.5: Optical dipole trap filled with atoms. The optical dipole trap is created by two far-red detuned laser beams crossing at an angle of 14°. The absorption image of a hot atomic sample from the top shall visualize the shape of the optical dipole trap. Figure taken from [Lom11].

For evaporative cooling, we decrease the laser power by the analog control of the laser itself and two AOMs that are placed in the beam path. The laser power is monitored by focusing light, that is transmitted through a mirror, on two photodiodes with different gain. This allows us to feed-back on the power and vary it over a large range. A detailed description of the entire optical dipole trap setup can be found in [Lom11].

3.2.4 Feshbach coils

A pair of coils in almost Helmholtz configuration provides the homogeneous magnetic offset field to tune the scattering length of the atoms. The coils are mounted around the reentrant viewports of the science chamber (see Figure 3.4) and can provide fields up to 1400 G. They allows us tune the interaction strength from repulsive, across the broad Feshbach resonances (see Sec.2.4) around 800 G to the attractive side.

Both coils consist each of 15 windings of flat copper wire with a cross-section of $1 \times 5 mm^2$, that are wound up in a spiral and then lathe faced on one side. The bare side of the coils are then thermally contacted to a water-cooled copper heat sink with a diamond-filled epoxy glue. Details on the coil design as well as the exact form of the magnetic field can be found in [Lom08, Zür09].

Each coil is connected to one power supply (SM15-400, Delta Elektronika) that can deliver 400 A and is voltage-controlled by the experimental control system (ADwin). For active feedback we measure the sum and the difference of the

two currents with two current transducers (Danfysik 866 and LEM IT1000). This allows us to independently set the magnetic field and a magnetic field gradient [Zür09, Ber13]. Furthermore we can switch the coils to an anti-Helmholtz configuration and create magnetic field gradients of up to 250 G /cm for the detection of single atoms in the MOT.

3.3 The microtrap setup

The microtrap setup is the center part of all our experiments. It allows us to prepare few fermions in the ground state of one or several potential wells [Ser11a, Mur15b]. The microtrap is generated by a far-red detuned, tightly focused optical dipole trap. A first version is described in [Zür09] with a waist of 1.8μm. With that setup, the deterministic preparation of few-fermion systems was demonstrated [Ser11b].

In an upgrade [Ber13], we added a custom-designed high-resolution objective [Ser11a, Ber13] to create even smaller beam waists together with an acousto-optic deflector (AOD) [Kli12] to allow for the creation of several microtraps next to each other [Zim11]. Details on the optical setup after the upgrade can be found in [Kli12, Ber13]. This section will explain the necessary experimental steps to create and control one or two microtrap potentials.

3.3.1 Generating the microtrap potential

Our microtrap consists of a single-beam optical dipole trap [Gri00]. We use coherent light from a Mephisto laser at a wavelength of 1064 nm which we focus down to a micrometer-size. The shape of the resulting potential $V(\mathbf{r}) = V_0 \, I(\mathbf{r})$ is fully determined by the intensity distribution of the focused beam and the potential depth V_0 can be calculated according to equation 3.3. The ideal intensity distribution of the focused Gaussian beam can be described by

$$I(\mathbf{r}) = \frac{2\,P}{w(z)^2}\exp\left(-2\,\frac{x^2+y^2}{w(z)^2}\right) \tag{3.4}$$

with the total power light power P. The $1/e^2$-beam waist spreads along the propagation direction like

$$w(z) = w_0\sqrt{1 + (z/z_{\mathrm{R}})^2} \tag{3.5}$$

with the beam focus situated at $z = 0$ and the Rayleigh length $z_{\mathrm{R}} = {w_0^2 \pi}/{\lambda}$. As a consequence of the small focus, a beam power of only 0.4 mW already leads

wavelength	$\lambda = 1064\,\text{nm}$	$\lambda = 671\,\text{nm}$
focal length	$20.3\,\text{mm}$	$20.3\,\text{mm}$
image distance	∞	∞
diameter field of view	$200\,\text{µm}$	$200\,\text{µm}$
max. diffraction limited NA	0.6	0.6
entrance aperture diameter at max. NA	$24.4\,\text{mm}$	$24.4\,\text{mm}$
resolution	$1.08\,\text{µm}$	$0.68\,\text{µm}$
waist of focus	$0.72\,\text{µm}$	$0.45\,\text{µm}$

Table 3.1: The nominal design parameters of the high-resolution objective. Taken from [Ser11a].

to trap depths of several μK and trap frequencies around few kHz. The trap frequencies can be calculated by a harmonic approximation around the minimum of the potential [Gri00]. We obtain $\omega_\perp = (4V_0/mw_0^2)^{1/2}$ and $\omega_z = (2V_0/mz_R^2)^{1/2}$. This results in an aspect ratio of $\eta = \omega_\perp/\omega_z = \sqrt{2}w_0\pi/\lambda$.

High-resolution objective

To achieve large trap frequencies and a small aspect ratio, we focus the 1064-nm trapping beam with a high-resolution objective of NA=0.55. Reaching a beam waist on the order of the wavelength requires a performance of the objective at the diffraction limit. As, the intensity distribution of the focus fully determines the shape of the trapping potential, great care was put into the design of the objective. It was custom designed by F. Serwane and is described in detail in [Ser11a].

The high-resolution objective consists of five lenses and sits outside the vacuum with a distance of 2 mm to the 6-mm thick vacuum window of the re-entrant viewport. Its focal length of 20.3 mm allows the trapping of atoms in the center of the vacuum chamber. The nominal design parameters are listed in Table 3.1. They are expected for a perfect alignment of the five lenses in the mount, as well as a good alignment of the lens system to the vacuum window.

In the course of the Master Theses [Kli12, Ber13] the objective was tested and then implemented in the experimental setup and we achieved a beam waist of $\approx 1.6\mu$m. At that time, we were aware of an imperfect alignment procedure. Therefore, when we had to remove the objective due to problems with the Feshbach coils, we re-investigated the alignment between objective and vacuum window. In a test setup, we found the optimal tilt between the objective and the vacuum window by optimizing the resolution of a point source with a size of 650 nm. With the optimal angle, we reached a resolution of ≈ 0.9ʮm at a wavelength of

671 nm. The smallest foci that we could create with a 1064-nm laser beam with a beam diameter of 19.9 mm where about 1.1μm [Deh16]. However, we observed an astigmatism on the beam which may be caused by the objective.

After that, we implemented the objective with the optimal angle to the vacuum window using an interferometer (see Figure 3.7). The better alignment decreased the waist of the microtrap significantly. When imaging single atoms via their fluorescence signal with the objective, we could also observe an astigmatism for the imaging light.

Creating a small focus

Apart from the numerical aperture and the optical performance of the objective, the focus size of the microtrap is influenced by the quality of the trapping beam. To monitor this, we used a shear plate interferometer and observed wave front errors smaller than $\lambda/4$ [Ber13].

Additionally the focus waist is dependent on the size of the incidenting beam. A larger beam leads to a more uniform illumination and thus to a smaller focus. We chose a beam diameter of 19.9 mm [Kli12] which is truncated by the entrance aperture of the objective. The truncation ratio $T = {w_0}/{r_{\mathrm{ap}}}$ therefore corresponds to $T = 0.8$ and leads to a lower limit of the focus waist of 0.84μm. In reality, we do not achieve such small values.

The aspect ratio of the trap influences the effective dimensionality of the system. Wit the nominal values, we expect an aspect ratio of $\eta \approx 3.5$. This means that for atoms in the lowest quantum states, the radial degree of freedom is frozen out and they behave according to a one-dimensional system. If the filling of the trap becames larger than the aspect ratio, also radial degrees of freedom are occupied and the system can be considered as three-dimensional. To perform experiments with larger atom number in the one-dimensional regime, we have to increase the aspect ratio of the trap again. In [Deh16], we investigated how we can increase the aspect ratio of the microtrap by truncating the trapping beam with an additional motorized aperture.

Determining the trap parameters

To characterize the trapping potential experienced by the atoms, we measure the trap frequencies by parametric heating of two atoms in the ground state at a fixed power. To do this, we prepare two fermions in the ground state of the trapping potential. Then we sinusoidally modulate the potential depth with an amplitude much smaller than the trap depth. If the modulation frequency corresponds

to twice the trap frequency the second excited trap level gets populated[4]. By measuring the ground state population at different modulation frequencies, we can determine the trap frequencies in axial and radial direction. Details can be found in [Ser11a, Zü12a, Ber13]. Based on these measurements and the overall light power[5], we can calculate the aspect ratio and also deduce the size of the focus. The trap parameters used in this thesis can be found in B.

3.3.2 Creation and control of multiwell potentials

Together with the high-resolution objective, we also implemented a new optical setup to create multiwell potentials. This setup allows us to prepare two atoms in the ground state of a double-well potential [Mur15b]. In the following, we will give a short overview over the setup. More details can be found in [Kli12, Mur15a].

AOD and optical setup

We create multiple potential wells with an Acousto-optic deflector (AOD, IntraAction) which is driven by a radio-frequency signal. For this, we send the trapping beam through the AOD where a fraction of the beam gets deflected by an angle proportional to the frequency of the input signal. The intensity of the deflected beam is dependent on the amplitude of the radio-frequency signal. We block the undeflected part of the beam and use only the deflected light.

By applying a signal consisting of several different frequencies, similar to [Zim11], we can create several beams propagating with different angles. Each of these beams is then expanded to a diameter of 19.9 mm using a telescope. After that, the beams are focused by the objective and their different angles of incidence are mapped to different positions in the focal plane.

Our AOD works in a frequency range between 25 MHz and 55 MHz. This range allows us to vary the microtrap positions within 10 μm. To perform tunneling experiments as presented in Section 6 the distance d between the wells is on the order of $d = 1.25\,w_0$. Consequently, up to 6 potential wells can be created next to each other in the setup. Additionally, the AOD can deflect a beam in two perpendicular directions which allows in principle to create arrays of 6×6 wells next to each other. However, we are only using one axis of the AOD.

The detailed optical setup is shown in Figure 3.7. A laser beam with 1.3 mm diameter exits a fiber collimator. After cleaning the polarization, the beam enters the AOD where it gets deflected. The deflected part is then expanded in a

---

[4]If we modulate the position of the microtrap, we can drive transitions into the first excited trap level.

[5]The objective transmits 95% of the trap light.
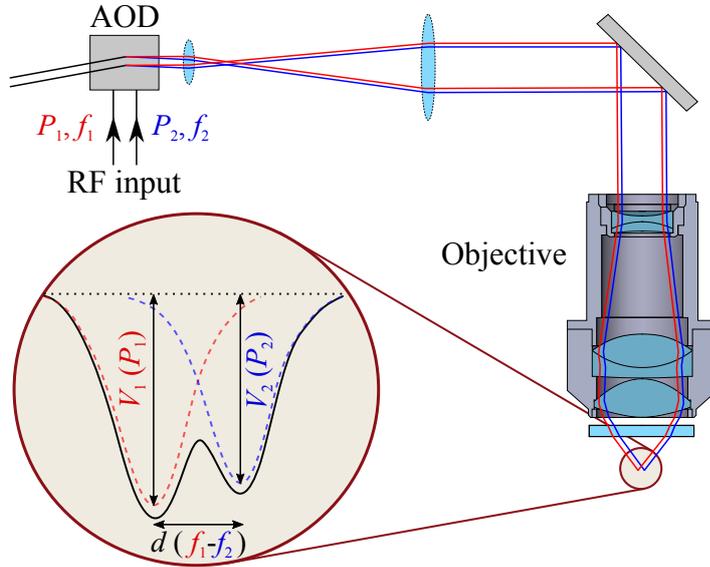
Figure 3.6: A microtrap setup to create multiple wells. The trapping beam passes through an Acousto-optic deflector (AOD) where it gets deflected by an angle proportional to the driving frequency. By controling the signal amplitude, we can change the light power in the deflected beam. By applying two signals with different frequencies, we create two beams. They get expanded by a telescope and focused into the science chamber, where the different angles result in different positions of the two foci. In this way, we create a double-well potential with controllable relative depth. Figure taken from [Mur15a].

telescope and sent to the objective. For aligning the objective, the setup contains a Michelson interferometer. Furthermore, the setup contains the stabilization of the light power to control the depth of the microtraps. For this purpose, we extract half of the power with a non-polarizing beam splitter and focus one half of it onto a photodiode with removed window. The measured power is fed back on an AOM (not shown in this setup) to regulate the total power. The other part of the power is focused onto a CMOS camera (PointGrey, Grasshopper GS3-U3-23S6M-C) for diagnosis and an eventual stabilization.

Creating a double-well potential for tunneling experiments

As a first step towards a finite-size lattice, we created a double-well potential. For performing tunneling experiments in this double well, a high control of the
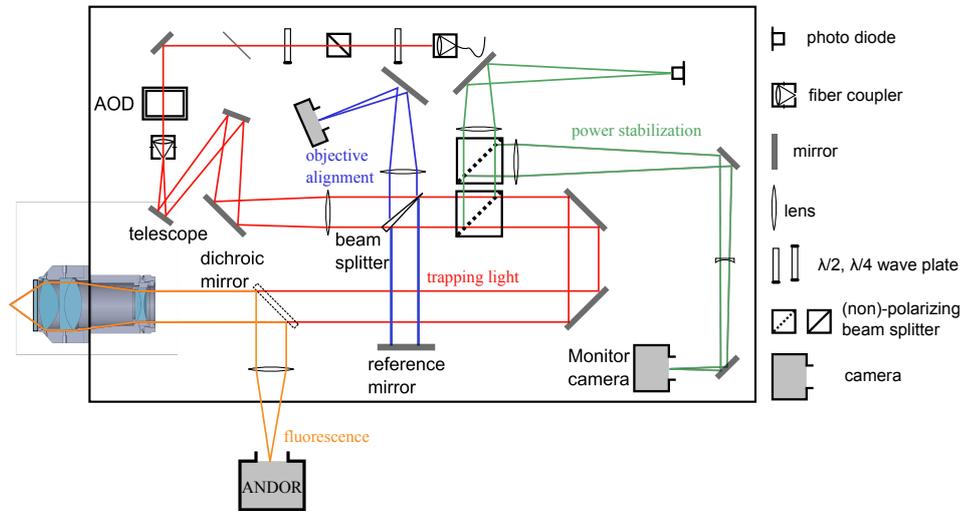
Figure 3.7: Optical mictrotrap setup. The trapping beam passes an AOD,
where it gets deflected. After that, the beam gets expanded in a telescope.
A small part of the light power is split off with a beam splitter for alignment
purposes. A non-polarizing beam splitter devides the rest of the light power
equally. One part of the beam is then used for power stabilization on
a photodiode whereas the other half gets focused with a high-resolution
objective and serves as a microtrap.

potential shape and stability of the wells is crucial. Especially the relative depth
between the two wells has to be stable enough to allow the observation of tunnel
oscillations (see Section 6)

To create a double-well potential, we apply a radio-frequency signal with two
frequencies f_1 and f_2 to the AOD. The generation of the signal is shown in Figure
3.8. We start with two signals from two outputs of a function generator (Rigol
DG4062). These output signals are permanently kept at the same power. We
mix each signal with a DC-voltage generated by an analog output channel of
the experimental control to tune the amplitudes A_1 and A_2 of the two signals
separately. Then, the two signals pass two switches that enable us to turn off
the beams separately from each other. After that, the two signals are combined,
amplified and applied to the AOD.

The radio-frequency signal generates two deflected beams that are focused by
the objective to two partly-overlapping potential wells. The resulting trapping
potential is determined by the intensity distribution of the far-red detuned laser
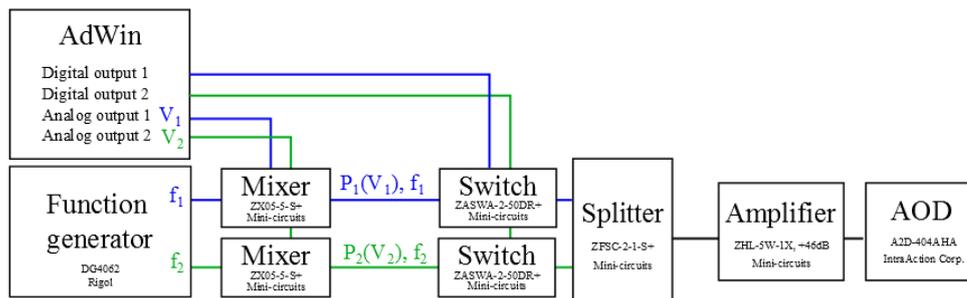
Figure 3.8: Radio frequency setup to create multiple potential wells.
We use a function generator to create two radio-frequency signals with
different frequencies f_1 and f_2. We control the power of each signal P_i by
mixing it with a DC-voltage V_i controlled by the experimental control AdWin.
Two switches controlled by TTL signals allow to separately switch off the
signals. After that, we combined the signals with a splitter used in reverse
mode. After an amplification we apply the signal to the AOD.

light

$$
V(\mathbf{r}) = V_0 \left[\frac{2\,P_1}{w(z)^2} \exp\left(-2\,\frac{(x - d/2)^2 + y^2}{w(z)^2} \right) + \frac{2\,P_2}{w(z)^2} \exp\left(-2\,\frac{(x + d/2)^2 + y^2}{w(z)^2} \right) \right].
$$
(3.6)

We control the relative depth of the wells by tuning the amplitudes A_1 and A_2
of the two signals. To observe tunneling in the setup, the relative stability has
to be on the order of 10^{-4}. During all experiments presented in this thesis, the
relative depth of the two wells was not actively stabilized. Work on an active
stabilization using a camera with fast read-out is ongoing.

Generating the two frequencies with a function generator provides a high
frequency stability, in contrast to e. g. using voltage-controlled oscillators. This
stability turned out to be important as we observed a varying deflection efficiency
of the AOD as a function of the input frequency. On top of a slow variation
over several MHz, it shows sinusoidal fringes with a periodicity of $100\,\mathrm{kHz}$ and an
amplitude on the order of 1%. The fringes probabily stem from the cubic shape
of the AOD crystal that results in a reflection of the density modulation in the
crystal which leads to a standing wave. We did not observe a temporal variation
of the fringes. Nevertheless, the fringes can lead to instabilities if the frequency is
varying.

Summary

All in all, our deterministic preparation allows us to investigate few-fermion systems at various interaction strengths. Since an upgrade we can not only extend our investigations into multi-well potential systems but also profit from the new high-resolution objective. With its help, we achieved smaller foci of the microtrap. In addition, the objective can also be used to image the atoms with high resolution. In the next section, we will make use of this to achieve fluorescence imaging with single-atom resolution.

Chapter 4

Single-atom resolved imaging

For several years, we measured the prepared few-fermion systems by recapturing the atoms in the microtrap back in the magneto-optical trap (MOT) and counted them as described in Section 3.1.4. Extending the setup to multiple wells vastly increases the required measurement time that is needed to reconstruct the occupation statistics on each individual site. We therefore aimed for a versatile but simple imaging scheme that allows to detect single atoms with single-site resolution.

In this chapter, we report on a newly developped imaging scheme that offers single-atom detection with spin and position resolution. In order to achieve this, we collect fluorescence photons from the atoms which allows to identify individual atoms and determine their positions as well as their hyperfine spin state. By letting them expand before imaging, we gain access to the momentum distribution on a single-particle level. Providing information on a single-particle level, our method paves the way to detecting N-point correlation functions in complex many-body states.

The first section will give an overview on different single-particle detection schemes present in the literature and then introduces our approach of detecting single atoms via fluorescence. Then, we take a closer look on the resonant excitation of the atoms and the emission and detection of few fluorescence photons. After that, we give an overview on the image processing which allows to identify and localize individual atoms and resolve their hyperfine spin state. In the last part, we apply our imaging method after time-of-flight to measure the momenta of the individual particles.

4.1 Stategies on single-atom detection

Absorption imaging [Ket99] is widely used for imaging large clouds of ultracold atoms. To study microscopic physics, however, it is convenient to have single-atom sensitivity as it usually comes together with new observables that one can access. The prerequisites for single-atom detection depend on the specific experimental

setup and led to a varity of solutions to overcome the technical challenges. An overview on the current progress can be found in [Ott16]. In the following section, a few examples for single-atom detection will be presented, that are closely related to our approach.

Quantum gas microscopes

The creation of standing wave optical dipole traps and the successful preparation of ultracold atoms in low-temperature states opened a new branch in the field. Now, one could study the physics of solids by quantum simulation in a periodic potential. In this way, it was possible to observe the transition from a superfluid to a Mott-insulator in bosonic [Gre02]. To directly observe occupation statistics and spatial correlations in the quantum state, however, single-site resolution is needed.

   This drove the development of quantum gas microscopes [Bak09, She10, Omr15, Par15, Che15, Edg15, Hal15, Mir15]. Achieving the optical resolution is however challenging as for most experiments lattice spacings are on the order of 500 nm. To image the sample with single-site resolution, one thus needs a high-resolution objective and clever ways of image analysis to resolve individual sites [She10, Alb16]. For the image process, the atoms have to scatter several thousand photons which leads to heating. To keep the atoms from tunneling to neighboring sites, the optical lattice potential has to be increased to several hundred recoil energies and sophisticated cooling schemes have to be implemented. In addition, the presence of resonant light together with the deep lattice potentials lead to light-assisted collisions which cause the loss of pairs of atoms on the same lattice site. Consequently, without circumventing this problem [Pre15, Bol16], the atom number per site is parity projected.

   Despite these complications, quantum gas microscopes are nowadays one of the work horses in optical lattice experiments. They allowed the observation of the superfluid to Mott insulator transition with single-site resolution [She10, Gre16] or the detection of two-point correlations (e.g. [Che12]).

Direct atom detection and fluorescence imaging in time-of-flight

Experiments with metastable Helium achieve single-atom resolution by direct particle detection. After the preparation of the sample the atoms are dropped on a multi-channel plate (MCP). Due to their internal energy of about 20 eV the Helium atoms release electrons at the place where they hit the surface. These

electrons are then multiplied by the channels of the MCP and the signal can be read out with spatial and temporal resolution [Sch05]. This allowed to study higher-order correlations in Bose-Einstein condensates with single-atom detection in time-of-flight [Hod11, Fan16, Hod17]

In a similar way, one can detect alkali atoms in time-of-flight experiments with single-atom sensitivity as shown with Rubidium atoms in [Büc09]. Instead of an MCP, they use a thin sheet of resonant probe light that the atoms pass through during their free fall. An objective focused to the light sheet then collects the photons from the fluorescing atoms onto an electron-multiplying CCD (EMCCD) camera where several photons impinge on single pixels. By using dilute clouds one can then distinguish the individual atoms [Büc09, Per12].

4.1.1 Spin-resolved single-atom imaging in free space

Our single-atom imaging technique works similar to [Büc09]. We excite the atoms with resonant light and collect the fluorescence of the atoms with an objective. To keep our scheme as simple as possible, we do not use a cooling technique and image the atoms in free space.

In contrast to Rubidium [Büc09], imaging ^{6}Li-atoms is much more challenging due to their small mass. As a consequence, scattering a single photon corresponds to a recoil energy of 3.5μK and a velocity change of $10\,$cm/s. Scattering thousand photons in order to obtain a sufficient signal-to-noise ratio on the camera leads to a significant increase of the momentum of the atom and the initial position of the atom cannot be determined.

We developed a simple detection scheme that achieves single-atom resolution because of some compromises we could make:

Reduction of photon scattering We use a camera that can detect single photons. To identify an atom, we therefore only need to detect about 10 to 20 photons. A high-resolution objective enables us to collect about 10% of the scattered photons on the camera and thereby reduce the necessary scattering events to about 300. As a consequence, the typical size of the random walk of the atoms is only several μm in free space and makes a cooling scheme unnecessary.

Spin resolution We perform the imaging at magnetic fields above $500\,$G where the optical transitions for the used hyperfine states are almost closed. This prevents the atoms from scattering into a dark state. As a consequence we do not need an additional repumping laser beam and we can selectively address different hyperfine spin states.

Increase of well separation   Our trapping potentials are generated by an array of optical tweezers of typical waists of 1.2μm with distances around 1.5μm. Our setup (described in Section 3.3.2) allows to increase the distance between the tweezers dynamically up to $10\mu m$. Resolving individual sites is thus less challenging in our case.

Imaging in free space   After the preparation of few particles in multiple wells, we can also perform an expansion in the 200μm-large harmonic potential created by the optical dipole trap. With an expansion time of $T/4$ we access the momentum distribution [Mur14] where the typical distance of the atoms is much larger than the typical size of the random walk. This allows us to achieve single-atom resolution in momentum space, similar to [Büc09].

Our imaging setup is shown in Fig.4.1. The atoms are trapped in optical tweezers created by focused far-red detuned laser beams. We apply a magnetic field larger than $500\,$G in vertical direction and probe the atoms with two counterpropagating resonant beams with horizontal polarization. They stem from a diode laser (Toptica DL100) with fast current feedback that is stabilized by a beat-offset lock [Ste16]. In order to avoid a standing wave between the two laser beams, we interleave pulses of $200\,$ns length. The scattered photons are then collected by the high-resolution objective and separated from the trapping beams by a dichroic mirror. With a six-fold magnification we image the signal onto an EMCCD camera (ANDOR iXon DV887, back illuminated) with 16μm pixel size. The magnification is chosen such that an atoms causes a signal spread on several pixels with no more than one photon per pixel. To identify the photon events, we binarize the signal on the EMCCD and apply an image processing algorithm to identify and localize individual atoms. The next sections will explain each of these experimental steps in detail.

4.2 Fluorescence of a single atom

Our single-atom detection technique is based on fluorescence imaging. For exciting the atoms we use the D2 line going from the $2^2S_{1/2}$- to the $2^2P_{3/2}$-manifold. The natural lifetime of the excited state is about $27\,$ns which leads to a natural linewidth of $\gamma = 2\pi \times 5.87\,$MHz.

Assuming a two-level system and a coupling due to the electric component of the laser field, we can estimate the photon number that the atoms scatter as a
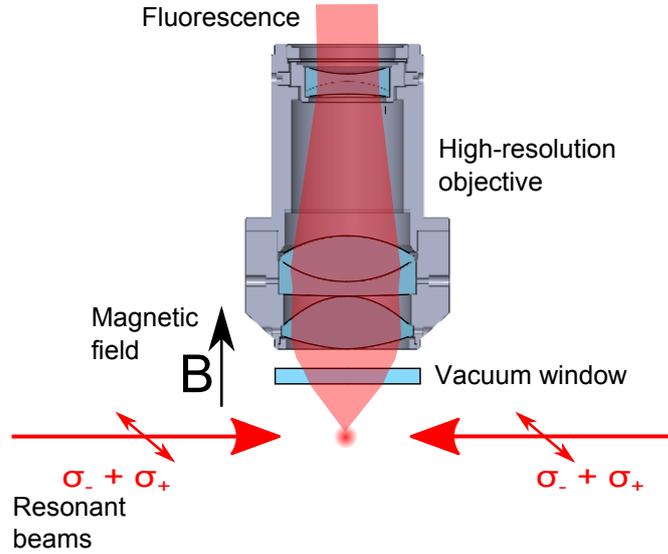
Figure 4.1: Imaging setup. We probe atoms trapped in the multiwell potential by resonant light with horizontal linear polarization. As the atoms experience a magnetic field in the vertical direction, the probe light can excite the σ-transitions in the atom. To avoid a standing wave, we pulse the two beams alternatingly with 2.5 MHz. We collect about 11.4% of the emitted photons with a high-resolution objective (NA= 0.55) and image them with a sixfold magnification onto an EMCCD camera.

function of exposure time. The total photon scattering rate is

$$\Gamma_{\mathrm{sc}} = \frac{\gamma}{2} \frac{s}{1 + s + (2\delta/\gamma)^2} \tag{4.1}$$

where γ denotes the natural linewidth and δ quantifies the detuning from the resonance. The saturation parameter $s = I/I_{\mathrm{sat}}$ quantifies the light intensity I by normalizing it with the saturation intensity $I_{\mathrm{sat}} = 2.54\,\mathrm{mW/cm^2}$. Equation 4.1 describes the scattering resonance with a width depending on the saturation $\gamma' = \gamma\sqrt{1+s}$. For strong driving, the scattering rate reaches $\gamma/2 = 18.4$ photons/μs and the width γ' gets infinitely large. For subsequently adressing two different hyperfine levels, it is not advantageous to choose such high intensities. Therefore we decided to use a saturation of $s = 8.5$ which results in a rate of 16.5 photons/μs. For a probe pulse of 20μs this results in about 300 scattering events.
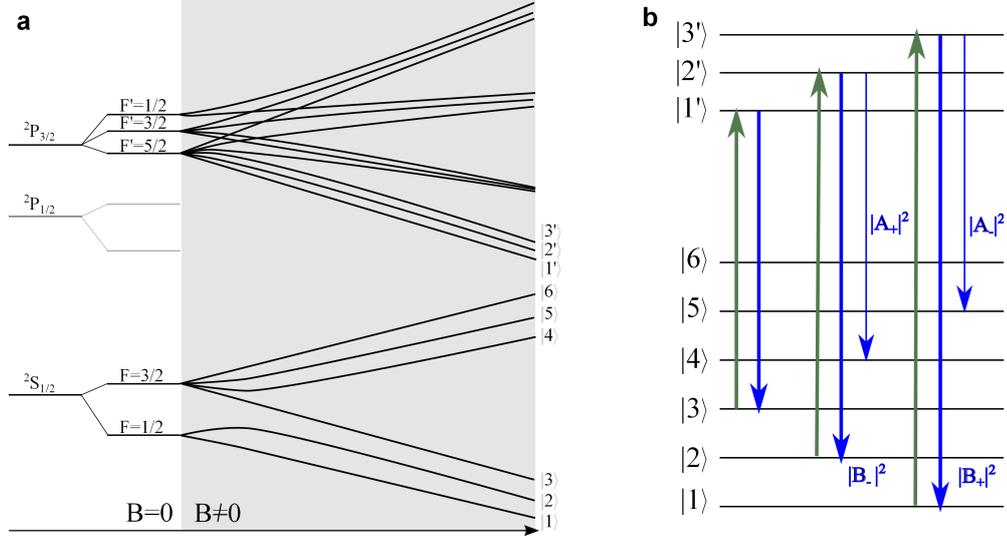
**Figure 4.2: Level scheme of the hyperfine states of ^{6}Li. a)** A sketch of the hyperfine states of ^{6}Li. For imaging single atoms we use the D2-line. The nuclear magnetic moment of $I = 1$ causes the depicted hyperfine splitting. Already at relatively low fields ^{6}Li enters the Paschen-Back regime and the levels regroup according to m_J. **b)** We work with the three lowest hyperfine states $|1\rangle$, $|2\rangle$ and $|3\rangle$ and drive a σ_--transition to the three lowest states in the excited state manifold. From there the atoms decay back to the initial states. With probabilities on the order of 10^{-3} they can also decay to $|4\rangle$ and $|5\rangle$, where they are lost for the imaging process.

4.2.1 The hyperfine level structure of ^{6}Li

In order to efficiently detect a single atom, it is crucial that the atom does not get dark to the probe light during this scattering process. Even a small probability p_{loss} to lose the atoms into a state not adressed by the probe light can significantly reduce the signal because the probability to find the atom in the initial state after N scattering events is $P_N = (1 - p_{\text{loss}})^N$. For this reason we have to understand the complex level structure of ^{6}Li to chose the most suited parameters.

^{6}Li has a nuclear magnetic moment of $I = 1$. Its coupling to the electron angular momentum J leads to the hyperfine structure depicted in Fig.4.2. The quantum number of the total angular momentum F can take integral numbers from $|J - I| \leq F \leq (J + I)$. So, the ground state manifold splits into two manifolds $F = \{1/2, 3/2\}$ and the excited state into three manifolds $F' = \{1/2, 3/2, 5/2\}$. Each of these manifolds consists of degenerate magnetic sublevels m_F. The presence of a magnetic field lifts this degeneracy.

For low magnetic fields B the hyperfine coupling $\mathbf{F} = \mathbf{J} + \mathbf{I}$ is dominant and $|F, m_F\rangle$ are good quantum numbers. In this regime the level spacing tunes proportional to m_F and B. As soon as the magnetic field gets on the order of the hyperfine coupling strength $\mathbf{I}$ and $\mathbf{J}$ start to decouple. Consequently $\mathbf{F}$ ceases to be a good description and the levels start to bend and group according to $|m_J, m_I\rangle$ (see Fig.4.2). In ^{6}Li the decoupling of $\mathbf{I}$ and $\mathbf{J}$ already happens at very low fields. For the ground state manifold the internal and the external magnetic fields have similar strength at around $30\,\text{G}$. For the excited state $2^2P_{3/2}$, this happens even below $1\,\text{G}$.

At high magnetic fields, where we image the atoms, it is convenient to chose the basis vectors $|m_J, m_I\rangle$. To obtain the eigenstates, we diagonalize of the Hamiltonian which contains the hyperfine coupling as well as the coupling to the external field. For the ground state manifold, the eigenstates can be expressed analytically [Geh03]

$$
\begin{aligned}
|1\rangle &= A_+ \left|^{1}\!/_{2}\,,0\right\rangle - B_+ \left|^{-1}\!/_{2}\,,1\right\rangle \\
|2\rangle &= A_- \left|^{1}\!/_{2}\,,-1\right\rangle - B_- \left|^{-1}\!/_{2}\,,0\right\rangle \\
|3\rangle &= \left|^{-1}\!/_{2}\,,-1\right\rangle \\
|4\rangle &= B - \left|^{1}\!/_{2}\,,-1\right\rangle - A_+ \left|^{-1}\!/_{2}\,,0\right\rangle \\
|5\rangle &= B_+ \left|^{1}\!/_{2}\,,0\right\rangle - A_- \left|^{-1}\!/_{2}\,,1\right\rangle \\
|6\rangle &= \left|^{1}\!/_{2}\,,1\right\rangle
\end{aligned}
\tag{4.2}
$$

The coefficients $A_\pm$ and $B_\pm$ can be understood as mixing angles that depend on the magnetic field[1]. For increasing magnetic fields $A_\pm$ decreases and eventually converges to zero. The states $|3\rangle$ and $|6\rangle$ do not have an admixture of a second $|m_J, m_I\rangle$-component.

For the excited-state manifold, the Hamiltonian can be diagonalized numerically. As in the $2^2P_{3/2}$-manifold, the nuclear and the electron angular momentum decouple around a magnetic field of $1\,\text{G}$, the mixing coefficients of the excited states can be neglected at magnetic fields around $500\,\text{G}$.

4.2.2 Optical dipole transitions

Starting in the three lowest hyperfine states $|1\rangle$, $|2\rangle$ and $|3\rangle$ we find nearly closed transitions by using σ_--polarisation that drives the atoms from the $m_J = -1/2$

---

[1]The coefficients are described by $A_\pm = 1/\sqrt{1 + (Z^\pm + R^\pm)^2/2}$ and $B_\pm = \sqrt{1 - A_\pm}$ where the parameter $Z^\pm = B\,(\mu_n + 2\mu_e)/A_{2^2S_{1/2}} + {}^{1}\!/_{2}$ is dependent on the magnetic field and $R^\pm = \sqrt{(Z^\pm)^2 + 2}$. Furthermore, μ_n denotes the nuclear magnetic moment, μ_e is the electron magnetic moment and $A_{2^2S_{1/2}} = 152.14\text{MHz}$ is the magnetic dipole constant.

to the $m_J' = -3/2$ manifold. From there the atoms can only decay back to the $m_J = -1/2$. In the following, we will denote the three adressed excited states with $|1'\rangle$, $|2'\rangle$ and $|3'\rangle$, where

$$|1'\rangle = |-3/2, -1\rangle$$
$$|2'\rangle \rightarrow |-3/2, 0\rangle$$
$$|3'\rangle \rightarrow |-3/2, 1\rangle$$

In the experiment we can drive σ_--transitions by using two resonant beams that are probing the atoms from the side (see Fig.4.1). We chose a linear polarization perpendicular to the direction of the magnetic field. Consequently the atoms can scatter photons with σ_+ and σ_- polarization. However, the two transitions have a frequency difference on the order of $1.8\,\mathrm{GHz}$ at $500\,\mathrm{G}$ which allows us to selectively scatter σ_--photons.

The absorption of σ_--polarized photons change $\Delta m_F = -1$ of the atom and m_I is left unchanged. Atoms in state $|3\rangle = |-1/2, -1\rangle$ are then only transferred to $|1'\rangle = |-3/2, -1\rangle$ from where they decay back only into $|3\rangle$ (see Fig.4.2 b). Consequently the probability to loose the atom into another state $p_{\mathrm{loss},3} = 0$.

For atoms in the hyperfine states $|1\rangle$ and $|2\rangle$, photonic excitations to $m_J = -1/2$ are in principle possible due to the small contribution of $|1/2, m_I\rangle$. However, the transition is detuned by about $900\,\mathrm{MHz}$ at $500\,\mathrm{G}$ and therefore additionally suppressed by at least 10^{-4}. Consequently, we can assume that atoms in the three lowest hyperfine state are excited into $|1'\rangle$, $|2'\rangle$ and $|3'\rangle$ without loss into other states.

Atoms in the states $|2'\rangle$ and $|3'\rangle$ can however also decay into the hyperfine states $|4\rangle$ and $|5\rangle$ where they cease to scatter the probe light. The loss probabilities for these decays are $p_{\mathrm{loss},1} = |A_+|^2$ and $p_{\mathrm{loss},2} = |A_-|^2$ and are on the order of 10^{-3}. Fig. 4.3 a shows the loss probabilities of atoms initially in the hyperfine states $|1\rangle$ and $|2\rangle$ as a function of the magnetic offset field.

The finite loss probability into dark states has an influence on the signal from the atoms. Every scattering event exponentially increases the probability that an atom in state $|1\rangle$ or $|2\rangle$ is lost into a dark state. Consequently, the average signal from an atom saturates after a certain exposure time. As a function of the exposure time, one expects a number of scattered photons of

$$N_{\mathrm{scatter}} = \Gamma_{\mathrm{sc}}(s, \delta) \int_0^{t_{\mathrm{exp}}} (1 - p_{\mathrm{loss}})^{\Gamma_{\mathrm{sc}}(s,\delta)t'} \mathrm{d}t' \tag{4.3}$$

$$= \frac{(1 - p_{\mathrm{loss}})^{\Gamma_{\mathrm{sc}}(s,\delta)t'} - 1}{(1 - p_{\mathrm{loss}})}$$

To illustrate the influence of the signal loss, Figure 4.3 shows the number of scattered photons for an atom in state $|3\rangle$ and an atom in state $|1\rangle$ for two different
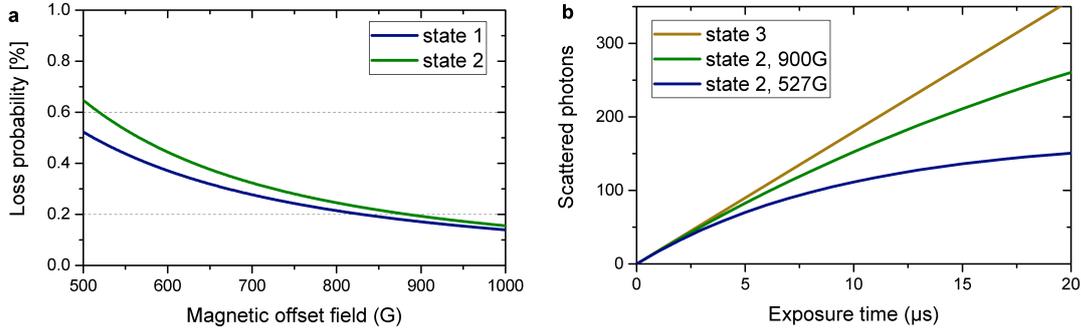
Figure 4.3: Loss probabilities. a) Probabilities to loose the atoms during the decay from the excited states back to $|1\rangle$ and $|2\rangle$ as a function of the magnetic field. The probabilites can be calculated analytically with eq. 4.2. Increasing the field from about $500\,\mathrm{G}$ to $900\,\mathrm{G}$ decreases the loss by more than a factor of two. The effect can be seen in **b)**. Depicted is the evolution of the mean scattered photon number as a function of the exposure time for state $|3\rangle$ (straight yellow line), and state $|1\rangle$ for $500\,\mathrm{G}$ (blue) and $900\,\mathrm{G}$ (green).

magnetic fields. The magnetic field has a large effect on the signal from atoms that are not in state $|3\rangle$. To maximize the signal strength for these states, we perform the single-atom imaging at $900\,\mathrm{G}$.

4.2.3 Collecting photons from a single atom

We can only collect a fraction of the scattered photons using a high-resolution objective. It has a numerical aperture of NA=0.55 and therefore covers a solid angle of about $1\,\mathrm{sr}$, or 8.2% of the full sphere. When decaying from the $m_J = {}^{-3}/_2$ states into the $m_J = {}^{-1}/_2$, the atoms emit σ_+ polarized light. The normalized dipole radiation pattern has an angular dependency on the azimuthal angle θ [DeM10]

$$I(\theta) = \frac{3}{16\pi}\frac{(1 + cos^2\theta)}{2} \quad . \tag{4.4}$$

This leads to an enhanced radiation along the direction of the magnetic field (for details we refer to [Bec16]). Consequently, we can collect 11.4% of the scattered photons with the objective. The photons are imaged with a lens onto an EMCCD camera. To block infrared light from the microtrap beam and the optical dipole trap laser, we cover the camera with a bandpass filter (Semrock, FF01-675/67-25). We estimate that the optics including the objective coating and the filter reduce the number of photons by 10%. The photons that arrive on the CCD-chip are
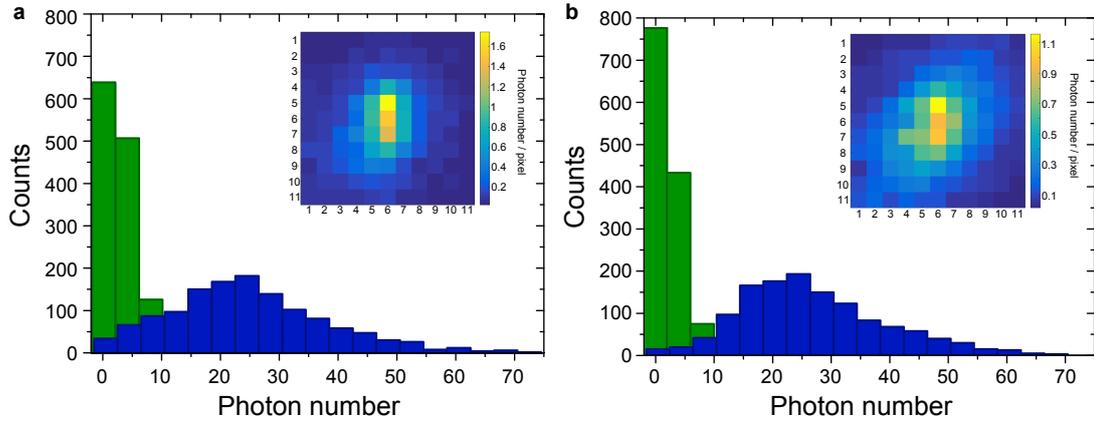
Figure 4.4: Number of detected photons. a) Histogram of the detected photons from one atom in state $|1\rangle$ (blue bars) and signal from a control region of the same size (green bars). The signal was detected in a ROI of 13×13 pixel. The loss probability of the atom is visible in the photon number distribution that is enhanced for lower photon numbers. **b)** Signal from one atom in state $|3\rangle$ (blue bars) and a control region (green bars). The probability for low photon numbers is smaller as atoms in state $|3\rangle$ are not lost into dark states during the scattering. The width of the photon distribution is slightly larger due to a finite probability of off-resonant scattering during the first pulse.

then detected with a quantum efficiency of about 85% (for details, see [Bec16]). In total, the average fraction of detectable photons is about 8.7%.

For an exposure time of 20μs we expect to detect in average about 28 photons from one atom in state $|3\rangle$. To measure the photon number per atom we prepare an atom in state $|3\rangle$ in the ground state of the microtrap and probe it with a resonant laser beam at a magnetic offset field of 900 G. The emitted photons impinge on the camera within a region of a few pixels and from the signal, we can infer the number of photons. Due to the statistic nature of the emission process, we expect a Poisson-like photon number distribution.

Figure 4.4 b shows a histogram of 1000 repetitions of the detected signal from one prepared atom in state $|3\rangle$. The inset shows the mean spatial distribution of the detected photons. To obtain the signal in units of the photon number, we correct the raw image for a present bias, then integrate over a region of interest (ROI) of 13×13 pixels and devided that value through the photoelectron gain of the camera (for details see Section 4.3.1). To show the influence of background signal on the data, we show the signal of an empty region on the camera with the

same size in green. The photon distribution from the atom in state $|3\rangle$ has a mean photon number of $N_p \approx 23$ and a width of $\approx \sqrt{2}N_p$. The factor $\sqrt{2}$ is caused by the stochastic nature of the photoelectron detection. The exact distribution can be deduced by stochastic modeling of the EMCCD camera [Hir13].

Figure 4.4 a shows the corresponding histogram for an atom in state $|1\rangle$. Due to the finite loss probability into dark states the mean photon number is slightly reduced compared to the signal from state $|3\rangle$. Additionally, we detect more events with lower photon number as an atom that entered the dark state at some point, will not scatter any more photons. However, in both cases the signal from the atom can be clearly distinguished from the background.

4.2.4 Diffusive motion

For an atom that emits photons from a fixed position, the width of the photon signal is governed by the optical resolution of the microscope objective. This is not the case for a free atom that scatters photons. With every scattering event, the momentum of the atom is changed in a random direction and the atom performs a three-dimensional random walk during the imaging process similar to a diffusion.

For a symmetric random walk, the mean of the atom's position distribution coincides with the initial position but the variance grows with time. The spread of the variance depends on the transferred momentum at each scattering event as well as the time between the individual scattering events, which is determined by the scattering rate. In the experiment, we measure the spread of the photon signal integrated over the full exposure time. We are only interested in a typical width of the integrated signal. To extract this, we average the spatial distribution of the photon signal from one atom and fit it with a Gaussian distribution. For an exposure time of 20μs, we find a width of (2.1 ± 0.3) pixel, which corresponds to $(5.7 \pm 0.8)\mu$m.

A jitter of the initial atom position from shot to shot leads to an additional increase of the width of the measured averaged signal. To estimate the influence of this process, we compare the typical width of the distribution on individual images σ_{ind} with the size of the averaged distribution σ_{mean}. To obtain a measure for the width of the individual distribution independent of their center-of-mass position, we apply an autocorrelation on each individual image. We compare it with the width of the autocorrelated averaged distribution to quantify the jitter of the initial atom position. We fit the two distribution with a Gaussian and find $\sigma_{\text{mean}}/\sigma_{\text{ind}} = (1.12 \pm 0.02)$. This excludes a significant jitter of the microtrap position with respect to the objective.

With a Gaussian width of 5.7μm, the photon signal is too large for a site-resolved detection of two atoms in a double-well potential. Even when we increase the

well spacing to 10μm, it may be challenging to achieve high fidelities for the site-resolution. Therefore, we want to decrease the diffusion of the atom during the imaging process. For this, we have to trap the atom at its initial position while it scatters photons by increasing the depth of the microtrap to values much higher than the recoil energy. As the microtrap potential is attractive for the ground state and the $2P_{3/2}$ excited state of the atom [Saf12, För15], the atom sees an average attractive potential $(U_g + U_e)/2 \approx 0.8 U_g$ and stays confined for a number of scattering events before it has gained enough energy to leave the microtrap potential.

We measure the reduction of the diffusion by imaging the atom in a single microtrap ramped to depths of several recoil energies. Figure 4.5 shows the signal for different trap depths after an exposure of 15μs. During this time, about 260 photons have been scattered. We observe that for trap depths larger than $100 E_R$ the signal is confined to few pixel. In Fig. 4.5 b the evolution of the fitted gaussian width of the signal is plotted as a function of the exposure time for two different depths. Their difference amounts to almost a factor of 2 and the width for the deep trap stays around 1μm.

This is promising for insitu measurements with dynamically separated wells. However, in our current double-well configuration we cannot increase the potential depth to sufficiently high values. In the following, we will establish a single-atom resolved imaging in free space.

4.3 Identification, localization and spin resolution of single atoms

In the last section we showed that we expect a stochastic signal of in average 20 photons per atom that is spread over several pixels. Based on this signal, we want to identify single atoms and determine their position. To do this, we use our EMCCD camera as single-photon detector and apply a binarization threshold to the raw data to identify pixels that detected a single photon. After this binarization, the image contains stochastically distributed events that are caused by camera noise together with clusters of events caused by fluorescing atoms. To identify the clusters of events as signals from a single atom, we apply a Gaussian low-pass filter and chose a width that corresponds to the width of the photon signal. The filtered image shows local maxima at positions were several events clustered. We extract the amplitudes of the local maxima as they serve as a measure for the cluster size. A histogram of the amplitudes shows a bimodal distribution which allows us to identify signals from single atoms. At the same
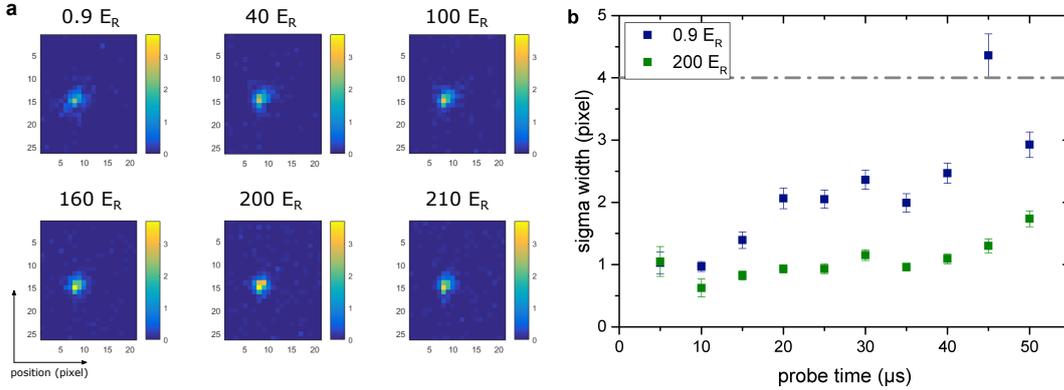
Figure 4.5: Fluorescence signal from atoms imaged in a microtrap.
a Mean fluorescence distribution of one atom in units of photon number
for different trap depths after an exposure time of 15μs. For configurations
deeper than $100E_\mathrm{R}$ the signal is stronger confined to few pixels. **b** Gaussian
width of the signal as a function of exposure time for two different depths.
In contrast to the shallow trap, the signal from the deep trap stays confined
to about 1μm.

time, the filtered image allows us to determine the position of the atom signal.
The following section reports on the image processing to identify single atoms and
determine their position.

4.3.1 Detection of single photons

When photons impinge on a semi-conductor based camera, they cause photoelec-
trons that can be measured with an electronic circuit. Electronic circuits have
read noise on the order of 2 to 10 electrons which makes the detection of a single
photoelectron impossible. To circumvent this limitation, an EMCCD camera
features an additional electron-multiplication register, where single photoelectrons
on the individual pixels are multiplied before they are read out by the electronics.
In this way, an EMCCD camera achieves single-photon sensitivity.

The multiplication process however is stochastic and the distribution of sec-
ondary electrons caused by the multiplication of one photoelectron is distributed
exponentially. For an initial number of photoelectrons n, the number of secondary
electrons x is described by the Erlang distribution [Har12, Lan08]

$$P_n(x) = \frac{x^{n-1}\mathrm{e}^{-x/g}}{g^n(n-1)!}\theta(x) \tag{4.5}$$

where $\theta(x)$ is the Heaviside function and g denotes the gain of the multiplication and

63
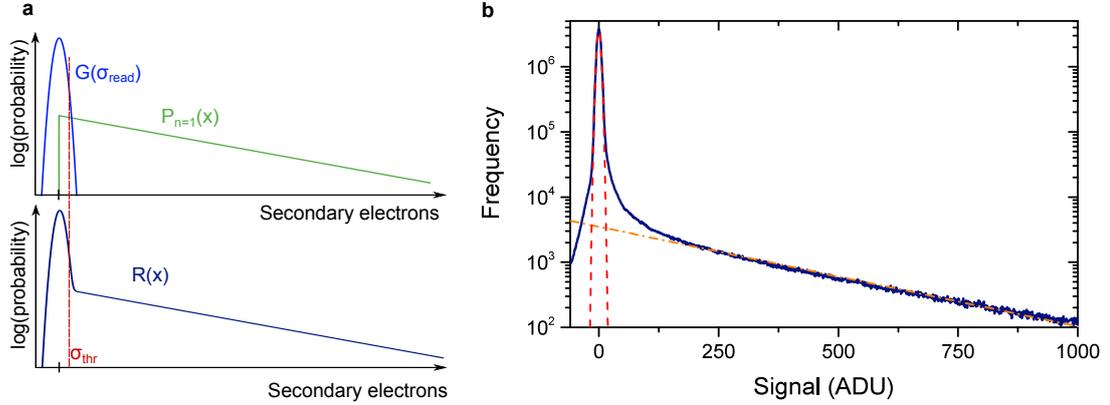
Figure 4.6: Histogram of the EMCCD signal. a) Schematic of the read noise (blue) and distribution of secondary electrons (green) created from a single photoelectron. A convolution leads to the distribution $R(x)$ which describes the distribution of the signal in the ideal case. **b)** Real signal distribution of an dark image. The red dashed line shows a Gaussian fit to the main peak to extract the read noise. The orange dashed line is a fit to the CIC to extract the gain.

corresponds to the $1/e$-width of the exponentially decaying number of secondary electrons for a single photoelectron. Figure 4.6 a shows a schematic of this distribution for a single photoelectron.

Although the detector does not allow exact counting of primary electrons, their signal can be clearly distinguished from read noise. The expected signal from the detector with p_0 pixels containing no photoelectron and p_1 pixels with one photoelectron is described by

$$R(x) = (G(\sigma_{\text{read}}) * [p_0 \delta + p_1 P_1])(x - b) \tag{4.6}$$

where $G(\sigma_{\text{read}})$ describes the Gaussian distributed read noise with a width of σ_{read} which is convolved with the distribution of secondary electrons (see Figure 4.6 a).

For the identification of photoelectron events from the raw image, a threshold value has to be determined above which the signal is identified with a detected photoelectron (see Figure 4.6 a). The optimal threshold σ_{th} minimizes both the probability to identify read noise as a photon event $P(0 \rightarrow 1)$ as well as the probability to not count an actual photon event $P(1 \rightarrow 0)$. The probability of wrongly identifying photon event $P(0 \rightarrow 1)$ can calculated by integrating the Gaussian distribution $G(\sigma_{\text{read}})$ from σ_{th} to ∞. Setting e. g. $\sigma_{\text{th}} = 3\sigma_{\text{read}}$ results in 0.135% wrongly identified events.

In the limit of a gain much larger than the read noise, the probability of missing a photon event can be calculated by

$$P(1 \to 0) = \int_0^{\sigma_{\mathrm{th}}} \frac{\mathrm{e}^{-x/g}}{g} \, \theta(x) \, \mathrm{d}x = 1 - \mathrm{e}^{-\sigma_{\mathrm{th}}/g} \quad . \tag{4.7}$$

This shows that a high gain and at the same time a low σ_{read} are essential for a high detection fidelity of a single photon. For $g/\sigma_{\mathrm{read}} = 90$, the optimal threshold is about $\sigma_{\mathrm{th}} = 2\sigma_{\mathrm{read}}$ with a resulting detection fidelity for one photoelectron of 97.5% and 2.5% of wrongly identified events.

In addition to the read noise, spurious charges are causing noise on the image. As they are multiplied in the same way as photoelectrons, their signal has the same distribution and consequently they cannot be distinguished from real events.

Spurious charges can be generated by photons from background light, thermal excitations or by the shifting process during the camera readout. The former two can be avoided by sufficiently shielding the experiment from stray light and using a bandpass filter on the camera and by cooling the camera chip[2]. The so-called clock-induced charges (CICs) caused by the shift process of the pixel rows are inherent to the readout of the camera[3].

We determine the noise from clock-induced charges by analysing a dark image. Figure 4.6 b shows a histogram of the signals from individual pixels. Although there is no stray light on the chip, we identify a distribution caused by multiplied electrons. By fitting an exponential function to the histogram, we determine about 2% of noise from the parallel transfer across the chip for our camera [Bec16, Bom17].

However, we observe that the fraction of pixels above the optimal threshold exceeds 2% and in the histogram, a significant part of the distribution lies above the fitted exponential function. These events can be attributed to CiCs that are generated in the serial multiplication register [Lan08]. Therefore, their distribution[4] differs from the one of a photo-electron. For serial CICs the effective gain is much lower and so their influence on the noise can be decreased by chosing a higher threshold. For all our evaluations we chose a threshold of $\sigma_{\mathrm{thr}} = 8\sigma_{\mathrm{read}}$ which results in about 3% of pixels above threshold on a dark picture. This choice reduces the photoelectron detection efficiency to 88.2%.

---

[2]For all data, presented here, we cooled the chip to -75° C.

[3]The amount of CICs depends on the wave form chosen for the shifting process. Optimizing this wave form the number of CICs can be significantly reduced [Dai10].

[4]These CICs can be generated at each cell of the register. The distribution is therefore a sum over all register cells m given by $p(x) = \sum_{l=1}^{m} \frac{p_s \exp(-x/p_c^{m-l})}{p_c^{m-l}}$ where p_c describes the duplication of one electron in each cell of the multiplication register.
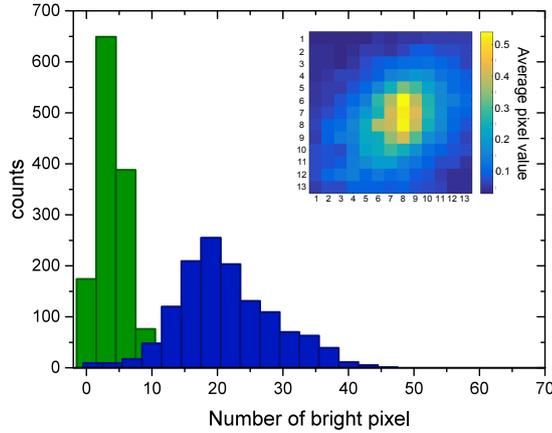
Figure 4.7: Number of bright pixels. Histogram of pixels above threshold for one atom in state $|3\rangle$ (blue bars). The signal was detected in a ROI of 13×13 pixel and we chose a threshold of $\sigma_{\mathrm{thr}} = 8\sigma_{\mathrm{read}}$. The signal from a control region of the same size (green bars) is in agreement with a CIC probablity of 3%. This results in 13 additional number of bright pixels from the fluorescence of one atom.

4.3.2 Identification of single atoms

After the binarization, the signal from one atom results in average in 13 bright pixels (see Figure 4.7) and spreads over a region with a Gaussian width of 2.5 pixel. Due to the photon shot noise from the fluorescence, the number of bright pixel varies from shot to shot and can also be significantly lower than 13. In order to achieve a high fidelity for the identification of single atoms, we apply an imaging processing that is sensitive to clusters of bright pixel.

Our strategy for the image processing of binarized pictures is show in Figure 4.8. We use the fact that the signal of an atom results in a cluster of bright pixels whereas the noise from the CICs is stochastically distributed over the image. To discriminate between the two, we apply a low-pass filter to the binarized data with a spatial frequency that corresponds to the typical cluster size. We use a Gaussian low-pass filter with a size of 3 pixel. After that, we search for all local maxima in the filtered picture. A histogram of the values of the local maxima found in 1000 pictures is shown in Figure 4.9. It shows a bimodial distribution where the right peak stems from maxima caused by the presence of an atom and the left peak is caused by maxima from spurious charges. The left peak increases with the size of the region that is evaluated. Based on the histogram, we chose a threshold value above which we count a local maximum as an event that was caused by an atom.

The fidelity of the atom identification is determined by the overlap of the two
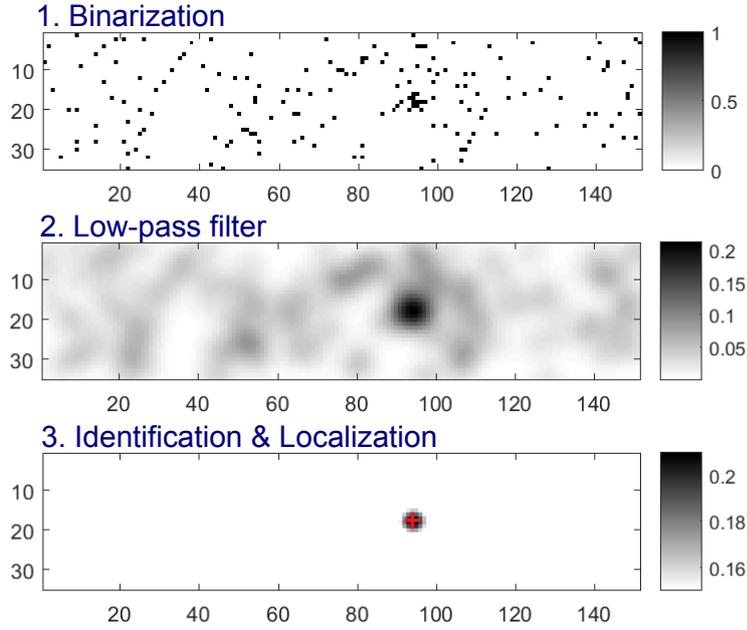
Figure 4.8: Identification of single atoms from raw pictures. We detect fluorescence photons of single atoms in the form of clusters of photo-electrons on the EMCCD camera. For the identification of single photo-electrons we set a threshold of $8\sigma_{\mathrm{read}}$ to the camera signal. We then apply a Gaussian low-pass filter on the binarized image with a width of 3 pixel and search for local maxima. Based on the histogram of Figure 4.9, we chose a threshold above which we identify a local maximum as an atom. Finally, we read out the central pixel of the maximum to localize the particle.

distributions. The more they overlap, the larger becomes the number of wrongly identified spurious charge events as well as the number of not identified atoms and the fidelity decreases. We can determine the latter by assuming that the atom peak has a Gaussian distribution and compare its width with the chosen threshold. For the data shown in Figure 4.8 we chose the threshold to be at minimum value between the two distributions which is about 2.3σ below the maximum of the atom distribution. This corresponds to a probability to miss a true event of about 1%. The probability of wrongly identifying spurious charge is in the same range for the chosen size of the evaluated region. Consequently we detect an atom with a fidelity of 98%.

As an alternative approach to the low-pass filter is to use a likelihood method for the identification analysis. Details on the realization can be found in [Bom17]. The basic concept is to use all the available information in combination with
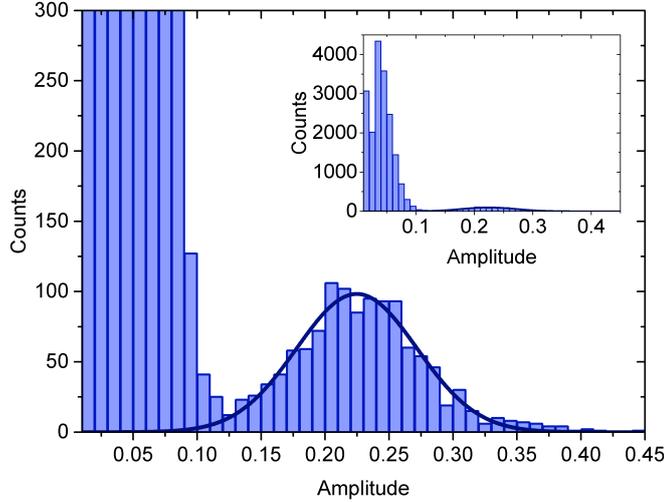
Figure 4.9: Identification of single atoms from raw picture. After the binarization and the application of the low-pass filter, we select a region of 150×25 pixel. In this region, we search for local maxima. We plot a histogram of their amplitudes for about 1000 pictures. The two distinct peaks represent the signal from spurious charges (left) and the signal from a single atom (right). Based on this, we set a threshold for the atom identification and obtain a detection fidelity of about 98%.

a hypothesis test. Instead of assuming a Gaussian distribution of the detected photons with the typical width, we measure the distribution of bright pixels caused by one atom in an insitu image. From this distribution, we identify a spatially dependent probability distribution for bright pixels $P_1(x_i, y_i)$ caused by an atom. In contrast, the probability distribution of spurious charges is homogeneous $P_0(x_i, y_i) = p_{\mathrm{CIC}}$. For a given event k we then calculate the probability that it was caused by an atom $P(k|H_1)$ or no atom $P(k|H_0)$ using the two hypothetical distributions P_0 and $P_1(x_i, y_i)$. As we have not prior knowledge about how often we expect the hypotheses H_1 and H_0 to be true, the calculated probabilities are estimates.

To give a quantitative estimate, we use the logarithmic likelihood ratio $\ln R = P(k|H_1)/P(k|H_0)$. We calculate it for every position of the hypothetic probability distribution on a large region. We then generate a histogram from these values R_{ij} which also shows a bimodal distribution, where one peak corresponds to signals from an atom and the other represents the signal from the spurious charges. In the same way than explained before we chose a threshold to identify the events cause by an atom. This method achieved higher detection fidelities also for large

regions-of-interest. However, in day-to-day use this method turned out to be unstable and often also led to much worse performances than the low-pass filter. Therefore, we used the low-pass method for all the data presented in this thesis.

4.3.3 Position determination of single atoms

Together with the atom identification we can also perform a position determination of the detected atom. For this we use the filtered images and extract the position of the local maximum as the coordinate of the detected atom.

The uncertainty of the position determination of the atom is influenced by the statistical fluctuation of the emitted photons. In addition, the atom performs a random walk during the photon scattering and the initial position does not necessarily correspond to the center of mass of the photon distribution.

In order to quantify the uncertainty in the position determination, we analyse images where the atom started its random walk at the position of the single microtrap. We apply our image analysis to each image and extract the position of the local maximum. From a histogram of 1000 realization, we can determine a spread of the local maxima with a Gaussian width of (1.36 ± 0.01) pixel which corresponds to 3.6μm. If the position of the microtrap is stable and therefore the initial position of the atom does not vary from shot to shot, the spread quantifies the uncertainty due to the stochastic detection process. In Section 4.2.4, we observed a jitter on the microtrap position that is at most 12% of the signal spread.

4.3.4 Hyperfine spin resolution

In addition to the identification of single atoms and the determination of their position, we can measure their hyperfine spin state. This is possible because we image the atoms at high magnetic fields, where optical transitions for each hyperfine state are almost closed (see Section 4.2) and the resonance frequencies differ by about $80\,$MHz.

Using a probe beam with moderate power, we probe first one hyperfine state and collect the fluorescence signal for $20 \mu s$ on the EMCCD. Then we shift the acquired photoelectrons vertically using the fast kinetic mode by 40 rows and simultaneously change the resonance frequency of the probe laser by $80\,$MHz or $160\,$MHz. $50 \mu s$ after the first probe pulse, we probe the system again, now being resonant to the other spin state. In this way we can probe atoms in two or all three lowest hyperfine states of one realization. Figure 4.10 shows a typical hyperfine-resolved image of two atoms in state $|1\rangle$ and $|3\rangle$.
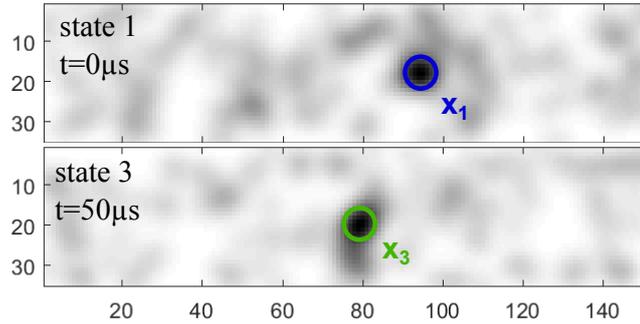
Figure 4.10: Hyperfine-resolved image of two atoms in different hyperfine state. We resolve the hyperfine state of individual atoms by probing them subsequently. After a first probe pulse of $20\mu s$ length, we shift the signal accumulated on the EMCCD camera vertically by 40 rows and change the frequency of the probe laser. $50\mu s$ later, we probe the second hyperfine state.

To change the frequency of the probe laser within $12\mu s$ by $160\,\text{MHz}$ is technically challenging. To achieve the fast frequency change, we change the current of the laser using the current modulation input. We stabilize the probe laser (DL100, Toptica) using a beat offset lock in combination with a RedPitaya that allows for simultaneous current and piezo feed-back. Details on the lock scheme can be found in [Tho16]. The local oscillator frequency of the beat offset lock is generated by a Direct Digital Synthesizer (DDS, Analog Devices AD9914) and changed by programming it with the help of an Arduino Due microcontroller. Details on the DDS control are presented in [Kra15, Ste16].

We chose moderate power of the probe beam to reduce the impact on the off-resonant spin state during the imaging. The number of off-resonantly scattered photons can be deduced from equation 4.1. The relative scattering rate is then

$$P_{\text{rel, scatt}} = \frac{1+s}{1+s+(2\delta/\gamma)^2} \xrightarrow{(2\delta/\gamma)^2 \gg s} \frac{1+s}{(2\delta/\gamma)^2} \quad . \qquad (4.8)$$

For a detuning of $160\,\text{MHz}$, an exposure time of $20\mu s$ and a probe beam intensity of $s = 8.5\,I_{\text{sat}}$, the off-resonant hyperfine state scatters in average 1.4 photons. After a scattering event, the offresonant atom moves with the velocity received from the photon recoil until it is imaged resonantely. The average distance it travels within $25\mu s$ until it gets imaged is about $5\mu m$. This is on the same scale than the uncertainty in the position detection.

4.4 Single-atom imaging in time-of-flight

In the last sections, we demonstrated that we can spin-selectively image single atoms in free space and achieve a position incertainty of about 1.4 pixel. This makes our technique perfectly suited for single-atom imaging after an expansion in time-of-flight. In that way, we gain access to the momentum distribution of the system on a single-atom level and can reconstruct the many-body wave function in momentum space.

4.4.1 Expansion into momentum space

For time-of-flight imaging, a trapped atom at $\mathbf{x_0}$ is released and travels according to its initial momentum $\mathbf{p_0}$. Its position as a function of time after the release can be described by

$$\mathbf{x}(t) = \mathbf{x_0} + \frac{\mathbf{p_0}}{m} t. \tag{4.9}$$

After a sufficiently long expansion time $\mathbf{p_0}/m\, t \gg \mathbf{x_0}$ and the position of the atom is dominated by its initial momentum $\mathbf{p_0}$.

If an atom is confined in the ground state of a three-dimensional harmonic potential its quantum state is described by a three-dimensional Gaussian wave function. According to Heisenbergs uncertainty principle, momentum wave function of the atom is also Gaussian with a width inversely proportional to the spatial confinement. In case of a release, the wave function of the atom expands in all three dimensions. For long exposure times, its size can exceed the depth of focus of the objective and the signal gets detoriated. This makes the identification of single atoms impossible.

We circumvent this problem by performing the expansion in a large confining harmonic potential. After an expansion time of a quarter of the oscillation period in this potential, the initial momentum wave function of the atom will be mapped to the spatial wave function. One can view this as a focusing of a matter-wave to access the fourier plane represented by the momentum distribution [Mur14].

Our high-resolution objective has a field of view with a diameter of 200μm and a focal depth of about 3μm. We avoid an expansion in the direction of imaging by confining the atoms in the crossed-beam optical dipole trap, shown schematically in Figure 4.11. In first approximation, this trapping potential is cigar-shaped. So the expansion times to reach the mapping of the momentum to space will depend on the direction. In addition to the automatic integration along the imaging direction, we also integrate over the other radial direction of the optical dipole trap. By chosing an expansion time of $t = T_{\mathrm{ax}}/4$ we access the momentum distribution along the axial direction of the dipole trap.
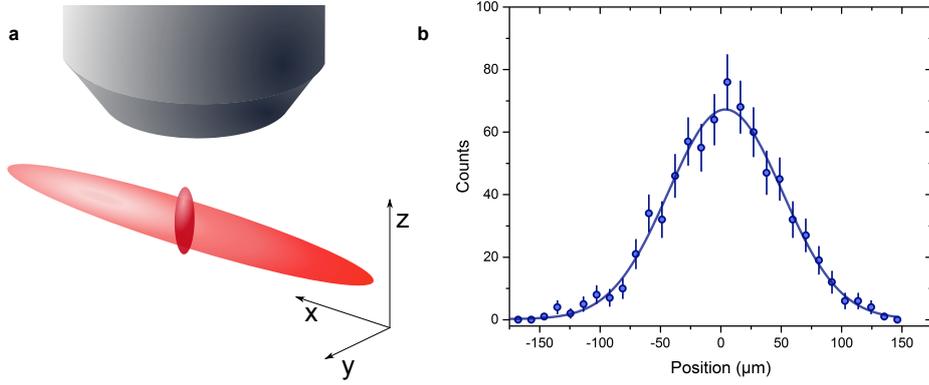
Figure 4.11: Expansion of a single particle in the optical dipole trap.
a) Distribution of the atoms for 800 realizations starting from one microtrap.
We prepared two non-interacting atoms in the ground state of the microtrap
released them. After an expansion time of 3.5 ms in the optical dipole trap,
we image them spin-selectively. **b)** Histogram of the axial position of a single
atom in 750 realizations. The distribution of the atom is governed by the
inital momentum distribution and consistent with a Gaussian distribution.

The intensity distribution of the optical dipole trap has a width of $\sigma_{\mathrm{rad}} = 25\mu m$
and $\sigma_{\mathrm{ax}} = 200\mu m$. We perform the expansion at a trap depth of 20μK which
results in trap frequencies of $\omega_{\mathrm{ax,ODT}} = 2\pi \times 73$Hz and $\omega_{\mathrm{rad,ODT}} \approx 2\pi \times 300$Hz. To
reach the momentum distribution along the axial direction of the optical dipole
trap, we chose an expansion time of 3.5 ms.

We demonstrate single-atom imaging in momentum space by preparing a single
atom in the ground state of the microtrap. Its spatial wave function has a radial
harmonic oscillator length of $a_{\mathrm{ho}} = \sqrt{\frac{\hbar}{m\omega_{\mathrm{rad,MT}}}} = 305$nm expands to a Gaussian
wavepacket with a width of $\sigma_{\mathrm{ODT}} = 53.3\mu m$ according to

$$\sigma_{\mathrm{exp,ODT}} = \frac{\sqrt{\hbar\,m\,\omega_{\mathrm{rad,MT}}(^1\!/_2 + n)}}{m\,\omega_{\mathrm{ax,ODT}}} \tag{4.10}$$

where m is the mass of the ^{6}Li atom and n is the principle quantum number. We
measure this expansion by multiple repetitions of the preparation and detection of
a single atom after time-of-flight. The result is shown in Figure 4.11 as a histogram
of the detected positions in the axial direction, where we integrated over the two
radial directions of the optical dipole trap. Fitting a Gaussian distribution results
in a width of (17.4 ± 0.4)pixel which corresponds to $(47.2 \pm 1.1)\mu$m. We observe a
discrepancy to the expectation that may be due to an overestimated magnification.

4.4.2 Impact of interaction

Until now, we considered the expansion of a single particle in the optical dipole trap. Imaging the momentum distribution of an interacting few-particle system is only possible if the interaction does not influence the expansion.

To estimate the impact of the interaction, we first calculate the density evolution of a single particle during the expansion. Using the equations from [Mur14], we obtain a rapid decrease of the density within the first microseconds after the release. After a time of $\tau = 1/f_{\mathrm{rad,MT}} = 300\mu$s, the density is reduced by more than a factor of thousand. However, the cigar shape of the optical potential and the expansion time of $3.5\,$ms lead to several reconfinement of the wave function in the radial direction of the large dipole trap. The density achieved in these revivals stays a factor of 100 lower than the initial density. Consequently, only the first microseconds after the release may alter the expansion.

During the release, the interaction energy is converted to additional kinetic energy of the system. To estimate the maximum impact of this process, we compare both energy scales. The interaction energy of two interacting particles in the ground state of a single cigar-shaped microtrap has been described in Section 2.4.3. In this limit, the contact interaction between the two particles increases the energy in the axial direction. For infinite repulsion the system can gain at most an energy of $\hbar\omega_z$. During the release of the system, the expansion of the state occurs mainly in radial direction with a kinetic energy of $E_{\mathrm{kin}} = \hbar\omega_\perp$. As a result, in the case of infinitely strong repulsion, $E_{\mathrm{kin}} = \eta E_{\mathrm{int}}$ where η denotes the aspect ratio of the microtrap.

For two particles in the ground state of a double-well potential, the energy of the system due to interaction can at most increase by $2J$ where J is the tunnel coupling. As $J \ll \hbar\omega_z$, the effect of the interaction strength on the expansion is negligible.

Summary

In this chapter, we introduced a new imaging technique to measure a quantum state on a single-particle level, with spin and position resolution. We demonstrated single-atom imaging by collecting about 20 fluorescence photons from each atom and detecting the photons with a single-photon sensitive (EMCCD) camera. We achieved a single-atom detection fidelity of 98% and a position determination with an uncertainty of 1.4 pixels. Unlike other single-atom imaging techniques, like for instance quantum gas microscopes which require complex cooling schemes, our imaging technique works with atoms in free space. By combining this method with matter-wave focusing techniques, we can measure the momentum space

distributions of quantum systems. This is the prerequisite for the measurement of two-point correlation functions presented in Chapter 7.

Chapter 5

Few atoms in a quasi-one dimensional potential

In our experiment, we are able to deterministically prepare few-fermion quantum systems in a single potential well with full control on the atom number. For instance, we can prepare two fermions in different spin states in the ground state of the microtrap and ramp them adiabatically into a double-well potential. The fact that the two fermions form a spin singlet is crucial to make the double-well system a fundamental building block of the Fermi-Hubbard model. Therefore, we want to probe the spin wave function of the two atoms. Additionally, we can prepare spin-imbalanced systems of one impurity immersed in a number of majority particles. Using a bottom-up approach and increasing the number of majority atoms one atom at a time, we can study impurity physics in the transition from few- to many-body physics. In particular, we are interested in the question how many particles are necessary to observe the expected many-body properties.

In this chapter, we use radio-frequency transitions to study two particles in a single microtrap as well as spin-imbalanced systems with a variable number of majority particles. In the first Section, we introduce radio-frequency spectrospoy and explain what quantities we can probe with this method. Then we present our measurements on the spin wave function of systems containing two fermions. After that, we report on first experiments to study the Anderson orthogonality in one dimension by measuring the quasi-particle residue. We present data for up to three majority particles at two different interaction strengths. In the future, we aim for probing systems with a larger number of majority atoms. To guarantee the applicability of the one-dimensional description, we have to increase the aspect ratio of the trapping potential. We brievly present experimental ideas to achieve this.

5.1 Radio-frequency spectroscopy

Radio-frequency (RF) spectroscopy is an important tool in atomic and molecular physics. It uses the possibility of changing the internal spin state of an atom to a different Zeeman sublevel to perform precision measurements on external fields or study the interaction energy in a system. In the field of ultracold atoms it was used for example to measure molecular binding and pairing gap in many-body systems or probe polaronic properties of systems with impurities [Sch09, Koh12]. In few-body systems, it allowed a precise measurement of ^{6}Li Feshbach resonance [Zü13]. In [Wen13b], the increase in interaction energy of a system consisting of one impurity and a varied number of majority atoms could be determined.

In our ^{6}Li -experiment, we drive RF-transitions between the three lowest hyperfine states $|1\rangle$, $|2\rangle$ and $|3\rangle$ at frequencies around 80 MHz (see Figure A.2). To change the hyperfine state of the atom, we apply a magnetic oscillatory field . For this, we use a single-copper-loop antenna mounted outside of the vacuum chamber together with a matching circuit [Lom11]. A maximum power of 100 W applied to the copper loop can lead to Rabi couplings of up to $\Omega_{23} = 2\pi \times 7$kHz. One can change the hyperfine state of an atom by either applying a fixed frequency to drive Rabi-oscillations in the system or use a Landau-Zehner passage to transfer atoms from one to another hyperfine state with a high probability.

In the following, we will give a brief introduction to the method of RF-spectroscopy using the notation of [Chi05]. In the experiments presented thereafter, we only used fixed driving frequencies to change the hyperfine state of the atoms. With this, we determined the total spin wave function of prepared few-particle states. Measuring Rabi oscillations further enabled the investigation of impurity physics in a few-body system.

5.1.1 Energy spectroscopy

For a single particle, the transition frequency between different hyperfine states is described by the Breit-Rabi formula. Transitions between adjacent states in the lowest three hyperfine states require frequencies around 80 MHz for magnetic offset fields above 100 G and depend on the magnetic offset field as well as the specific transition. We denote the transition frequency of a single atom as the bare transition frequency f_{bare}.

In a sample of atoms with two different hyperfine states, the atoms are usually interacting. Driving the atoms in one internal state to a third hyperfine state leads to a shift of the bare RF-transition frequency because the RF-photon has to additionally supply the energy difference between the initial state Ψ_i and the final state Ψ_f caused by the difference in interaction strength. The transition frequency
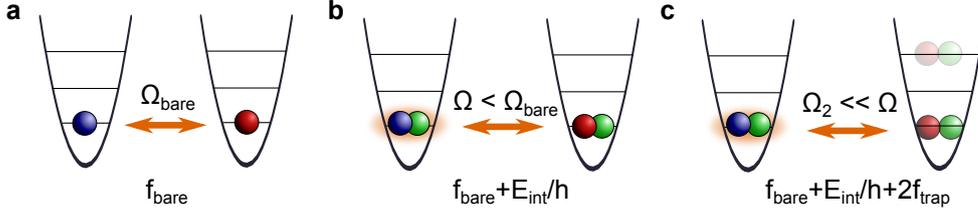
Figure 5.1: Radio-frequency spectroscopy and Rabi transitions. a)
We change the hyperfine spin state of one atom by applying an oscillatory
magnetic field to the system. For only one atom present in the system, the
transition frequency corresponds to the energy difference of the different
hyperfine states, and depending on the power, we can drive Rabi oscillations
with a frequency of Ω_{bare}. **b)** In the presence of another atom, the transition
frequency is shifted by the difference in interaction energy between the two
systems and the Rabi oscillation Ω decreases. c) By increasing the transition
frequency by multiple trap frequencies, one can drive the system into an
excited state. As the overlap into this state is much smaller, also the Rabi
oscillation Ω_2 is much lower. Figure adapted from [Wen13a].

can be calculated by

$$f_{\text{RF}} = f_{\text{bare}} + \Delta E_{\text{int},fi}/h + (\Delta E_{\text{kin,fi}}) \tag{5.1}$$

where $\Delta E_{\text{int},fi}$ describes the difference in interaction energy between the initial
and the final state. The last term accounts for an additional change of the kinetic
energy for example by transferring the system into a higher trap level. In the
following, this term will not be relevant.

5.1.2 Rabi oscillations

The transition between the initial state Ψ_i with a final state Ψ_f is well-described
by a two-level system. We describe it using the operator $\hat{M}_{\text{RF}} = \hbar\hat{\Omega}/2$ with the
corresponding Rabi frequency Ω. Using Fermi's golden rule [Chi05], one obtains a
transition rate of

$$\Gamma_{fi} = \frac{2\pi}{\hbar} \left| \langle \Psi_f | \hat{M}_{\text{RF}} | \Psi_i \rangle \right|^2. \tag{5.2}$$

The states Ψ consist of a spatial state described by the spatial wave function ϕ and
an internal state being the hyperfine state $|\text{hf}\rangle$. As the energy of the RF-photon is
on the order of 80 MHz, one can neglect the momentum change of atom when it
absorbes a RF-photon. Consequently, the spatial wave function ϕ is not influenced
by the RF-transition and one can rewrite the Rabi frequency

$$\Omega_{fi} \propto \langle \Psi_f | M_{\text{RF}} | \Psi_i \rangle = \langle \text{hf}_f | M_{\text{RF}} | \text{hf}_i \rangle \, \langle \phi_f | \phi_i \rangle. \tag{5.3}$$

The Rabi frequency of the transition is influenced by two terms. It depends on the coupling between the initial and the final hyperfine state and it is influenced by the overlap between the two spatial wave functions. If the transition is driven in a non-interacting system, $\Delta E_{\text{int},fi} = 0$ and the spatial wave functions of initial and final state are identical. Consequently, the spatial overlap is one and the Rabi frequency only depends on the coupling strength between the two hyperfine states.

5.2 Determination of the total spin wave function

In the following, we will use resonant Rabi oscillations to study the total spin wave function of a few-fermion system. For this, we use systems with few atoms in two hyperfine states $|1\rangle$ and $|2\rangle$ and select a regime, where interparticle interaction is negligible. Then we drive transitions between state $|1\rangle$ and $|2\rangle$ for various times and measuring the probability to find zero, one or two particles in the spin state $|2\rangle$.

We start with a single particle in state $|2\rangle$ prepared in the ground state of a single well. By applying a resonant RF-coupling field we initiate coherent oscillations between the hyperfine states $|2\rangle$ and $|1\rangle$. After a quarter of the oscillation period, the system is in a superposition of state $|2\rangle$ and state $|1\rangle$. The exact states after a $\pi/2$-pulse are given by

$$|2\rangle \xrightarrow{\pi/2} \frac{1}{\sqrt{2}}(|2\rangle + |1\rangle) \tag{5.4}$$

$$|1\rangle \xrightarrow{\pi/2} \frac{1}{\sqrt{2}}(|1\rangle - |2\rangle) \tag{5.5}$$

and consequently the probability to detect one atom in state $|2\rangle$ after a $\pi/2$-pulse is $\mathcal{P}_{1,|2\rangle} = 0.5$.

In that way, we observe coherent Rabi oscillations of a single atom, shown in Figure 5.3. We drive the transition between state $|2\rangle$ and state $|1\rangle$ with a Rabi frequency of $\approx 1.6\,\text{kHz}$. We probe the system after the applied RF-pulse by removing all atoms that are not in hyperfine state $|2\rangle$ with a spin-selective spilling procedure[1] . After that, we count the remaining atoms in the MOT. We repeat the measurement for several different pulse duration, and extract the probability to find zero $\mathcal{P}_0$, one $\mathcal{P}_1$ or two atoms $\mathcal{P}_2$ in hyperfine state $|2\rangle$. As a function of the

---

[1]To do this, we apply a magnetic offset field of $30\,\text{G}$ to the atoms. At this magnetic offset field, atoms in state $|2\rangle$ have no magnetic moment and consequently only atoms in hyperfine states $|1\rangle$ and $|3\rangle$ experience tilting the potential of the spilling.
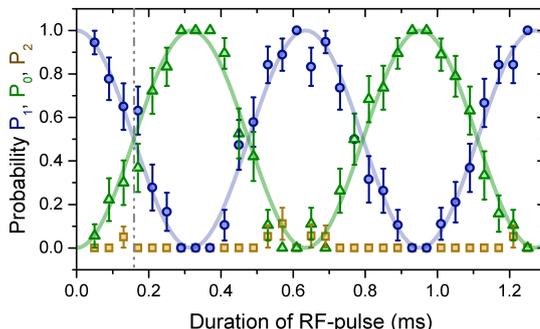
Figure 5.2: Rabi-oscillations for one fermion. We initialize one fermion in state $|2\rangle$ and drive resonant Rabi-oscillations between the two hyperfine spin states $|2\rangle$ and $|1\rangle$. After a variable duration of the RF-pulse, we measure the probability to detect one (blue), zero (green) or two (yellow) atoms in hyperfine state $|2\rangle$. The solid lines are guides to the eye not taking a finite preparation fidelity into account.

pulse duration, we observe that the probabilities $\mathcal{P}_0$ and $\mathcal{P}_1$ oscillates sinusoidally, where the oscillation amplitude is limited by our preparation fidelity of about 97%.

In the next step, we want to determine the total spin wave function of two particles. We prepare two fermions with different internal states $|1\rangle$ and $|2\rangle$ in the ground state of the microtrap and repeat the measurement. Again, we extract the probability $\mathcal{P}_0$, $\mathcal{P}_1$ and $\mathcal{P}_2$ to detect zero, one or two particle in state $|2\rangle$.

As shown in Figure 5.3 a, we do not observe oscillations in the population for two atoms prepared in the ground state of the microtrap. A naive ansatz for the spin wave function of $|1\rangle |2\rangle$ does not explain this observation as after a $\pi/2$-pulse the spin wave function would be

$$|1\rangle_1 |2\rangle_2 \xrightarrow{\pi/2} \frac{1}{2}(|1\rangle + |2\rangle)_1(|2\rangle - |1\rangle)_2 \tag{5.6}$$

$$= \frac{1}{2}(|1\rangle_1 |2\rangle_2 - |2\rangle_1 |2\rangle_2 - |1\rangle_1 |1\rangle_2 + |2\rangle_1 |2\rangle_2) \tag{5.7}$$

and consequently, one expects to observe probabilities of $\mathcal{P}_0 = 0.25$, $\mathcal{P}_1 = 0.5$ and $\mathcal{P}_2 = 0.25$.

In order to explain the observed data, we have to account for the anti-symmetry of the fermionic wave function and therefore assume a singlet spin wave function. Calculating the influence of a $\pi/2$-pulse shows no change in the probabilities

$$\frac{1}{\sqrt{2}}\left(|1\rangle_1 |2\rangle_2 - |2\rangle_1 |1\rangle_2\right) \xrightarrow{\pi/2} \frac{1}{\sqrt{2}}\left(|1\rangle_1 |2\rangle_2 - |2\rangle_1 |1\rangle_2\right) \tag{5.8}$$

79
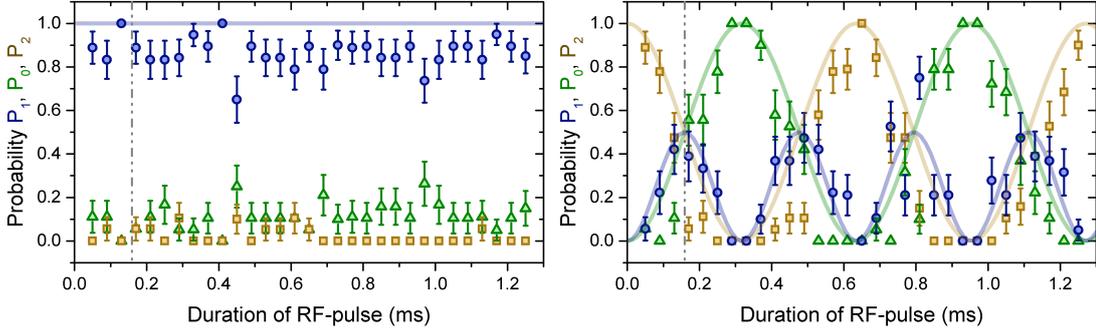
Figure 5.3: Rabi-oscillations for two fermions in a single well. a)
Evolution of the spin wave function of a prepared singlet. We prepare two
fermions in hyperfine states $|1\rangle$ and $|2\rangle$ in the ground state of the microtrap.
Then, we drive Rabi oscillations between the two states for various pulse
durations. To probe the system, we measure the probability to detect one
(blue), zero (green) or two (yellow) atoms in hyperfine state $|2\rangle$. We do not
observe oscillations, which is in agreement with a prepared spin singlet state.
The vertical dashed line indicates the time corresponding to a $\pi/2$-rotation.
b) Spin evolution of two identical fermions. We prepare two identical fermions
in hyperfine state $|2\rangle$ in the overall ground state of the system. After an
RF-pulse we observe oscillations in the probability to detect one (blue), zero
(green) or two (yellow) atoms in hyperfine state $|2\rangle$. This is consistent with
the expectations from a spin triplet $|S = 1, m_S = \pm 1\rangle$

Calculating the time evolution of the singlet state for a full Rabi oscillation shows
no oscillation as a function of a RF-pulse of various length. Our measurement
agrees with this expectation and shows, that the two-particle state prepared in
the ground state of the single potential well, has a spin spinglet wave function.

For comparison, we also prepare two identical fermions occupying the single-
particle ground state and the first excited state of the microtrap. After applying
an RF-pulse for various different durations, we detect oscillating probabilities to
find zero, one or two atoms in state $|2\rangle$. This is in agreement with the expectations
from a triplet spin wave function $|\uparrow\uparrow\rangle$.

These simple measurements demonstrate in a clear way, that two fermions which
we prepare in the ground state of a single microtrap form a spin singlet state.
This measurement can also be applied to larger systems. In [Maz16], it was for
example used to demonstrate the $SU(2)$-symmetry of the of a prepared long-range
antiferromagnetic state. The finding of a total spin of $S = 0$ encourages us to use
this system as a fundamental building block to generate small anti-ferromagnetic
states that are expected to have $S = 0$. Additionally, this technique can also help

to detect deviations from $S = 0$ for prepared systems.

5.3 Emergence of the Anderson orthogonality

Studying Rabi oscillations in a system does not only give insight on the spin wave function but also allows to observe properties of the spatial wave function of the system. In particular, it delivers information of the wave function overlap between the two systems coupled with the RF-signal. Therefore, it is well suited for studying the Anderson orthogonality catastrophe, which can be observed in strongly-interacting impurity systems.

In this section, we investigate the orthogonality catastrophe which predicts the decrease of the wave function overlap between a system of many identical fermions and one impurity and the wave function of the system without the impurity. In our experiment we perform a bottom-up approach and study systems with one impurity and a variable number of majority atoms that gradually form a Fermi sea. In particular, we drive Rabi oscillations and measure their frequencies with high precision. In this way, we can quantify the influence of the number of majority atoms and the interaction strength on the few-body wave function.

5.3.1 The orthogonality catastrophe

In a seminal paper [And67], P. W. Anderson studied the quantum states of a system with N fermions confined in a spherical box in the presence of a finite-range scattering potential. He could prove that the perturbation due to this hard-core potential causes the ground state of the system to be orthogonal to the ground state of the unperturbed system if $N \to \infty$. This observation is known as the *orthogonality catastrophe* and occurs already when the Fermi sea experience only an infinitesimally small interaction with an impurity that is fixed in space. This demonstrates the large the impact of one impurity on a quantum many-body system and offers the possibilities to turn this fact into a possibility of control [Goo11].

A widely used quantity in impurity problems it the so-called *quasi-particle residue Z*. It quantifies the overlap between the wave function of the Fermi sea and the wave function of the perturbed system

$$Z = |\langle \Psi_{FS} | \Psi \rangle|^2. \tag{5.9}$$

This quantity has been used to study the properties of Fermi polarons [Sch09] and its coherence and stabililty [Koh12]. Anderson found that for a Fermi sea containing infinitely many particles, $Z \to 0$ if the impurity is static. It is thus

natural to ask, how fast this transition occurs and how the quasi-particle residue Z depends on the interaction strength between the fermions and the impurity.

Anderson showed the orthogonality catastrophe in a three-dimensional system with a static impurity. Interestingly, the orthogonality catastrophe also occurs in a one-dimensional harmonically trapped system with a mobile impurity which has the same mass than the surrounding majority particles. Especially from an experimental point of view, harmonically trapped one-dimensional systems are interesting. However, in contrast to the homogeneous one-dimensional system [McG65], there exists no analytic solution for many particles [Gua13]. For two interacting atoms an analytic solution was found [Bus98], but apart from this only numerical solutions are available that can describe systems of up to $N \approx 10$ particles. In the regime of strong interaction (Tonks-Giradeau limit) one can however write down an ansatz for the wave function that reproduces the numerical calculations and is not limited small particle numbers [Lev14]. Experiments are in a perfect position to benchmark the theoretical predictions beyond the capability of numerical simulations.

A sensitive probe of the results from theory is to compare not only the calculated energies with measurements, but also experimentally study the wave functions. Based on their ansatz, Levinsen et al. predicted [Lev14] the decrease of the quasi-particle residue Z as a function of the number of majority particles N interacting infinitely strong with a single impurity. Figure 5.4 shows their result for infinite interaction strength of one impurity with N majority atoms. ψ_{NI} denotes the non-interacting wave function and ψ_N describes the wave function obtained from their ansatz. For $N = 1$, they recover the analytic solution of $Z = 2/\pi$. Furthermore, their theory suggests a scaling of Z proportional to $1/\sqrt{N+1}$.

More importantly, the Anderson orthogonality catastrophe represents a true many-body phenomenon driven by correlations in the system. As a consequence, one expects to detect entanglement in such systems [Oss14, Cam14]. In this context also the investigation of the system's dynamics after a quench can give crucial insight into the problem [Cam14].

Measuring Z in our system

In our setup, we want to study the emergence of the orthogonality catastrophe in a one-dimensional system as a function of the number of majority atoms. We use the deterministic preparation scheme to prepare spin-imbalanced few-fermion systems in a single microtrap [Ser11b]. Similar to the configurations in [Wen13b], we prepare one impurity in the ground state of the microtrap and different numbers of majority atoms that fill up the trap and form a Fermi sea.

In the experiments, presented here, our trap had an aspect ratio of $\eta \approx 7$.
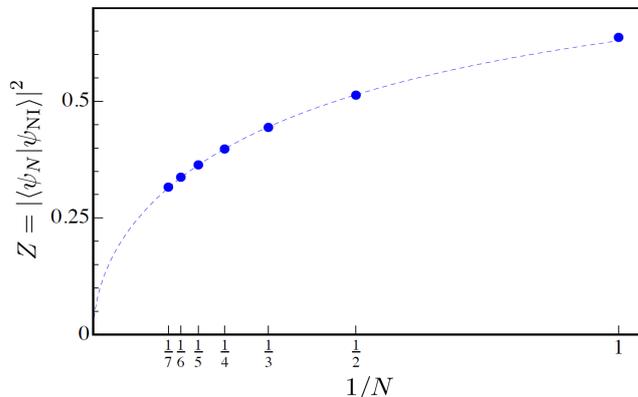
Figure 5.4: Quasi-particle residue calculated with a strong-coupling ansatz. The wave function from the strong-coupling ansatz ψ_N is compared with the wave function of the non-interacting system ψ_{NI}. The quasi-particle residue Z is plotted as a function of the number of majority atoms N. The ansatz recovers the analytic result of $Z = 2/\pi$ for $N = 1$ and predicts a decrease of Z proportional to $1/\sqrt{N+1}$ (dashed line). Figure taken from [Lev14].

In a situation where all relevant energy scales of the system are lower than the radial energy $\hbar\omega_\perp$, the system can be considered as one-dimensional. This can be guaranteed by restricting the Fermi energy $E_F = N\hbar\omega_z$ to be much smaller than $\hbar\omega_\perp$.

To measure the quasi-particle residue, we prepare a non-interacting system and then drive the impurity atom into a third hyperfine state. In that configuration, the majority atoms interact with the impurity which influences the spatial wave function. By driving resonant Rabi oscillations we can measure the spatial overlap and infer the quasi-particle residue. We will perform this measurement for different numbers of majority particles N and different interaction strenghts g_{1D}.

5.3.2 Determining the interaction energy

Before we can measure the frequency of the Rabi oscillations of the impurity, we have to determine the resonant frequency of the RF-transition. For the single impurity, the resonance frequency is given by the bare transition frequency f_{bare}, which only depends of the magnetic field. Adding, one or more majority atoms shifts the transition frequency, as we already explained in Section 5.1.1. We measure the interaction shifts with high resolution by driving the transition at low RF-power.
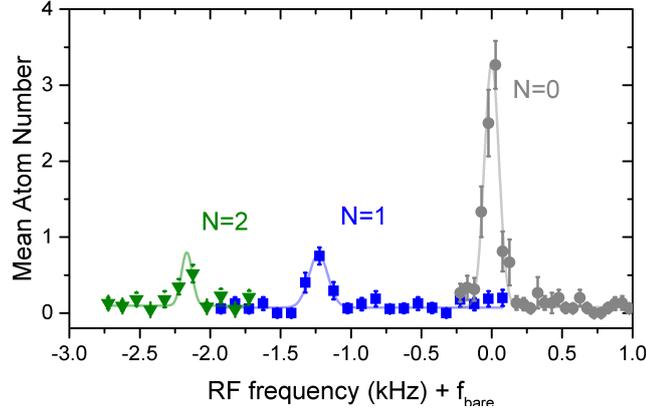
Figure 5.5: RF-spectroscopy with one impurity surrounded by N majority atoms. We drive an impurity from state $|1\rangle$ to state $|2\rangle$ by a RF-pulse and measure the mean number of atoms in state $|2\rangle$. We find the resonant transition frequency for $N = 1$ and $N = 2$ majority atoms in the system shifted by $1.23\,\mathrm{kHz}$ and $2.21\,\mathrm{kHz}$, respectively, due to the difference in interaction energy between the inital and the final state.

Figure 5.5 shows a measurement of the transition frequency for different numbers of majority particles. To find the bare transition between hyperfine states $|1\rangle$ and $|2\rangle$, we prepared about four atoms in state $|1\rangle$ and applied a RF-pulse for $100\,\mathrm{ms}$ to the atom. Then we measured the population in state $|2\rangle$ as a function of the RF-frequency. To measure the shift due to the interaction energy, we added one or two atoms in state $|3\rangle$ to the impurity in state $|1\rangle$. The presence of the majority atoms resulted in interaction shifts of on the order of a few kHz for a magnetic offset field of $634.8\,\mathrm{G}$ and an axial trap frequency of $2.5\,\mathrm{kHz}$.

We calculate the expected one-dimensional interaction strength $g_{1\mathrm{D}}$ using equation 2.43 in units of $\hbar\omega_a x a_a x$ where $a_a x = \sqrt{\hbar/(\omega_a x\, m_r)}$. Figure 5.6 shows a plot of $g_{1\mathrm{D}}$ as a function of the magnetic offset field for all three combinations of spin states. From this, we see that at a magnetic field of $634.8\,\mathrm{G}$, the initial and the final state are both interacting. To measure the quasi-particle residue, however, we want to drive Rabi oscillations between a non-interacting and an interacting system. For this reason, we additionally measure the Rabi frequency also at a magnetic offset field of $589.8\,\mathrm{G}$.

5.3.3 Measuring the quasi-particle residue

After having determined the resonance shift due to the interaction energy $\Delta E_{\mathrm{int,fi}}$, we can measure the frequency of the Rabi transition $\Omega_{\mathrm{f\,i}}$ between two states with
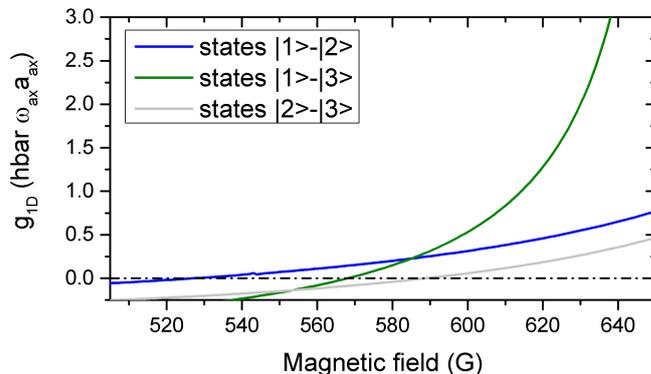
Figure 5.6: The one-dimensional interaction strength for two particles. We use equation 2.43 and the scattering lengths in three dimension to calculate the one-dimensional interaction strength g_{1D} for all three spin state combinations.

different interaction strengths and deduce the quasi-particle residue Z. To do this, we will compare the Rabi frequencies of different system configuration. Therefore it is crucial to understand all the parameters that have an impact on Ω_{fi}.

The Rabi frequency Ω_{fi} is set by several properties. As the transition can be described by a two-level system, the frequency of the Rabi oscillation changes with a detuning Δ of the driving frequency from the resonance. The effective frequency is described by $\Omega_{fi} = \sqrt{\Omega^2 + \Delta^2}$. For a precise measurement it is important to keep Δ as small as possible. The resonant Rabi frequency Ω depends on the coupling between the hyperfine states of the two systems $\langle hf_f | \hat{M}_{RF} | hf_i \rangle$. In particular, it is set by the coupling between the hyperfine states of the impurity as the majority particles are only spectators. The strength of this coupling is not expected to change significantly within a frequency change on the order of a few kHz. Additionally, the Rabi frequency Ω can be increased by increasing the power of the RF-field driving the transition. And most importantly, Ω depends on the overlap of the two spatial wave function $\langle \phi_f | \phi_i \rangle$, which is the quantity we are actually interested in.

In order to perform a precise measurement of the quasi-particle residue by comparing Rabi frequencies $\Omega(P_{RF}, \Delta, Z)$, we have to take care that the measurements we want to compare were taken under the same conditions, which is the same the RF-power P_{RF} and detuning Δ. This is especially challenging as the few-fermion systems themselves have different resonance frequencies.

Figure 5.7 shows a measurement of the Rabi frequency of the bare impurity (gray) and the Rabi oscillations of the impurity in the presence of a majority atoms (blue). We observed a significant change in the Rabi frequency due to
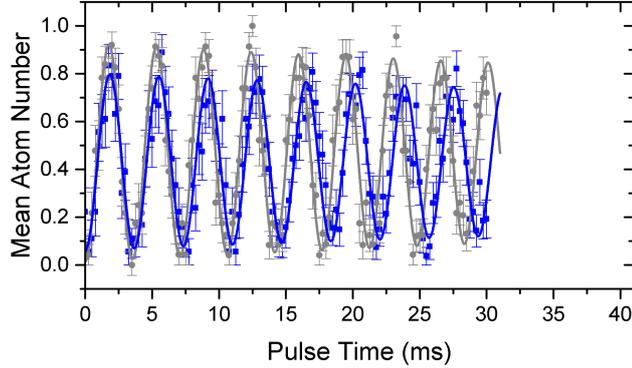
Figure 5.7: Driving Rabi oscillations in systems with different particle numbers. We measure the Rabi oscillation of a bare impurity atom by driving it between the hyperfine states $|1\rangle$ and $|2\rangle$ (gray data points). We compare it with the Rabi oscillations of the impurity in the presence of one majority atom in state $|3\rangle$ (blue) and observe a clear decrease in the Rabi oscillation. This reduction is caused by a reduced overlap of the spatial wave function between the two quantum states $\Psi_{|1\rangle|3\rangle}$ and $\Psi_{|2\rangle|3\rangle}$. The measurement of the Rabi oscillation therefore allows to extract the wavefunction overlap and infer the quasi-particle residue $Z = |\langle\phi_i|\phi_f\rangle|^2$.

the interaction energy that changes the spatial overlap of the initial and final wave function. For this measurement, we chose a magnetic field of $634.8\,\mathrm{G}$. As we already pointed out, we do not expect to obtain the quasi-particle residue in that measurement. To measure the overlap between a non-interacting and an interacting wave function, we perform measurements at $589.8\,\mathrm{G}$. As the interaction in the final state is very weak, the change in the Rabi oscillation will be very small. This requires a frequency measurement with a precision in the range of a few percent.

To perform such a high precision measurement, all additional effects on the Rabi frequency have to be much smaller than the desired level of precision. For instance, it is crucial that the power of the RF-frequency does not change as a function of the frequency. Our RF-frequency source is an RF-Signal generator (E4432B, Agilent Technologies) with programable power. The signal is then amplified by an amplifier (ZHL-100W-52, Minicircuits). Over a range of 5 kHz the amplified power changes by less then 10^{-4} with results in a change in the Rabi frequency of less than 5×10^{-5}. The frequency response of the RF-signal line is therefore not limiting the precision.

The detuning to the resonance frequency can have a large influence on the Rabi frequency. To achieve a precision on the order of 10^{-3}, the detuning has to be
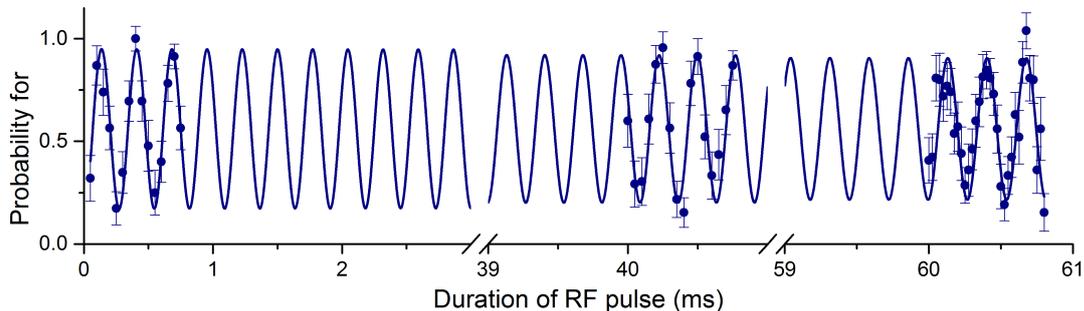
Figure 5.8: Rabi oscillations for weak interaction. We drive one impurity in the presence of two majority atoms at weak interaction. Observing the Rabi oscillation over more than 200 cycles, we can determine the oscillation frequency with a precision of 0.25%. We also do not observe a reduction in contrast over 200 cycles.

thousand times smaller than the Rabi frequency. As the precision of the detuning is not only limited by measurement but also by the magnetic field stability of the system, it is advantageous to chose a large Rabi frequency. In addition, we have to measure several 10 cycles in order to determine the frequency precisely.

Figure 5.8 shows a Rabi oscillation of more than 200 cycles at weak interactions. For this measurement, we prepared one impurity in the ground state of the single well and two majority particles and probe them at a magnetic field of 589.8 G. We drive the system at a Rabi frequency of almost 4 kHz for a duration of 60 ms. This allows a frequency determination with an uncertainty of less than 4×10^{-3}. To reduce the measurement time, we only measure the oscillation in intervals of about 20 ms for two to three cycles and fit a sinusoidal function to extract the precise frequency. Interestingly, we do not observe a reduction of the coherence in the driving of the Rabi oscillation.

We extract the overlap of the spatial wave functions between non-interacting and interacting state by deviding the measured Rabi frequency for the few-body system Ω_N by the Rabi frequency of the impurity $\Omega_{N=0}$. Figure 5.9 shows the result for different numbers of majority atoms. Our measurement precision is on the order of 10^{-3}. It allows us to observe a decrease of the frequency by 0.25% if one majority atom is present. Adding more majority atoms increases the frequency again.

When we increase the number of majority atoms, the density in the system increases too. This influences the interaction strength in the system. In order to compare systems with different densities, one uses a dimensionless interaction parameter γ. However, in a one-dimensional system, in contrast to a three-
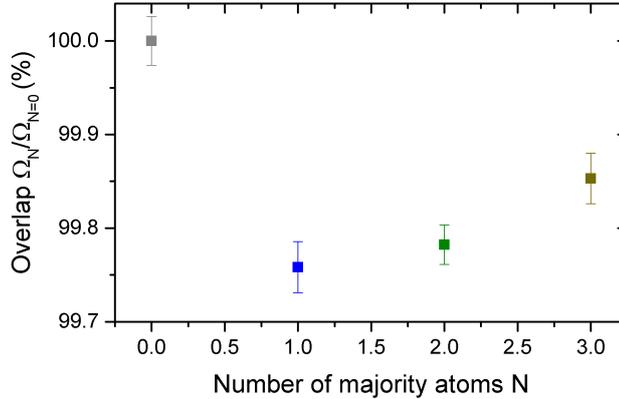
Figure 5.9: Wave function overlap extracted from the Rabi frequency. To compare the wave function overlaps for different numbers of majority atoms N, the measured Rabi frequencies Ω_N are normalized with the bare Rabi frequency $\Omega_{N=0}$. After a decrease in overlap for $N = 1$, the values increase again due to different densities in the systems.

dimensional system, the interaction strength decreases with increasing density like $\gamma_{1D} \propto \frac{g_{1D}}{k_F}$. In a harmonic system, the Fermi energy scales like $E_F = N\hbar\omega_z$ and so, the Fermi wave vector is proportional to $\sqrt{N}$. This leads to a dimensionless interaction parameter[2] of [Wen13b, Bro13]

$$\gamma = \frac{\pi}{\sqrt{2}} \frac{g_{1D}}{\sqrt{N}}. \tag{5.10}$$

This parameter is known as Lieb-Lininger parameter and allows us to compare the experimental results to a homogeneous system. It also shows that with increasing number of majority particles the interaction decreases, and the increasing overlap for $N > 1$ is not unexpected.

We want to compare the measurement with the theoretical expectation. However, we did not measure the quasi-particle residue at infinitely strong interaction and can therefore not compare the data with the predictions of the strong-coupling ansatz. However, for two atoms, the full solution of the wave function is available [Bus98]. And for more majority particles, one can use a numerical solution.

In order to display the data in the weakly and strongly interacting regime where $g_{1D} \to \infty$, we plot the inverse interaction parameter $1/\gamma$. In that way, the strong coupling limit is at $1/\gamma = 0$, whereas $1/\gamma \to \infty$ describes the non-interacting

---

[2]Note that for this definition g_{1D} is not used in the units of the reduced mass and therefore the values of are larger by $\sqrt{2}$.
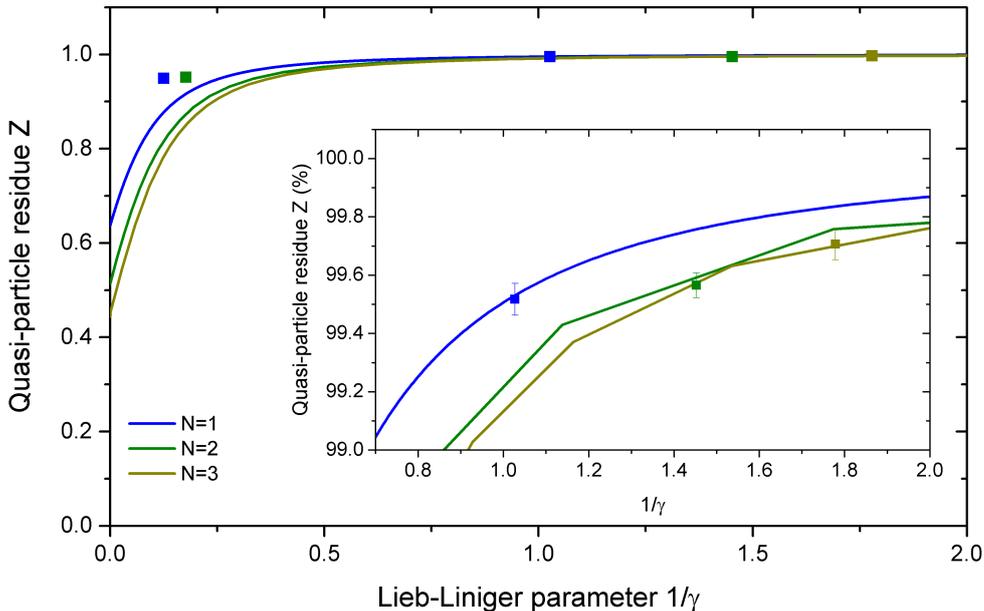
Figure 5.10: The measured quasi-particle residue. To compare our results with theory, we plot the measured quasi-particle residue as a function of the dimensionless interaction strength $1/\gamma$. The blue solid line shows the analytic solution for two particles in a harmonic confinement. The green and yellow lines are numerical solutions [Mas15]. At $1/\gamma = 0$, the solutions match with the calculations from [Lev14]. Our results are in good agreement with the theoretical prediction (see inset) if we drive the system from a non-interacting to an interacting state. They overestimate Z for the case of an initial interacting state.

regime. Figure 5.10 shows the measured quasi-particle residue $Z = |\langle \psi_N | \psi_{NI} \rangle|^2$ as a function of the dimensionless interaction strength. The blue solid line is the analytic solution from [Bus98] and the green and yellow lines are numerical solutions from [Mas15].

The data for the weakly interaction are in good agreement with the theory. The measurements at stronger interaction show a significant deviation from the expected values for the quasi-particle residue. This deviation is expected as the data was taken at a magnetic field of $B = 634.8$G where the initial state was also repulsively interacting. Therefore, in this situation, one expects a spatial overlap that is higher than the calculated quasi-particle residue.

As for ^{6}Li all three combinations of hyperfine states exhibit broad Feshbach resonances, there are only three magnetic offset fields where the initial state can be non-interacting (see also Figure 5.6). This makes a measurement of the

quasi-particle residue difficult. One possibility to obtain a relatively precise value for the quasi-particle residue, is to chose a magnetic field, where the final state is strongly interacting and the initial state is interacting much less. Due to the large difference in interaction strength, the relative deviation from the true Rabi oscillation between a non-interacting and a strongly interacting system may becomes smaller. A second possibility would be to numerically calculate the overlap between two interacting systems.

A third possibility to measure the quasi-particle residue, is to combine measurements

$$\langle \psi_N | \psi_{NI} \rangle = \langle \psi_N | \sum_i (|\psi_i\rangle \langle \psi_i|) |\psi_{NI}\rangle = \sum_i \langle \psi_N | \psi_i \rangle \langle \psi_i | \psi_{NI} \rangle \tag{5.11}$$

where ψ describes an arbitrary orthogonal basis, e.g. the one of an interacting system and i indexes the basis states where $i = 0$ denotes the ground state and $i > 0$ the excited states in the system. By measuring all overlaps between the non-interacting and the intermediate state $\langle \psi_N | \psi_i \rangle$ as well as between the intermediate and the strongly interacting state $\langle \psi_i | \psi_{NI} \rangle$, one can reconstruct the quasi-particle residue.

5.3.4 Increasing the aspect ratio of the potential

In the presented measurements, we only measured systems up to three majority particles. In order to increase the number of majority particles further, we have to ensure that the transversal degrees of freedom in the system are still not playing a role. For this, we have to increase the aspect ratio of our microtrap. E.g. to measure systems containing $N = 10$ particles, the aspect ratio has to be well above $\eta = 10$.

One possibility to increase the aspect ratio of the microtrap is to decrease the waist of the Gaussian beam, which is focused by the objective. This would result in a larger waist w_0 of the focus and the Rayleigh length, which describes the length in the axial direction, would grow proportional to w_0^2. To reach an aspect ratio of $\eta \approx 20$, the focus waist has to be about $w_0 \approx 4.5 \mu m$. Decreasing the waist of the Gaussian beam however requires a major change in the optical setup and the preparation of few-fermion systems will probabily not work at all in such a large microtrap [Ser11a].

Another possibility to increase the aspect ratio is to decrease the size of the focused Gaussian beam using an aperture. This non-invasive method has the additional advantage, that it might be possible, to perform this decrease in a dynamic way in order to not harm the preparation. In [Deh16], we investigated the influence of such a beam truncation on the intensity distribution of the mictrotrap

beam. It turns out that the most favorable position of the truncating aperture is at the position of the focusing lens, as it leads to a symmetric truncation of the axial intensity distribution. If the aperture is positioned before the lens, the intensity distribution along the propagation direction becomes assymetric. This assymetry increases with increasing distance.

Summary and Outlook

We reported on the measurement of the quasi-particle residue in a one-dimensional few-fermion system. Our preliminary results are in agreement with the expectations from the Anderson orthogonality catastrophe. As a next step, we plan to increase the aspect ratio of the trapping potential to investigate one-dimensional systems with larger numbers of majority particles and observe the vanishing quasi-particle residue. The established methods may also allow us to measure other properies of the impurity system, as e. g. the effective mass and perform dynamical measurements [Cam14]. The unprecedented measurement precision also puts us into a perfect position to measure polaron-polaron interactions.

Chapter 6

Two fermions in a double well: Realizing the fundamental building block of the Hubbard model

The Hubbard model is a paradigmatic model to describe interacting particles that move in a periodic potential. The motion of the particles is described by nearest-neighbor hopping and the particles only interact when they occupy the same site. Despite the reduction to only two relevant parameters, the tunnel coupling J and the on-site interaction U, the Hubbard model exhibits a rich phase diagram. To gain understanding on such a complex system, it is often helpful to first look at the smallest realization that incorporates all the important physics which leads to specific phases in the large system. Having understood this fundamental building block, one can gradually increase the size of the system and watch how complex phases emerge.

We want to perform such a bottom-up approach experimentally. In this chapter, we report on the first step in this approach which is the realization of the fundamental building block of the Fermi-Hubbard model. It consists of two fermions in an isolated double-well potential.

The isolated double-well potential is created from two partly overlapping focused laser beams. By changing the power in the individual beams, we can tune the relative depth between the two well. We start by deterministically preparing two particles in the ground state of one single optical tweezer and then add the second potential well. By lowering the barrier between the two wells, the atoms can tunnel between the wells. A Feshbach resonance allows us to tune the interaction strength between the two fermions and we make use of the tunable relative depth to deterministically prepare the two particles in the ground state of the double-well potential.

The tunability of the relative depth comes at a price: One has to ensure that the tilt of the double-well potential does not change during days. We find that the system is sufficiently stable to studying tunneling dynamics in the system. In addition, it is sufficient to resolve the super-exchange energy which is responsible for the anti-ferromagnetic ordering in the Hubbard model.

Achieving this level of control on the fundamental building block is the first step in our bottom-up approach. Now, it will be possible to increase the size of the system by adding more wells or particles and deterministically prepare the quantum states of larger and more complex systems with low entropy.

This chapter reports on the realization of the fundamental building block in our setup. We start with a theoretical description of two fermions a double-well potential and explain the accessible eigenstates. Then, we explain our tunable parameters and describe how we calibrate and control the Hubbard parameters. This allows us to adiabatically prepare the two fermions in eigenstates of the double-well system at different interaction strengths. We then explain our method to measure the super exchange energy which is based on modulation spectroscopy. Last but not least, we demonstrate our ability to change the symmetry of the spin and spatial wave function by singlet-triplet oscillations.

Parts of this chapter have been published in [Mur15b]. Details can also be found in [Mur15a].

6.1 The two-site Hubbard model of two interacting fermions

Studying many-body systems in double-well potentials led to a lot of insight in the field of quantum physics. One of the first was the observation of phase coherence between two spatially separated Bose-Einstein condensates [And97]. Experiments with few particles in a double well could beautifully demonstrate effects like the two-particle interference of two bosons in a Hong-Ou Mandel type experiment [Kau14]. Furthermore, the system allows to perform fundamental operations for quantum computation [And07, Tro10, Foo11] and to observe second-order tunneling [Föl07, Tro08] showing the connection to the field of condensed-matter physics.

In our setup, we realize the fundamental building block of the Hubbard model which consists of two neutral fermionic particles trapped in a double-well potential. A system has to fulfill several approximations to be describable by the Hubbard model. First of all, the tight-binding approximation has to be applicable. As already discussed in Section 2.3.1, the particles are then describable by Wan-

nier states localized on individual wells, with the occupation probability of the neighboring site being negligible. For very deep periodic potentials, the localized wavefunction can then be approximated by the eigenstates of the individual wells.

The motion of particles from one site to another can be described by a tunnel coupling J. This energy scale depends on the overlap between wavefunctions on neighboring sites. Due to the tight-binding approximation it is much smaller than the energy to the single well excited state $J \ll \hbar\omega$. Furthermore, we restrict the model to the lowest band (single-band approximation). To fulfill this, our double-well system is only half filled and the on-site interaction U is smaller than the energy gap to the next higher band during all our experiments.

If these restrictions are fulfilled, the natural single-particle basis state of the Hubbard model consists of the ground state Wannier function for each site. For the two-site Hubbard model, we use the notation $|L\rangle$ and $|R\rangle$. In this basis, the Hamiltonian of a single particle in a double-well potential can be written as

$$h_{\mathrm{sp}} = \begin{pmatrix} +\Delta & -J \\ -J & -\Delta \end{pmatrix} \tag{6.1}$$

where J is the tunnel coupling and Δ denotes the energy difference from the symmetric configuration in case of a potential tilt. For the symmetric double well ($\Delta = 0$), the eigenstates of the system are the symmetric superposition and the anti-symmetric superposition of the particle occupying the left or the right site.

$$|+\rangle = \frac{1}{\sqrt{2}} \left(|L\rangle + |R\rangle \right) \tag{6.2}$$

$$|-\rangle = \frac{1}{\sqrt{2}} \left(|L\rangle - |R\rangle \right) \tag{6.3}$$

For two decoupled wells ($J = 0$) the resulting eigenenergies are degenerate. However, for finite coupling strength the two energies are $E_+ = -J$ and $E_- = +J$ where the symmetric superposition is lower in energiy and represents the ground state of the system. This can be easily understood as a particle in the symmetric state is more delocalized and therefore minimizes its kinetic energy.

For two particles in a double well the basis can be constructed from the single particle basis: $\{|LL\rangle, |LR\rangle, |RL\rangle, |RR\rangle\}$ where the first (second) entry denotes the state of the first (second) particle. The two-particle Hamiltonian can then be formulated as

$$H = h_{\mathrm{sp},1} \otimes \mathbb{1}_2 + \mathbb{1}_1 \otimes h_{\mathrm{sp},2} + \mathrm{Diag}\{U, 0, 0, U\} \tag{6.4}$$

We constructed it using the single-particle Hamiltonian h_{sp} and inserted a term that accounts for the on-site interaction U for all basis states that show double

|	$U \rightarrow -\infty$	$U = 0$	$U \rightarrow +\infty$
$|a\rangle$	$\frac{1}{\sqrt{2}}(|LL\rangle + |RR\rangle)$	$\frac{1}{2}(|LL\rangle + |RR\rangle) + (|LR\rangle + |RL\rangle)$	$\frac{1}{\sqrt{2}}(|LR\rangle + |RL\rangle)$
$|b\rangle$		$\frac{1}{\sqrt{2}}(|LL\rangle - |RR\rangle)$	
$|c\rangle$	$\frac{1}{\sqrt{2}}(|LR\rangle + |RL\rangle)$	$\frac{1}{2}(|LL\rangle + |RR\rangle) - (|LR\rangle + |RL\rangle)$	$\frac{1}{\sqrt{2}}(|LL\rangle + |RR\rangle)$
$|d\rangle$		$\frac{1}{\sqrt{2}}(|LR\rangle - |R L\rangle)$	
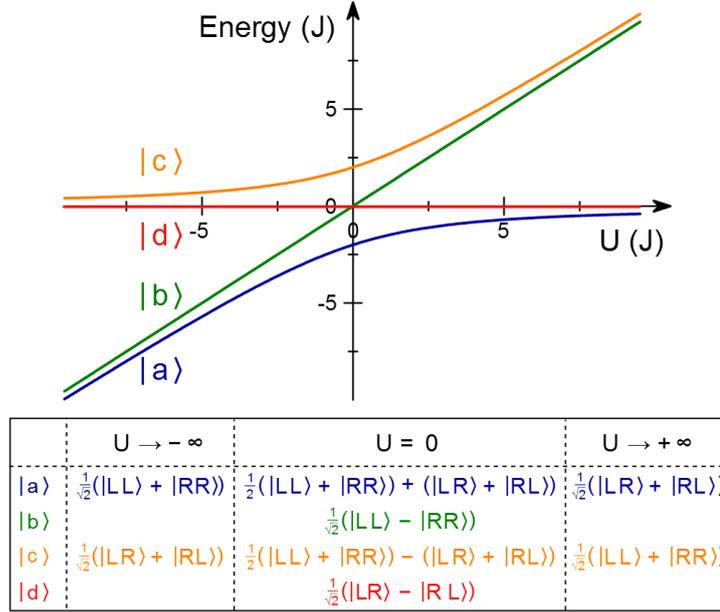
Figure 6.1: Energy spectrum of the two-site Hubbard model with two interacting particles. The eigenenergies of the four eigenstates are plotted for a symmetric double well $\Delta = 0$ as a function of the on-site interaction strength U. The table shows the eigenstates written in the spatial basis in the limiting cases of strong attractive $U \rightarrow -\infty$, zero $U = 0$ and strong repulsive interaction $U \rightarrow +\infty$.

occupancy. This results in the two-site two-particle Hamiltonian written in the basis of spatial wave functions

$$H = \begin{pmatrix} U + 2\Delta & -J & -J & 0 \\ -J & 0 & 0 & -J \\ -J & 0 & 0 & -J \\ 0 & -J & -J & U - 2\Delta \end{pmatrix} \tag{6.5}$$

Diagonalizing the Hamiltonian results in four eigenstates. As already explained in Section 2.1, three of these states are spatially symmetric under particle exchange ($|a\rangle$, $|b\rangle$ and $|c\rangle$). State $|d\rangle$ has an anti-symmetric spatial wave function. Consequently the two fermions do not interact with each other and therefore the energy of the state does not change as a function of the on-site interaction strength U. We assumed two fermions with different hyperfine spin. As a consequence of the anti-symmetric total wave function of the fermions, the spin wave function of the states $|a\rangle$, $|b\rangle$ and $|c\rangle$ is a spin singlet $|S\rangle = \frac{1}{\sqrt{2}}(|\uparrow\downarrow\rangle - |\downarrow\uparrow\rangle)$ with the total

	$\Delta \to -\infty$	$\Delta = 0$	$\Delta \to +\infty$
$|a\rangle$	$|LL\rangle$	$\frac{1}{2}(|LL\rangle + |RR\rangle + |LR\rangle + |RL\rangle)$	$|RR\rangle$
$|b\rangle$	$\frac{1}{\sqrt{2}}(|RL\rangle + |LR\rangle)$	$\frac{1}{\sqrt{2}}(|LL\rangle - |RR\rangle)$	$\frac{1}{\sqrt{2}}(|RL\rangle + |LR\rangle)$
$|c\rangle$	$|RR\rangle$	$\frac{1}{2}(|LL\rangle + |RR\rangle - |LR\rangle - |RL\rangle)$	$|LL\rangle$
$|d\rangle$	$\frac{1}{\sqrt{2}}(|LR\rangle - |RL\rangle)$	$\frac{1}{\sqrt{2}}(|LR\rangle - |RL\rangle)$	$\frac{1}{\sqrt{2}}(|LR\rangle - |RL\rangle)$
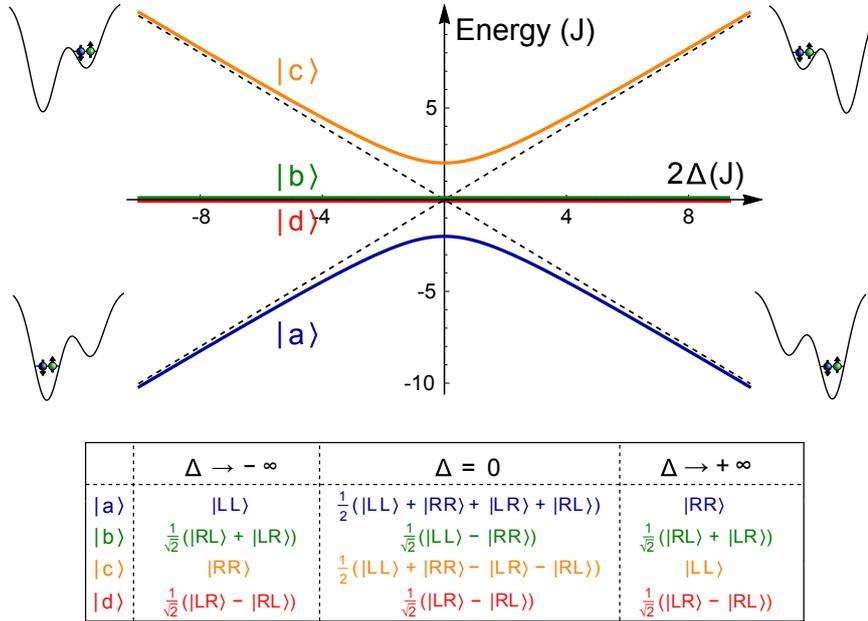
Figure 6.2: Eigenenergies of the two-site Hubbard model without interaction. We plot the eigenenergies of the tilted non-interacting Hubbard Hamiltonian. As $U = 0$, we recover the physics expected from single particles. At a large tilt, the ground state shows large occupation probability in the deeper well. For a finite tunnel coupling, the degeneracy at $\Delta = 0$ is lifted and an adiabatic passage from $\Delta \ll 0$ to $\Delta \gg 0$ is possible. The energy splitting around $\Delta = 0$ is $4J$ and corresponds to the expected width of a band in for an electron gas in one dimension.

spin $S = 0$ whereas the spatially anti-symmetric state $|d\rangle$ has a triplet spin wave function $|T\rangle = \frac{1}{\sqrt{2}}(|\uparrow\downarrow\rangle + |\downarrow\uparrow\rangle)$ with a total spin of $S = 1$.

The energy spectrum of the two-site Hubbard model and the eigenstates are depicted in Figure 6.1 for the symmetric configuration $\Delta = 0$ and in Figure 6.2 in the limit of zero on-site interaction $U = 0$ in units of the tunnel coupling J.

The *ground state* is denoted with $|a\rangle$. For $U = 0$, it simply consists of two independent particles occupying the symmetric ground state of the double well. When U is increased to the repulsive side, doubly occupied sites become more and more unfavorable. Eventually, the ground state reaches $|a\rangle_{U\to\infty} = \frac{1}{\sqrt{2}}(|LR\rangle + |RL\rangle)$ in the limit of large on-site interaction and energetically approaches the state $|d\rangle$. This energy splitting between $|a\rangle$ and $|d\rangle$ scales like $-4\,J^2/U$ for large on-site interaction and is caused by the super exchange (see Section 2.3.2). For attractive on-site interaction $U < 0$, double occupancies are favored and the state approaches

$|a\rangle_{U\to-\infty} = \frac{1}{\sqrt{2}}(|LL\rangle + |RR\rangle)$ for infinite U. The ground state has a total spin of $S = 0$ and is non-degenerate over the whole range of U. Therefore it does not cross any other energy level at finite U. Lieb has shown [Lie93, Aue98] that this is also the case for the more general situation of a bipartite lattice filled with as many atoms as sites and $N_{|\uparrow\rangle} = N_{|\downarrow\rangle} = 1/2\,N_{\text{sites}}$.

At $U = 0$, the *highest excited state* denoted with $|c\rangle$ consists of two independent fermions each occupying the anti-symmetric state $|-\rangle$. For repulsive interactions, the double occupancy is favored in contrast to the ground state. At attractive interaction, the state tends to single occupation, which is also in contrast to the behavior of the ground state. This similarity can be expressed by a particle-hole mapping between the two states[1] and explains the similarities in the energies. We will use this fact later for the measurement of the super exchange energy.

At high interaction strength $U \gg J$, the four states regroup into two doublets. If the spacing between the two doublets is much larger than the energy difference between the two states in the doublet, the system can be described in terms of the Heisenberg model [Kes10].

6.1.1 Experimental realization of the two-site Hubbard model

We realize the double-well potential by generating two optical tweezers that are partially overlapping. As explained in detail in Section 3.3.2, we create them by focusing two far-red detuned laser beams that act as optical dipole traps to the atoms. In the experiments presented in this chapter, the waist of each optical tweezer was about 1.65μm.

Our experimental setup allows to set and tune all relevant parameters at will. We can change the distance d between the two wells and thereby set the possible parameter range for the tunnel coupling J. Here, we chose a distance of 2μm between the two wells. Having individual control on each optical tweezer, we can tune the relative depth Δ between the two wells. This allows us for example to prepare fermions in the eigenstate of the double well potential. The control on the overall light power that generates the potential enables us to quickly switch and set the barrier height between the two wells. This is crucial to initialize the system in the uncoupled regime and then quench it to a well-determined tunnel coupling J. To control the on-site interaction in the system U, we tune the scattering length of the particles using a Feshbach resonance (for details see Section 2.4.2).

To fulfill the required tight-binding approximation, we choose a tunnel coupling

---

[1]In [Ho09], such a particle-hole mapping was suggested to map the repulsive onto the attractive Hubbard model.
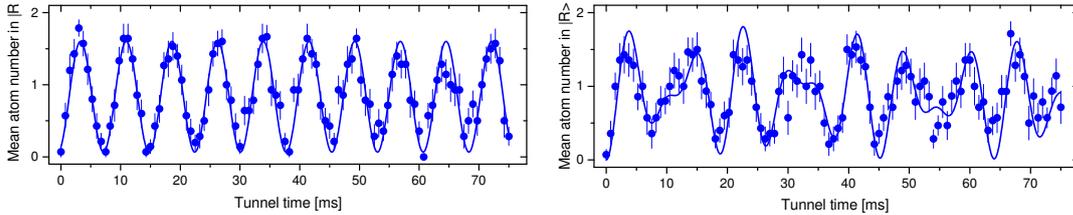
Figure 6.3: Tunnel oscillations with and without interaction. a) Oscillations without interactions. We plot the mean number of atoms in the right well after an initialization in $|LL\rangle$ and variable tunneling time. The data points show the statistical average of 15 repetitions for each tunnel time. We observe a sinusoidal oscillation (solid line) with a frequency of $2J/h = (134.6 \pm 1.0)$Hz consistent with two independently tunneling fermions. **b)** Tunneling with interaction. Due to the interaction, the two particles do not tunnel independently anymore. A Fourier transfom of the recorded oscillation reveals three different frequencies. The solid line shows a calculation of the expected time evolution for the calibrated tunnel coupling and on-site interaction.

on the order of $J/h \approx 100$Hz which is much smaller than the distance to the next higher band. The energy difference to the first excited states is on the order of 1.2 kHz. In all our experiments we did not exceed an on-site interaction of $U \approx 0.5\hbar\omega_z$. All parameters can be found in Appendix B.4.

6.2 Calibrating the Hubbard parameters

The shape of the double-well potential determines the Hubbard parameters of our system. Changing the distance between the two wells or the overall light power in the potential strongly influences the overlap between the Wannier functions $|L\rangle$ and $|R\rangle$ and changes the tunnel coupling strength J. The tunneling of one particle from one site to the other can be described in terms of a two-level system described by equation 6.1. As a consequence, tunneling is only resonant if the tilt Δ between the two wells is not larger than the tunnel coupling J.

To observe oscillations in our system, we have to know and control these parameters. In addition, the shape of the potential has to be stable during the measurement to actually observe the tunneling dynamics over several oscillations. The experimental realization turned out to be challenging. Therefore, studying the oscillations in the system did not only allow us to calibrate the Hubbard parameters, but also gave hints to the limitations in the stability of the system.

For all tunneling measurements, we initialize the system by preparing two
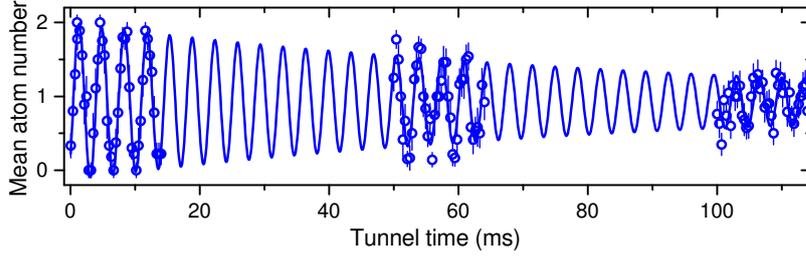
Figure 6.4: Decay of the tunneling oscillations of two non-interacting particles. We observe a decay time of about 80 ms. The amplitude does not show a pure exponential decay. Assuming a small drift of the resonance position by about 25 Hz during the measurement time leads to a dephasing of the oscillation that agrees with the observed shape.

non-interacting atoms in the ground state of a single potential well. After that, we slowly ramp on a second well next to it and keep the tunnel coupling negligible. In this way, we prepared the system in state $|LL\rangle$ which is not an eigenstate.

To start the dynamics, we suddenly switch on the tunnel coupling by decreasing the total optical power and thereby lowering the height of the barrier in the double-well potential. We do this at a time scale slow enough to not excite the atoms into higher trap levels. Then, we let the system evolve for some time before we stop the dynamics by switching off the tunnel coupling again. We measure the occupation probability of the final state by switching off one well. We then recapture the atoms in the remaining well into the MOT and count them.

6.2.1 Calibration of the tunnel coupling

For two non-interacting particles, we observe sinusoidal oscillations of the mean atom number in the right well (see Figure 6.3(a)). We measured the frequency of these oscillations for different depths of the coupled double well. Figure 6.5(a) shows the measured tunnel frequency as a function of the overall light power forming the potential. It decreases exponentially with increasing barrier height as expected from the overlap between Wannier functions in the tight-binding approximation. Based on this measurement, we chose the tunnel coupling strength around $J/h = 100$Hz. At this potential depth we fulfill the required approximations of the Hubbard model as the axial trap frequency is about ten times larger than the tunnel coupling.

We can observe tunneling oscillations for several tens of milliseconds which corresponds to more than 20 oscillations. Figure 6.5 shows such a long oscillation where the damping time is (83 ± 9)ms. From the time-dependent amplitude we
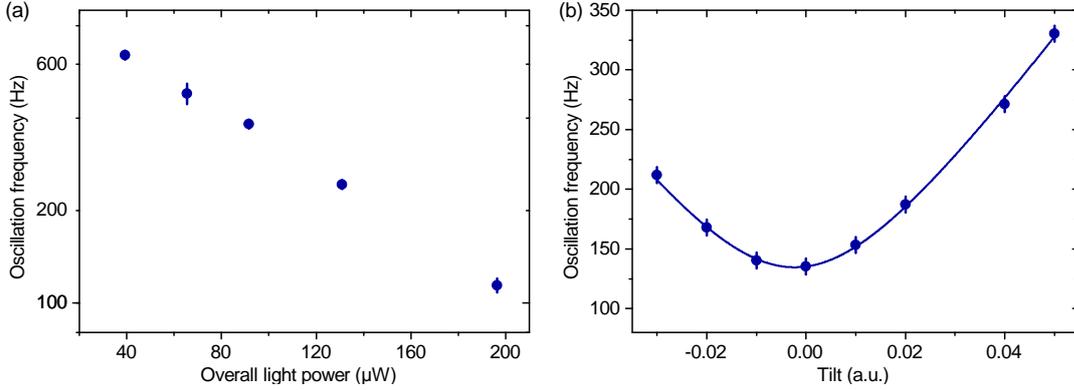
**Figure 6.5: The influence of the barrier height and the tilt on the
tunnel frequency. a)** Dependence on barrier height. We alter the effective
barrier height by changing the overall light power that creates the double-well
potential. As a function of the power we observe an exponential scaling of
the oscillation frequency. For all further measurements, we use settings of
the two lowest oscillation frequencies shown here. **b)** Influence of the tilt.
We perform tunneling sequences with different relative depth between the
two wells and measure the effective tunnel coupling $J' = \sqrt{J^2 + \Delta^2}$ expected
from a two-level system. This allows us to calibrate the tilt and find the
configuration of the symmetric double well.

could conclude that the decay is not exponential. Instead, simulating a continuous
change of the tunnel resonance due to an instability in the relative depth leads
to slightly different tunnel coupling for every realization. A linear drift of the
resonance by 25 Hz could explain the observed behavior. This shows that the
damping time of the tunnel oscillation is limited by the stability of the double-well
potential.

6.2.2 Calibration of the tilt

In order to calibrate the tilt Δ of the double-well potential, we perform the
tunneling sequence for different relative depths of the two wells. To do this, we
change the relative power in the two focused laser beams using an acousto-optic
deflector (AOD). Details on the experimental method can be found in Section
3.3.2. We measure the oscillation frequency for various different tilts around the
resonance. The result is shown in Figure 6.5 b. and described by the single-particle
Hamiltonian in equation 6.4. By assuming a detuned two-level system, we can
deduce an effective tunnel coupling of $J' = \sqrt{J^2 + \Delta^2}$. By fitting the effective
tunneling rate $2J'(\Delta)$ to the observed oscillation frequency we calibrate the tilt

axis and also extract the bare tunneling frequency. Within the range of chosen tilts, we do not observe a deviation from the two-level assumption.

6.2.3 Stability of the tilt

To observe tunnel oscillations with high contrast over several periods, the stability of the tilt Δ has to be better than the tunnel coupling $J/h \approx 100$Hz. We stabilize the overall light power in the double well with an active feedback. In contrast to this, the relative depth of the two wells is not actively stabilized. With a typical potential depth of 30 kHz, corresponding to an overall light power of $P_{\text{tot}} \approx 200\mu W$, we need a passive stability of the relative potential depth on the order of 10^{-4} to observe coherent oscillations.

When we started the tunneling experiments in the double well, we observed rather short coherence times. We then observed that the tilt at which we observed the tunneling resonance changed as a function of time after switching on the second potential well. We concluded that switching on the second potential well leads to an additional heating of the acousto-optic deflector which generates both beams. As a consequence, the diffraction efficiency in the device changes until it has reached its new equilibrium temperature. In this process the relative depth changes by more than J. This drift, however, turned out to be reproducable for each cycle of the experiment and we compensate it by applying an exponential ramp to the relative RF powers with a time constant of ≈ 400ms. In this way, our setup is only limited by long-term drifts of the relative depths which is on the order of 10Hz to 20Hz per day.

In the future, we aim for an active stabilization of the relative depths with the help of a fast camera read-out. This will allow us not only to eliminate the long-term drifts but it is also crucial for the extension of the potential beyond two wells. First steps on that project are reported in [Lak15].

6.2.4 Calibration of the on-site interaction

For two interacting particles, the dynamics cannot be described by the single-particle Hamiltonian anymore. As a consequence of the interaction, the two particles tunnel in a correlated way and the observed oscillations are not describable by a single sinusoidal function (see Figure 6.3 b). Knowing the experimental parameters of the system, we can predict the time evolution. Figure 6.3 b shows the prediction based on the parameters (solid line) which fully agrees with the measurement.

To calibrate the on-site interaction we perform conditional tunneling similar to [Tro08]. We prepare the two fermions in state $|LL\rangle$ and change the scattering
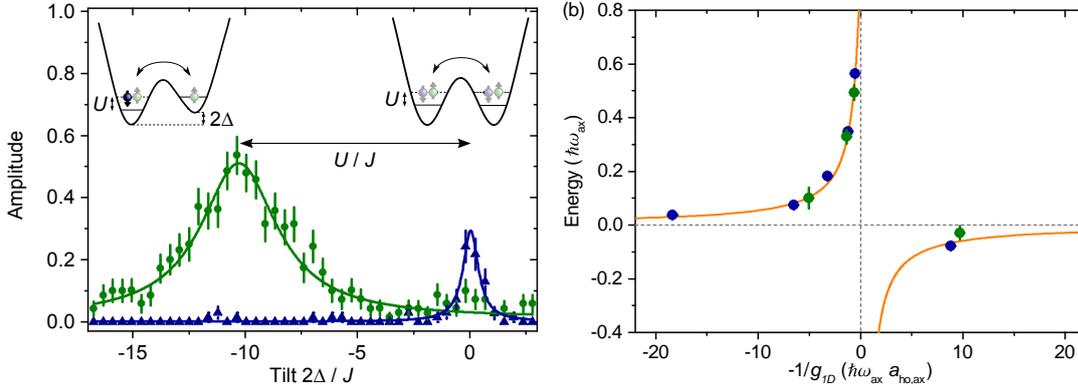
Figure 6.6: Calibrating the on-site interaction by conditional tunneling. a) We measure the on-site interaction U by comparing the position of pair and conditional single-particle tunneling. The data shows the time-averaged probability to find two particles (blue) and a single particle (green) in the second well as a function of the tilt Δ. **b)** We compare the results for different scattering lengths and tunnel couplings with a calculation in a single cigar-shaped trap and find good agreement.

length by means of a Feshbach resonance. Then, we switch on the tunnel coupling as explained above. Due to the interaction the two particles can only tunnel as a pair in case of a symmetric double-well potential. This tunneling will happen with much lower frequency compared to the single-particle tunneling and the resonance is more narrow. By tilting the potential we can compensate the on-site interaction energy. Then single-particle tunneling between the two wells can be restored, in case that the other particle stays in state $|L\rangle$. By scanning the tilt for different magnetic fields and measuring the two-particle and the conditional single-particle resonance, we can infer the on-site interaction strength $U = -2\Delta$.

An example of the conditional tunneling is shown in Figure 6.6. After scanning the tilt and averaging over different tunneling times we observe two distinct peaks that belong to pair tunneling or conditional single particle tunneling. To distinguish the two processes, we plot the probabilities to find on (green data points) or two particles (blue data points) in the right well of the potential. We fit the two peaks and extract the distance between the two resonances. Using the calibration of the tilt we can then deduce the on-site interaction energy U in units of the tunnel coupling.

We performed the calibration for two different tunnel coupling strengths $J/h = (67.3 \pm 0.5)$Hz (blue data points) and $J/h = (142.0 \pm 0.5)$Hz (green data points) and all magnetic fields, that we will use later. The results are plotted in units of the axial trap frequency. The measured values agree with a calculation (orange solid

line) of the interaction strength expected in a cigar-shaped harmonic potential of an aspect ratio of $\eta = 7$. To do this calculation, we use the theory developed in [Idz05]. A detailed explanation on the calculation can be found in Section 2.4.3.

All in all, the investigation of dynamics in the double-well potential allows us to calibrate the Hubbard parameters for further experiments. The observation of coherent oscillations over several periods also demonstates a sufficient stability of the potential. Both aspects are necessary prerequisites for the realization of the fundamental building block of the Fermi-Hubbard model.

6.3 Preparing and probing of eigenstates in a double-well potential

The interesting low-temperature phases of the Hubbard model are governed by the ground state properties of the system [Aue98]. To realize the fundamental building block of the Hubbard model, we have to be able to deterministically prepare two interacting fermions in the ground state of the system. At repulsive interaction, the ground state exhibits an increasing probability of singly occupied sites similar to a Mott-insulating state (see Figure 6.8). At attractive interaction, the double occupancy increases as expected for a charge-density wave. We successful prepare eigenstates of the system and perform further investigations of the level structure of the Hubbard model by measuring the super exchange energy. By using our novel single-atom resolved imaging technique (Chapter 4) we later demonstrate that the ground state exhibits strong correlations (see Section 7).

6.3.1 Adiabatic ramping into eigenstates

For the ground state preparation, we start our experiments with two non-interacting fermions occupying the ground state of a single microtrap. Similar to the ground state of the Hubbard model, this initial state has a total spin of $S = 0$ as demonstrated in Section 5.2 and a symmetric spatial wave function.

Then, as depicted schematically in Figure 6.7 a, we add the second potential well and introduce a large tilt. Consequently, the two atoms occupy the state $|LL\rangle$ in an uncoupled double well. We chose a tilt of $\Delta = -1/2\hbar\omega_{\mathrm{ax}}$, such that the left well is deeper than the right well. Then we turn on the tunnel coupling J. As the tilt is much larger than the tunnel coupling J, this brings us directly into the ground state of the coupled double well as the overlap of $|LL\rangle$ with the ground state of the tilted double well is almost 1. After this, we can adiabatially ramp to the relative depth of the two wells to zero.
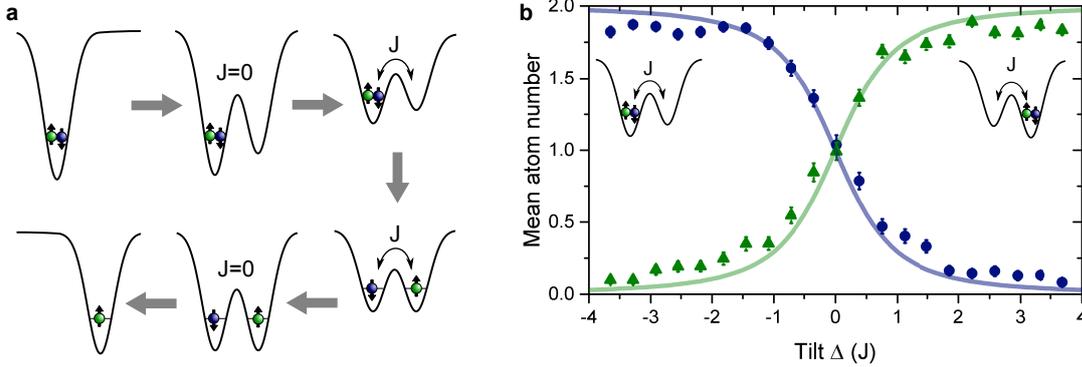
Figure 6.7: Adiabatic passage into the ground state. a Preparation of
two fermions the ground state of the double well. We start with two fermions
in the ground state of a single optical tweezer. We then add a second well
and introduce a finite tilt Δ in the double-well potential. After that, we
couple the double well while staying in the ground state of the system as
the tilt is much larger than the tunnel coupling J. We can then ramp the
tilt to zero. To probe the system, we decouple the wells and switch off one
of them. Then we count the atoms in the remaining well. **b** Adiabaticity
of the ramp accross the resonance. We start with two atoms in state $|LL\rangle$
in a coupled double well of $J/h = (142.0 \pm 0.5)$Hz. Then, we change the
relative depth with $2J/100$ms and measure the mean atom number per well
at different tilt values. For large negative (positive) tilts, we find both atoms
in the left (right) well plotted as blue (green) data points. Each point is the
mean value of about 130 measurements. Within the error bars we do not
observe a reduction in the mean atom number after the ramp into the right
well. The solid lines show the expectation from the Hubbard model.

To prove that the ramp of the tilt is adiabatic, we ramp the system across
the resonance to $\Delta = +^1\!/_2\hbar\omega_{\mathrm{ax}}$. Figure 6.7 shows a plot of the population per
well across the tunneling resonance. We compare the ground state population in
the second well after the ramp with the ground state population in the first well
before the ramp. Within the error bars, we observe no reduction in ground state
populations for ramp speeds of $2J/100\,$ms.

After the preparation of two non-interacting fermions in the ground state of
the symmetric double well, we adiabatically ramp the interaction strength to
the attractive side around $300\,$G ($a_{\mathrm{sc}} = -288\,a_0$) or to the repulsive side $740\,$G
($a_{\mathrm{sc}} = +2974\,a_0$) within $60\,$ms. To check for the adiabaticity of the field ramp,
we hold it at the respective fields for various different hold times and then ramp
the system back to $U = 0$ and $\Delta = -^1\!/_2\hbar\omega_{\mathrm{ax}}$. We compared the ground state
population with and without the full ramp. We did not observe any heating, that is
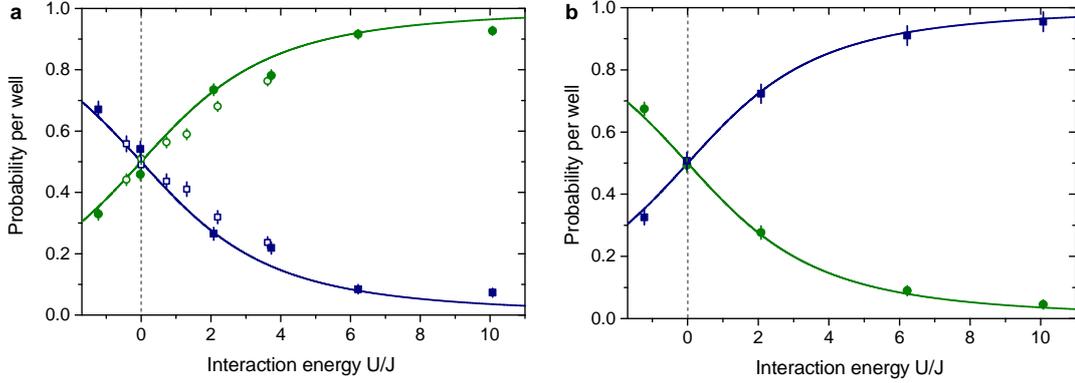
Figure 6.8: Occupation probability as a function of the interaction strength. a) Occupation statistics of the ground state $|a\rangle$. The green (blue) data points show the single (double) occupancy. Starting from equal probabilities at $U = 0$, the probability of single occupancies rises (drops) with increasing repulsion (attraction), exhibiting the two-particle analog of a Mott-insulator (charge-density wave). **b)** Occupation statistics of state $|c\rangle$. Here the double occupancy rises with increasing repulsion. Due to the finite preparation fidelity in the system, the probabilities have been corrected in both plots. The solid lines show the occupation probability calculated from the Hubbard model.

caused by the magnetic field ramps. This means that our fidelity of preparing the ground state of the double well with interaction is only limited by the preparation fidelity in the single well, which is typically above 90%.

In a similar way, we could also prepare the excited state $|c\rangle$ of the two-site Hubbard model. This can be understood by taking a look at Figure 6.1. For the ground state preparation, we started with the two atoms occupying the deeper well. To prepare the excited state $|-\rangle = 1/\sqrt{2}(|L\rangle - |R\rangle)$, both atoms occupy the well that is less deep. In an adiabatic ramp, one can then reach state $|-\rangle$ and subsequently follow it adiabatically to higher interaction strengths. As our system is well isolated from the environment and the optical potential does not heat the system significantly, we do not observe a decay into lower-lying states. Note, that for the excited state $|c\rangle$ the ramp to higher fields has to be slower to maintain adiabaticity, as a coupling into state $|b\rangle$ is not forbidden by symmetry.

6.3.2 Measuring occupation probabilities

To probe the prepared state, we measure the site-resolved occupation probability as a function of the interaction strength. We perform the measurement of the

occupation number per well, as explained above (see Figure 6.7). For the presented measurements, we repeated the experiment about $N \approx 300$ times for each data point and calculated the probabilities $n_i' = N_i/N$ to find $i = 0, 1$ or 2 atoms in one well. The measured occupation probabilities are influenced by our finite preparation and detection fidelity. In the symmetric double well, we cannot distinguish these two processes. For this reason, we combine them to the fidelity p, which we know from previous measurements. Using combinatorics, we can calculate the ideal probabilities n_0, n_1 and n_2:

$$n_2 = n_2'/p^2$$
$$n_1 = n_1'/p - 2(1-p)n_2'/p^2$$
$$n_0 = n_0' - n_1'(1-p)/p + n_2'(1-p)^2/p^2 \quad . \tag{6.6}$$

From this, we calculate the probability for single occupancy $P_1 = n_1$ and the probability for double occupancy $P_2 = n_0 + n_2$.

Figure 6.8 shows the resulting occupation probabilities as a function of the interaction strength for state $|a\rangle$ and state $|c\rangle$. For the non-interacting system we measure equal probabilies of finding single or double occupancy as both atoms distribute equally on both sites. This is the same for both states $|a\rangle$ and $|c\rangle$ and we can therefore not distinguish the two states at that point.

With increasing interaction strength the probability for single occupancy in state $|a\rangle$ rises almost to unity. This can be seen as the two-particle analog of the Mott-insulator state. For attractive interaction, however, the double occupancy becomes more and more favorable leading to a charge-density-wave like state. The excited state $|c\rangle$ shows exactly the opposite behavior. With increasing repulsion, the double occupancy rises. Our measurements are in agreement with calculations from the two-site Hubbard model. The solid lines show the calculated occupancies where $\mathcal{P}_1 = |\langle\psi|LR\rangle|^2 + |\langle\psi|RL\rangle|^2$ and $\mathcal{P}_2 = |\langle\psi|LL\rangle|^2 + |\langle\psi|RR\rangle|^2$.

6.3.3 Resolving the super exchange energy

The emergence of quantum magnetism is based on collective ordering of spins in a material. The underlying mechanism can be explained by the super exchange in a double-well potential. The energy scale of the super exchange is $\frac{4J^2}{U}$ which is often smaller than the scale of the temperature. This complicates its observation in form of anti-ferromagnetic correlations in larger systems [Har15, Gre11]. In [Tro08] the super exchange was observed in a superlattice of double wells by tunneling measurements of bosons. We take a different route to measure the super exchange using the deterministic preparation of eigenstates in the double well. By means of

modulation transfer spectroscopy to the higher lying states we could measure the super exchange energy for two fermions.

Naturally, the super exchange energy is defined as the energy difference between the ground state $|a\rangle$ and the state $|d\rangle$. These two states have different spin wave functions. Transitions between them are only possible if the spin and the spatial degree of freedom couple. In our system, we work in a parameter regime where state $|a\rangle$ and state $|d\rangle$ do not couple. Despite this fact, we can measure the super exchange energy as it is also responsible for the energy splitting of the states $|b\rangle$ and $|c\rangle$.

Modulation transfer spectroscopy

We measure the energy difference between the states $|c\rangle$ and $|b\rangle$ by performing modulation transfer spectroscopy. We prepare state $|c\rangle$ as explained in Section 6.3.1 with different interaction strengths reaching from $U = -1.3\,J$ to $U = +10.1\,J$. Then, we sinusoidally modulate the overall trap depth for 200 ms with an amplitude that varies the tunnel coupling by not more than $0.11\,J$. For the modulation, we choose frequencies between 30 Hz and 300 Hz. If the modulation frequency corresponds to the energy difference, $\Delta E_{\mathrm{b,c}}$, then a resonant transfer of population into state $|b\rangle$ is possible and the population in state $|c\rangle$ decreases.

We probe the resonant transfer of the population by adiabatically ramping back the interaction to $U = 0$ and the tilt to $\Delta = -\frac{1}{2}\hbar\omega_{\mathrm{ax}}$. If the system is still in state $|c\rangle$, both atoms end up in the left well. If the system was transfered into state $|b\rangle$ however, one atom will end up in the left well and one in the right well. We detect the atom number in the right well as a function of the modulation frequency (see inset of Figure 6.9) and extract the resonance frequency with a Gaussian fit.

The energy difference $E_{\mathrm{b,c}}$ does not only tune with the interaction energy U but is also significantly changed when the tilt of the potential is on the order of $4J^2/U$. As the passive stability of the relative depth is limited to about 30 Hz which is on the same scale as the expected super exchange for $U \approx 10\,J$, we perform the modulation transfer spectroscopy for different tilts around $\Delta = 0$. By fitting a numerical calculation of the Hubbard model to the centered data and using the calibrated on-site interaction, we obtain the dashed lines in Figure 6.9. The deviations can be explained by assuming a modified tunnel coupling of $J_{\mathrm{mod}} = (70.7 \pm 0.3)\,\mathrm{Hz} = 1.06 J$ which we obtain by a fit of the data at $U = 0$. The solid lines show the expected energy differences using the modified tunnel coupling. From this fit, we extract the energy differences at $\Delta = 0$.
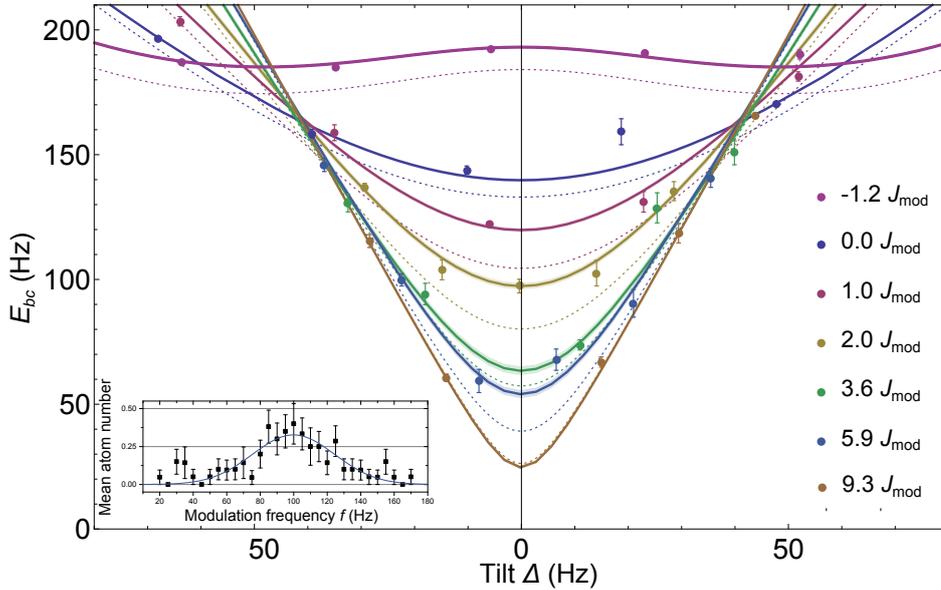
Figure 6.9: Modulation transfer spectroscopy. Starting in state $|c\rangle$ we modulate the overall trap depth by $0.11\,J$ to drive resonant transitions to state $|b\rangle$. Ramping the system back to $U = 0$ and $\Delta \ll 0$ and measuring the average atom number in the right well, we can extract the resonance frequency (Inset). We perform these measurements for different interaction strengths (shown in different colors) and different tilts around $\Delta = 0$. Using the calibrated on-site interaction energy, we fit the position of the balanced trap and can extract the energy difference with a numerical calculation of the Hubbard model (dashed lines). The deviation from the measurement hint towards a modified coupling strength $J_{\mathrm{mod}} = 1.05\,J = (70.7 \pm 0.3)\,\mathrm{Hz}$ due to the periodic trap modulation (solid lines).

Measurement results for the super exchange

The modulation transfer spectroscopy allows us to observe the transition to second-order tunneling. For the non-interacting system we find an energy difference $E_{\mathrm{b,c}} \approx 2J$, which is agrees with the single-particle tunneling rate. As we increase the interaction strength, the energy difference between the two states decreases as single-particle processes are more and more suppressed. It eventually converges to the expected super exchange scale $4J^2/U$ which is described by a second-order tunneling process. By measuring the energy difference between state $|b\rangle$ and state $|c\rangle$ we could resolve the super exchange energy down to $30\,\mathrm{Hz}$ at $U \approx 10J$.

To compare our measurements with the expected energy spectrum of the two-site Hubbard model, we add the energy of state $|b\rangle$ which increases linearly with U to
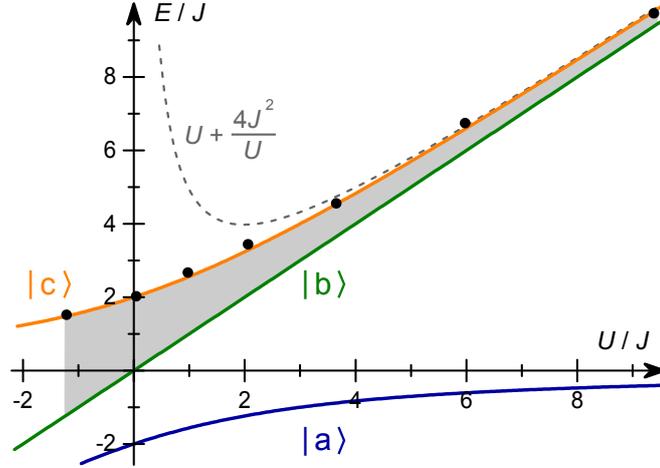
Figure 6.10: Observing the transition from first-order to second-order tunneling. We plot the measured energy difference between state $|c\rangle$ and state $|b\rangle$. To visualize the agreement with the theoretical prediction, we add the energy $E_{|b\rangle} = U$ to the measured values. The dashed line shows the scaling of the super exchange energy derived from second-order perturbation theory. An agreement with the exact solution is only expected at high U/J, where second-order perturbation theory is valid.

the results and plot $U + E_{\mathrm{b,c}}$ in Figure 6.10. The data is in good agreement with the expected super exchange energy.

6.4 Singlet-triplet oscillations

For all our experiments presented so far, we started out with two atoms in a spin singlet state $S = 0$. Adiabatic ramps into the ground state of the double well potential did not act on the spin wave function and so we were restricted to that subspace for the experiments presented above.

To drive a transition from the spin singlet state to the spin triplet state, the symmetry of both the spatial and the spin wave function have to be changed simultaneously. This is possible by coupling the spin and the spatial degree of freedom in the system. This so-called spin-orbit coupling can be achieved by applying a magnetic field gradient to the atoms with different magnetic moments [Tro10]. In the following, we will show how we access the spin triplet by performing singlet-triplet oscillations. Details can also be found in [Mur15a].

6.4.1 Engineering oscillations between singlet and triplet

In the Mott-insulating regime ($U \gg J$), the Hubbard model can be approximated by the Heisenberg model. The effective model assumes single occupation of each site and a spin-coupling with a coupling constant given by the super exchange. We want to drive transitions between the two lowest states, which are a spin singlet and a spin triplet state. Choosing the basis $\{|\uparrow, \downarrow\rangle, |\downarrow, \uparrow\rangle\}$, we can write the Heisenberg Hamiltonian as

$$H = J_{\text{ex}} \left(\mathbf{S_L} \cdot \mathbf{S_R} - \frac{1}{4} n_L n_R \right) = \frac{1}{2} \begin{pmatrix} -J_{\text{ex}} & J_{\text{ex}} \\ J_{\text{ex}} & -J_{\text{ex}} \end{pmatrix} \tag{6.7}$$

If a magnetic field is added to the system, that spatially varies over the double well, and additionally the atoms have different magnetic moments, an energy bias is added between the two states $|\uparrow, \downarrow\rangle$ and $|\downarrow, \uparrow\rangle$. This energy offset is

$$2\Delta_m = (\mu_{\uparrow,L} B_L^z + \mu_{\downarrow,R} B_R^z) - (\mu_{\downarrow,L} B_L^z + \mu_{\uparrow,R} B_R^z) = \Delta B_{\text{L,R}}^z \Delta\mu_{\uparrow,\downarrow} \tag{6.8}$$

where $\mu_{\uparrow,L}$ denotes the magnetic moment of $|\uparrow\rangle$ localized on the left site, and B_L^z is the magnetic field in z-direction at site L. Including this term in the Hamiltonian results in

$$H = \frac{1}{2} \begin{pmatrix} -J_{\text{ex}} + \Delta_m & J_{\text{ex}} \\ J_{\text{ex}} & -J_{\text{ex}} - \Delta_m \end{pmatrix} \tag{6.9}$$

If the magnetic field gradient is zero, we recover the spin singlet and the spin triplet as the eigenstates of the system. In the limit of $\Delta_m \gg J_{\text{ex}}$, the eigenstates of the system are $|\uparrow, \downarrow\rangle$ and $|\downarrow, \uparrow\rangle$. As a consequence, by switching on the magnetic field gradient diabatically, an initial singlet state is no longer an eigenstate and the system will perform an oscillation between the singlet and the triplet state.

6.4.2 Measuring singlet-triplet oscillations

The frequency of this oscillation depends on the energy difference between the two eigenstates $f_{\text{STO}} = 2\Delta_m/h$. In order to observe the oscillation in the experiment, its frequency has to be well above $1\,\text{Hz}$. As shown in equation 6.8, it scales with the difference in the magnetic moments of the two atoms. For all our experiments presented so far, we worked at a magnetic offset field, where the two magnetic moments differ by less than 1%. For the singlet-triplet oscillations, it is favorable to perform our experiments at around $25\,\text{G}$, where the magnetic moments have opposite sign (see Figure A.2). Additionally, the oscillation frequency scales with the difference in magnetic field between the two wells. Due to the small distance between the two wells of about $2\mu\text{m}$, a large $B' = \mathrm{d}B/\mathrm{d}x$ is required. Additionally,
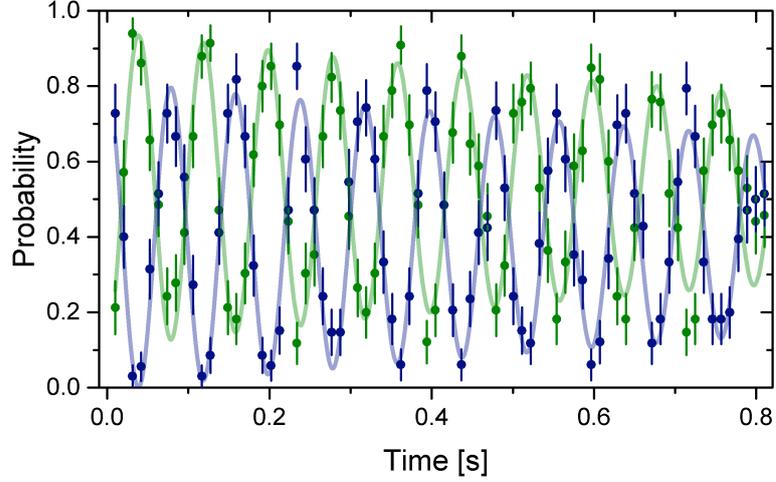
Figure 6.11: Singlet-triplet oscillation. We prepare two fermions with opposite spin in the spin singlet state and quickly ramp the magnetic field down to 25 G and add a magnetic field gradient. As the singlet state is not an eigenstate of the new Hamiltonian (eq. 6.9) the system oscillates to the triplet state and back. We measure the oscillation by mapping the final state to the occupation number of the left well. We plot the probability to detect two fermions (blue, singlet state) and one fermion (green, triplet state) as a function of the evolution time. We observe a frequency of $f_{\mathrm{STO}} = (12.53 \pm 0.03)$Hz. From this we can calculate a magnetic field gradient of (75.9 ± 0.2) mG/cm present during the oscillation. We observe exponential damping with a timescale of about 2 s.

we can only apply a magnetic field gradient along the z-direction in our setup. Only an imperfect alignment of the double well to the symmetry axis of the coils leads to a small magnetic field gradient along the x-direction.

We perform the singlet-triplet oscillations by preparing two fermions in the ground state of the double well and then ramp to an interaction of $U \approx 10J$. After that, we decouple the two wells by increasing the barrier height within 40 ms to $P_{\mathrm{tot}} \approx 900\mu$W. While doing this, we ensure that we do not excite the system into higher trap levels. In that way, we initialized the system in state $\nicefrac{1}{\sqrt{2}}(|LR\rangle + |RL\rangle)$ with pure single occupation. Within 12 ms, we then ramp the magnetic offset field from 740 G to around 25 G. At the same time, we apply a magnetic field gradient and let the system perform singlet-triplet oscillations for some time. We stop the oscillation by quickly ramping the magnetic offset field back to 740 G and the gradient to zero. In order to probe the final state, we couple the double well again and ramp to $U = 0$ and $\Delta \ll 0$. As a result, we observe two particles in the left

well, if the final state was a spin singlet. In case of a spin triplet state $|d\rangle$, we only measure one particle in the left well.

Plotting the result for various evolution times results in oscillations as shown in Figure 6.11. We observe an oscillation with a frequency of $f_{\mathrm{STO}} = (12.53 \pm 0.03)\mathrm{Hz}$. We performed this measurement at a magnetic offset field of $B = 25\,\mathrm{G}$. From the data, we can deduce a magnetic field gradient of $(75.9 \pm 0.2)\,\mathrm{mG/cm}$ along the axis of the double-well potential. The damping time of the oscillation is much longer than for the tunnel oscillation in Section 6.2. This is due to the fact that the oscillation is insensitive to a drift of the potential bias Δ. The only mechanism which leads to the decoherence of the oscillation is an instability in the magnetic field.

As we usually perform all our experiments at high magnetic fields, the prepared ground state $|a\rangle$ is insensitive to decoherence from a residual magnetic field gradient. In the regime of large repulsion, the occupation statistics becomes more and more insensitive to drifts of the tilt Δ. In the next chapter, we use the prepared ground state to study strong correlations between the two interacting fermions.

Chapter 7

Detecting correlations of two atoms in a double-well potential

In the last chapter, we demonstrated the preparation of the fundamental building block of the Fermi-Hubbard model, which consists of two fermions in a double-well potential. Taking this as a starting point, we aim for assembling larger quantum states by preparing several building blocks next to each other and merging them in an adiabatic way. In this way, we will obtain mesoscopic quantum states with strong correlations. We then want to characterize the mesoscopic states by measure the full set of correlation functions.

Using our new imaging technique which provides single-atom and spin resolution (see Chapter 4) we have a tool to characterize prepared quantum states on a single-atom level. By directly detecting each atom after an expansion into momentum space, we can extract the full set of correlation functions that characterizes the state. In the following, we will demonstrate the detection of correlations and benchmark our technique. For this, we study the correlations for the simplest systems that already show interesting correlations: two fermions prepared in the double well potential as presented in Chapter 6. As our technique is scalable, it can be used to study strongly correlated systems with larger particle numbers.

In the first section, we introduce the measurement of correlations in momentum space. We will test it by measuring the first order coherence of a single particle prepared in the double-well potential. In the next step we add a second identical fermion to the system and observe anti-bunching in the correlation function of the two identical fermions. In this way, we can benchmark our correlation detection. Finally we study two interacting fermions prepared in the ground state of the double well. As we increase the interaction between the two distinguishable particles, we observe the increase of correlations in the form of bunching in momentum space.

7.1 Spatial correlation function in real and momentum space

The measurement of correlations allows the characterization of many-body quantum states. Depending on the system, correlations can be present in different observables. Here, we are interested in spatial correlations. In a quantum gas microscope, one has access to the density distribution of the system with site-resolution. By analysing density-density correlations one can for instance identify the Mott-insulating phase or observe dynamics such as the light-cone like spreading of correlations as a function of time after a quench of the system [Che12]. In 2004, Altman et al. proposed the measurement of second-order correlation in momentum space by observing noise correlations in ultracold gases after an expansion in time-of-flight [Alt04]. By measuring the sample with absorption imaging and extracting two-point noise-correlations of each realization, it was possible to measure pair correlations [Gre05]. Furthermore, one observed bunching of atoms in a bosonic Mott-insolator [Fö05] as well as anti-bunching in the fermionic band insulator [Rom06]. In experiments with ultracold fermionic and bosonic Helium atoms, the single-atom resolution in momentum space allowed for the beautiful demonstration of bosonic bunching and fermionic antibunching in Hanbury-Brown Twiss experiments with massive particles [Sch05, Jel07] and the characterization of thermal bosonic samples as well as quasi-BECs [Hod17, Fan16].

In the last chapter, we characterized our prepared states by measuring the occupation statistics per well. With the additional knowledge of having two atoms in the system in more than 95% of the cases, we could infer the site-resolved density distribution of the state in real space $|\Psi(x_1, x_2)|^2$. By changing the interaction energy adiabatically and studying how the occupation statistics evolves, we could identify the prepared state. However, as we measure the absolute square of the wave function in an insitu experiment, we cannot distinguish between a symmetric and an anti-symmetric spatial state at $U \gg J$.

In this chapter, we extract this information by measuring the density distribution of the particles in momentum space $|\tilde{\Psi}(k_1, k_2)|^2$. There, the difference between the symmetric and the anti-symmetric spatial wave function becomes apparent because of the interference of separated parts of the wave function which reveals their phase difference. This works for a one-particle state as well as for a two-particle wave function where the symmetry in the two-particle state influences the two-particle interference pattern. Measuring in momentum space comes to the expense of being insensitive to the sign of an eventual asymmetry in the density-distribution. A combination of measuring the density distribution as well as the momentum distribution of a prepared state, would allow to fully characterize the state.
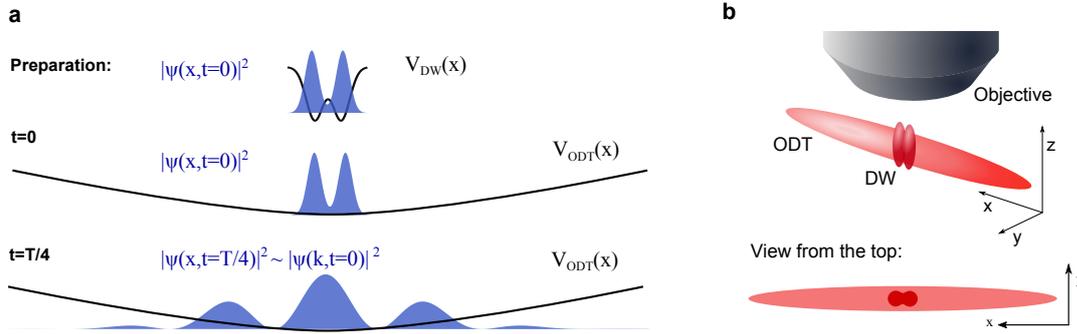
Figure 7.1: Measuring correlations in the double well. a) We start
with a prepared wave function in the double-well potential. At time $t = 0$, we
switch off the double well and let the system expand in the optical dipole trap
(ODT). After a quarter of the trap period T, the momentum distribution
of the initial state translated to a spatial distribution, which we image. **b)**
Optical setup. The high-resolution objective creates two partly overlapping
potential wells. The axis of this double-well potential coincides with the
axial direction of the cigar-shaped optical dipole trap, which we use for the
matter-wave expansion. To image the momentum distribution along the
double-well axis, we let the state expand for $T_{\mathrm{ax}}/4$ and integrate along the
other two directions.

7.1.1 Measuring the momentum distribution in a double well

The momentum distribution can be accessed by performing a ballistic expansion
in free space for a long time, the momentum distribution of a quantum state (at
time $t = 0$) can be mapped to real-space. This mapping can also be achieved
by performing the expansion in a large harmonic trap where after a quarter of
the trap period the position of the particles correspond to the initial momentum
[Mur14]

$$\langle n(\mathbf{q})\rangle_{t=0} \propto \langle n(\mathbf{X})\rangle_{T/4}. \tag{7.1}$$

where the exact proportionality depends on the system. An expansion in a
harmonic trap (see Section 4.4) has the advantage that the atoms remain trapped
at a fixed region and additionally it take a finite amount of time until the spatial
distribution corresponds to the initial momentum distribution.

In our setup, two momentum scales are relevant. The localization of the particles
on the individual wells is described by the Wannier function $\phi(x - x_i)$. For a
deep lattice, it can be approximated by a Gaussian wave function with a width

of σ_x. This results in a momentum uncertainty of the particle of $\sigma_p = \hbar/2\sigma_x$. In addition to this, the distance of the two wells d gives rise to a lattice momentum $\hbar k_{\text{latt}} = 2\pi\hbar/d$.

We will map these momentum scales to position space by an expansion for $T/4$ in a harmonic potential with a trap frequency of ω. The mapping from momentum $\mathbf{q}$ to position $\mathbf{X}$ only depends on the curvature of the potential in which the expansion takes place. From this follows the fringe spacing $\mathcal{D} \propto k_{\text{latt}}$ and the width of the wave function $\sigma_X \propto \sigma_p$ after the expansion

$$\mathcal{D} = \frac{h}{d \, m \, \omega_{\text{ODT}}} \quad \text{and} \quad \sigma_X = \frac{\hbar}{2\sigma_x \, m \, \omega_{\text{ODT}}}. \tag{7.2}$$

In our experimental setup, we let the atoms expand in a cigar-shaped three-dimensional harmonic potential which is created by the optical dipole trap. The setup is shown schematically in Figure 7.1 b). The axis of the double well coincides with the axial direction of the optical dipole trap. Due to the geometry of the harmonic potential, the trapping frequencies are different along the axial and the transversal direction. Therefore, we do not reach momentum space in all directions simultaneously.

We are mainly interested in correlations along the direction of the double well. Consequently, we perform the expansion for $t = T_{\text{ax}}/4$ to reach momentum space along the axial direction of the harmonic potential. During this expansion, the atoms perform several oscillations in the y- and z-direction. After $T_{\text{ax}}/4$ we image the atoms from the top, as shown in Figure 7.1 b which integrates over the z-direction. We perform an additional integration along the transversal direction of the optical dipole trap and obtain

$$n(X, t = T_{\text{ax}}/4) = \iint n(\mathbf{X}, t = T_{\text{ax}}/4) \, \mathrm{d}y \, \mathrm{d}z \,. \tag{7.3}$$

In that way, we obtain the density distribution in one dimension which is proportional to the initial momentum distribution.

For all following measurements that are presented, we chose a trap frequency of $\omega_{\text{ax,ODT}} = 2\pi \times 73\text{Hz}$. Consequently, a distance of $d = 1.5\mu\text{m}$ results in a fringe spacing is $96.6\mu\text{m}$. For the total light power of about $210\mu\text{W}$ in the microtrap one obtains a distribution with a width of $\sigma_X = 50.4\mu\text{m}$.

7.2 Single-particle interference in momentum space

In a first set of experiments, we study single-particle interference of one particle prepared in the spatially symmetric ground state of the double well. For this, we
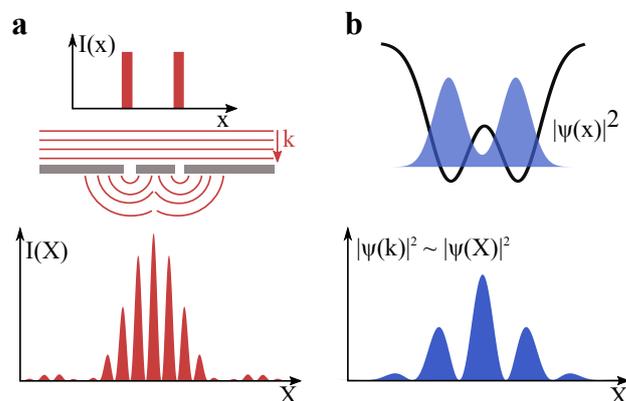
Figure 7.2: Single-particle interference of atoms and light. a) Young's double-slit experiment. Light with a flat wave front is illuminating a double slit. After propagation into the far field, the intensity distribution is measured on a screen. **b)** An atom prepared in the symmetric ground state of a double well potential. The momentum distribution of the particle, detectable e.g. after an expansion in time-of-flight is shown below. In both scenarios (a and b), the fringe distance is determined by the distance of the two slits (Wannier functions) and the envelope is determined by the shape of one single slit (Wannier function).

use the preparation scheme presented in Section 6.3. After that, we let the wave function expand and detect the atom position with our single-atom imaging.

7.2.1 A double-slit experiment with a single particle

The momentum distribution of a single particle in the ground state of a double-well potential can be understood in analogy to Young's double slit experiment with light [You02]. A sketch of a double-slit experiment is shown in Figure 7.2 a. Monochromatic light with a flat wave front falls on a double slit, where it gets blocked everywhere apart from the positions of the two slits. This results in an intensity distribution consisting of two rectangles and no phase difference between the waves. The electromagnetic field then propagates into the far field where one measures the intensity distribution on a screen. Young observed intensity fringes at distances that changed inversely with the distance of the two slits. Furthermore, the envelope of the intensity pattern is determined by the Fourier transform of the intensity distribution through one single slit.

In a similar way, the initial wave function of the particle plays the role of the initial electromagnetic field. As shown for a symmetric double well in Figure

7.2 b the particle is described by the symmetric superposition of being localized in the left or right well $|+\rangle = 1/\sqrt{2}(|L\rangle + |R\rangle)$. After the expansion we detect the position of the particle. Repeating the experiment several thousand times reveals an interference pattern similar to the distribution of the light intensity on the screen[1]. The interference pattern corresponds to the absolute square of the Fourier transformed initial wave function. The Fourier transform of the two parts of the wave function localized at $x = -d/2$ and $x = +d/2$ result in two plane waves with different phases $e^{\pm ikd/2}$. This causes the interference to emerge where symmetric superposition of the two localized wave functions lead to the constructive interference at the center.

7.2.2 Calculating the single-particle interference

We can describe the initally prepared wave function in a more quantitative way and include eventual imperfections in the preparation or the expansion which change the resulting atom density. We assume that we prepared the particle in a pure state with no restrictions on the tilt of the potential Δ. Then the single-particle wave function is described by [Gro99]

$$\Psi(x) = c_L \phi_0(x - d/2) + e^{i\varphi} c_R \phi_0(x + d/2) \tag{7.4}$$

where $\phi_0(x)$ describes the Wannier function in the ground state of one well, c_L and c_R are the probability amplitudes of the individual wells with $c_L^2 + c_R^2 = 1$ which depend on the tilt of the potential. Furthermore, we assume a relative phase φ between the two Wannier functions which can be present from the beginning or accumulate during the expansion. For example, if $\varphi = \pi$, the wave function of the single particle is anti-symmetric.

In the next step, we calculate the Fourier transform of this wave function assuming that we can apply the tight-binding approximation and the Wannier function can be described by a Gaussian wave function with the width of σ_X. The absolute square is described by

$$|\tilde{\Psi}(X)|^2 = \mathcal{N} \exp\left(-2\left(\frac{X}{2\,\sigma_X}\right)^2\right)\left(1 + 2c_L\sqrt{1 - c_L^2}\cos\left(2\pi X/\mathcal{D} + \varphi\right)\right). \tag{7.5}$$

In this expression, we find the two momentum scales, introduced above. The Gaussian function describes the envelope of the interference pattern with a width σ_X which is inversely proportional to the width of the Wannier function of the

---

[1]Performing the expansion of the wave function in the harmonic trap is equivalent to focusing the propagating light with a lens in order to get the Fourier transform of the intensity distribution.
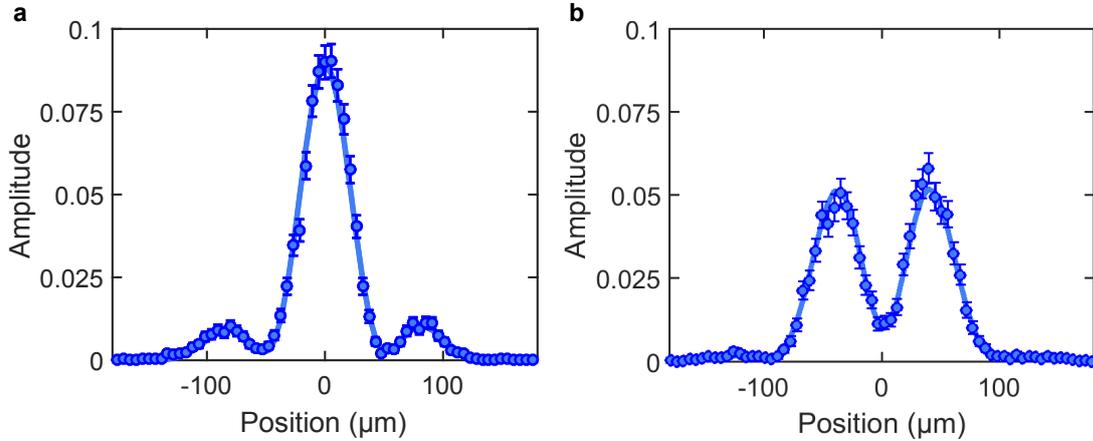
Figure 7.3: Momentum distribution of a single atom prepared in a double well. We prepare a single atom in state $|+\rangle$ (a) and $|-\rangle$ (b). After this, we switch off the trapping potential and let them expand in a large harmonic trap for a quarter of the trap period. We image the atom, detect their position and plot the normalized distribution. The solid lines are fits to the data according to equation 7.5. We find an envelope width of $\sigma_{X,|+\rangle} = (43.4 \pm 0.5)\mu$m and $\sigma_{X,|-\rangle} = (47.8 \pm 0.5)\mu$m, and fringe spacings of $\mathcal{D}_{|+\rangle} = (102.1 \pm 0.8)\mu$m and $\mathcal{D}_{|-\rangle} = (96.1 \pm 0.7)\mu$m.

localized particle. The cosine function describes the actual interference with a spacing caused by the lattice momentum. Additionally, a probability amplitude of $c_L^2 = 0.5$ which corresponds to $\Delta = 0$ leads to full visibility of the interference fringes and a finite value of φ causes the interference pattern to shift away from the center. In the extreme case of $\varphi = \pi$, we observe destructive interference at the center. $\mathcal{N}$ takes care of the normalization.

7.2.3 Preparation and quantitative analysis

In the experiment, we prepare two non-interacting particles in the ground state of a single well and then ramp adiabatically into the ground state of the double well with a depth of 2.6μK, as explained in detail in Section 6.3. During the preparation of the quantum state in the double well, we additionally ramp on the optical dipole trap making sure that no heating occurs. After this, we switch off the double-well potential and let the system expand in the optical dipole trap. After $3.5\,$ms, we image the atoms with single-atom resolved fluorescence imaging and extract their position as well as their hyperfine spin.

As the atoms do not interact we can consider them as independent. Here, we

only analyse the data of one of the two atoms. Figure 7.3 a shows the normalized distribution of the measured position of the atom in the symmetric ground state of the double well in about 3000 realizations. The distribution shows constructive interference in the center with a fitted visibility[2] of $\mathcal{V}_{|+\rangle} = (89.8 \pm 1.4)\%$. The positions of the side maxima corresond to a momentum difference of one lattice momentum. Figure 7.3 b shows the normalized position distributions for the anti-symmetric state $|-\rangle \propto (|L\rangle - |R\rangle)$ with destructive interference in the center of the distribution and a visibility of $\mathcal{V}_{|-\rangle} = (77.4 \pm 1.4)\%$.

From the fits to the data according to equation 7.5, we extract information about the momentum distribution in the double well. We find an envelope width of $\sigma_{X, |+\rangle} = (43.4 \pm 0.5)\mu$m and $\sigma_{X, |-\rangle} = (47.8 \pm 0.5)\mu$m, that is in agreement with the measured envelope width in Section 4.4. Furthermore, we determine fringe spacings of the interference pattern. For the symmetric state, we obtain $\mathcal{D}_{|+\rangle} = (102.1 \pm 0.8)\mu$m and the spacing of the anti-symmetric state amounts to $\mathcal{D}_{|-\rangle} = (96.1 \pm 0.7)\mu$m. From the fit to the data, we can bound the eventual phase evolution of the states during time-of-flight to be smaller than $(0.003 \pm 0.01)\pi$.

If we assume the preparation of a pure state, we can deduce how much our prepared state deviated from the symmetric ground state via the fringe visibility $\mathcal{V}$. From the fits, we deduce a residual tilt that is smaller than $|\Delta_+| \approx 0.5\,J$ and $|\Delta_-| \approx 0.85\,J$. As we are measuring the absolut square of the wave function, we cannot determine the sign of the tilt.

However, the fringe visibility can also be reduced by the finite resolution of the momentum measurement. With the calculated momentum uncertainty of $\Delta k/k_{\text{latt}} \approx 8\%$, the visibility would be reduced to at most 92%. Additionally, it can be reduced by the preparation of a mixed state. With the available information, however, we cannot distinguish between a visibility reduction due to a pure state in a tilted potential or the preparation of a mixed state.

7.3 Correlations of two identical fermions

The observation of interference in the density distribution in momentum space gave us insight into the coherence of a single atom prepared in a quantum state. In a next step, we want to observe the quantum statistics of two identical fermions. In order to observe the exchange statistics of the two particles, we study the two-point correlation function in the momentum distribution. Similar to the momentum density distribution, we can access the two-point correlation by an expansion of

---

[2]The visibility has been extracted from a fit with equation 7.5, where $\mathcal{V} = 2c_L\sqrt{1 - c_L^2}$. This is equivalent to the common definition $\mathcal{V} = A_{\max} - A_{\min}/A_{\max} + A_{\min}$ where $A_{\max,\ \min}$ denotes the maximum and minimum amplitude of the signal.
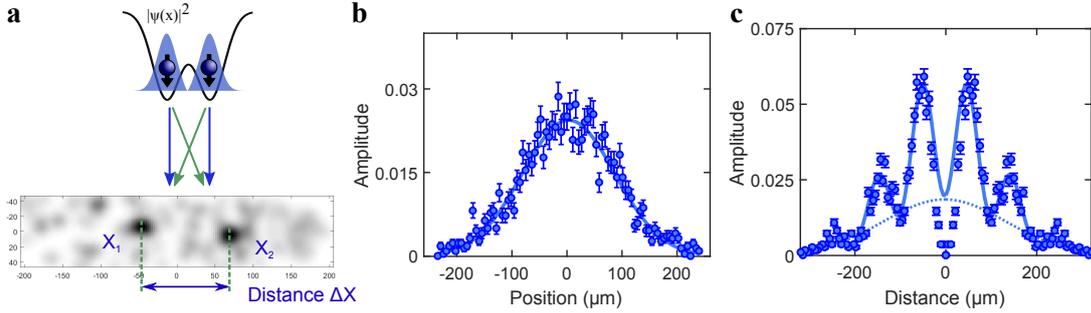
Figure 7.4: Two-particle interference of two identical fermions. a)
We prepare two identical fermions in the double-well potential. Due to
the Pauli principle, they occupy different single-particle quantum states.
The indistinguishability leads to a destructive interference between the two
depicted paths (green and blue). After expansion we detect the positions
of the two particles X_1 and X_2. **b)** The single-particle density distribution
does not show interference fringes. **c)** The distribution of the measured
distances between two detected particles shows clear interference fringes with
a visibility of 69%.

the particles in the harmonic potential of the optical dipole trap and obtain

$$\langle \hat{n}(X)\hat{n}(X') \rangle_{T/4} \propto \langle \hat{n}(q)\hat{n}(q') \rangle_{t=0} \,. \tag{7.6}$$

The total wave function of identical fermions is anti-symmetric with respect to
particle exchange. Consider a system with two identical fermions in the overall
ground state. Then one fermion occupies the single-particle ground state $\phi_0(x)$
and the other particle occupies the single-particle first excited state $\phi_1(x)$. The
indistinguishability leads to the following total wave function

$$\Psi(x_1, x_2) \propto (\phi_0(x_1)\phi_1(x_2) - \phi_0(x_2)\phi_1(x_1)) \left| \uparrow\uparrow \right\rangle \,. \tag{7.7}$$

In a double-well potential, the ground state wave function $\phi_0 \propto \phi_+$ and the first
excited state corresponds to $\phi_1 \propto \phi_-$. In the limit of tight binding, one can write
the wave function in the Wannier basis $\phi_{L,R}$

$$\Psi(x_1, x_2) \propto (\phi_L(x_1)\phi_R(x_2) - \phi_L(x_2)\phi_R(x_1)) \left| \uparrow\uparrow \right\rangle \,. \tag{7.8}$$

We use the preparation scheme to initialize a state with two identical fermions
in the two lowest bound states of a single microtrap. After that, we add a second
potential well and use an adiabatic ramp to shift one of the particles into the
lowest state of the second well. The density distribution of the state is depicted in

Figure 7.4 a. After the preparation, we ramp the total power of the double-well potential up to 1.3 mW within 40 ms before we switch off the double-well potential, let the wave function expand in the optical dipole trap and image the atoms.

7.3.1 Density distribution of single particles

A distribution of the detected positions of the two atoms in the same hyperfine state is shown in Figure 7.4 b. In contrast to the single-particle system, we do not observe interference fringes in the density distribution of the particles. We can fit the density distribution with a Gaussian distribution and extract a width of $(84.1 \pm 1.5)\mu$m. It corresponds to the expected width from the expansion of a single atom.

We can explain the absence of the interference pattern by calculating the expected density distribution of the prepared state. The fact that each of the identical fermions occupies one well, can be expressed in the Fock basis

$$|1,1\rangle = \hat{a}_R^\dagger \hat{a}_L^\dagger |0\rangle \tag{7.9}$$

where the creation and annihilation operators obey the fermionic anti-commutation relations and $\hat{a}_i^\dagger$ describes the creation of one particle at site i. Consequently, the expectation value of the number operator $\langle \hat{a}_l^\dagger \hat{a}_j \rangle = \delta_{jl} n_l$. We observe the quantum statistics in the momentum distribution. To express this, we construct the creation and annihilation operators in momentum space

$$\hat{b}_i = \sum_j \hat{a}_j \mathrm{e}^{ik_i x_j} \tag{7.10}$$

We can then calculate the density distribution in momentum space

$$\langle n(q) \rangle = \langle \hat{b}_i^\dagger \hat{b}_i \rangle = |\tilde{\phi}(q)|^2 \sum_{j,l} \mathrm{e}^{i(k_i x_j - k_i x_l)} \langle \hat{a}_l^\dagger \hat{a}_j \rangle \tag{7.11}$$

where $\tilde{\phi}(q)$ describes the single-particle wave function in momentum space.

Applied to the state containing two localized identical fermions, the density distribution is described by

$$\langle n(q) \rangle = |\phi(q)|^2 \sum_{j,k} \mathrm{e}^{ik(x_i - x_j)} \delta_{kj} n_j \tag{7.12}$$

$$= N_{\text{tot}} |\phi(q)|^2 \tag{7.13}$$

where N_{tot} describes the number of particles contained in the quantum state. The calculated density distribution only features the envelope of the single particle but no interference pattern, as observed in the experiment.

7.3.2 Two-point correlations between two particles

The single-particle density distribution does not show interference fringes. Nevertheless, the two-particle wavefunction described in equation 7.8 contains correlations. To extract the correlations, we determine the distance between the two atoms $\Delta X = |X_1 - X_2|$ detected for each realization of our experiment and plot their distribution. The distribution of distances for about 4000 shots is shown in Figure 7.4 c. It shows an interference pattern with a large contrast. We observe anti-bunching at integer lattice momenta because the identical fermions do not occupy the same momentum modes due to the Pauli exclusion principle. Instead we observe a high probability to find the two particles at distances to each other, which correspond to half-integer lattice momenta.

For a quantitative analysis, we study the magnitude of the detected visibility. In case of a perfect preparation, the quantum system would be in a pure state for which one expects full anti-bunching. Our data shows a large contrast on the order of 70%. At zero distance, we observe a very low probability of events in the experiment. However, this is not only caused by anti-bunching of the identical fermions but also an artifact of our imaging method: When two atoms have only a small distance to each other, our the detection method cannot resolve them as two distinct atoms which are close together. As the photon signals of the two atoms overlap significantly, these events are instead counted as events containing only one atom and rejected in the post selection process. The minimum distance at which two atoms are identified correctly is determined by the typical size of the photon distribution. We estimate this distance to roughly 6 pixel.

In a periodic potential, two identical fermions also show anti-bunching at the integer multiples of the lattice momentum. Using this fact, we determine a visibility of $(68.8 \pm 3.6)\%$ in our experiment. This is to our knowledge the first time that destructive two-particle interference at that scale is observed in an experiment with identical fermions. We attribute the reduction from full contrast to imperfection in the preparation which lead to excitations in the system. These excitations do not destructively interfere and thus add up to the signal as a single-particle amplitude. We fit an underlying Gaussian function to the fringes that has an amplitude of $\approx 30\%$ of the full signal amplitude.

7.3.3 Extracting correlations from the momentum distribution

We can calculate the expected wave function in momentum space by a fourier transform of the quantum state given in real space in equation 7.8. In this way, a particle on the left well is mapped to $|L\rangle \to \tilde{\phi}(k_j)\, \mathrm{e}^{-ik_j d/2}$ and a particle on the right
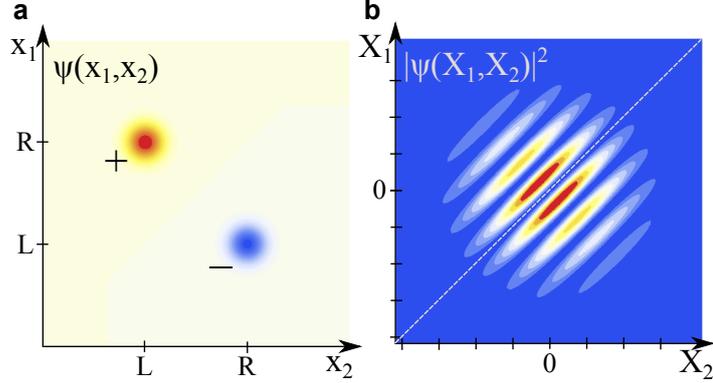
Figure 7.5: Two-particle interference of two identical fermions. a)
One-dimensional wave function of two identical fermions in real space. The
coordinate of the two particles x_1 and x_2 are plotted as the two axes. The
wave function only has finite values when one particle is localized on the
left well and the other is localized on the right well. The sign of the two
contributions $|LR\rangle$ and $|RL\rangle$ is opposite. **b)** Absolute square of the mo-
mentum distribution of two identical fermions in a double-well potential.
The momentum distribution is obtained by fourier transformation of the
real space wave function. Experimentally, we access it by an expansion in
time-of-flight where the particle momentum gets mapped to the detected
position $k_i \propto X_i$. The plot illustrates, that the fringes in the momentum
distribution originate from a two-particle interference. The shift of the fringe
pattern is caused by the different signs of the two contributions in real space.

well is mapped to $|R\rangle \rightarrow \tilde{\phi}(k_j)\, \mathrm{e}^{ik_j d/2}$, where $\tilde{\phi}$ denotes the fourier transformed
Wannier function. Consequently, we obtain the momentum space wave function

$$\tilde{\Phi}(k_1, k_2) \propto \tilde{\phi}(k_1)\, \tilde{\phi}(k_2) \left(\mathrm{e}^{-ik_1 d/2}\mathrm{e}^{ik_2 d/2} - \mathrm{e}^{ik_1 d/2}\mathrm{e}^{-ik_2 d/2} \right) \qquad (7.14)$$

$$\propto \frac{1}{i}\tilde{\phi}(k_1)\, \tilde{\phi}(k_2)\, \sin((k_2 - k_1)d/2) \qquad (7.15)$$

with k_1 and k_2 denoting the momenta of the two identical fermions. The two-
particle wave function in real space $\Phi(x_1, x_2)$ and absolute square of the momentum
space wave function $|\tilde{\Phi}(k_1, k_2)|^2 \propto |\tilde{\Phi}(X_1, X_2)|^2$ are sketched in Figure 7.5. The
sketch illustrates that the momentum distribution of the two-particle wave function
can be understood from a two-particle interference where the different signs of the
amplitudes in the real space wave function results in a phase shift of the fringes in
the density distribution in momentum space.

We compare this calculation with our data. For this we extracted the detected
positions X_1 and X_2 of the two atoms for each realization and plot the distribution
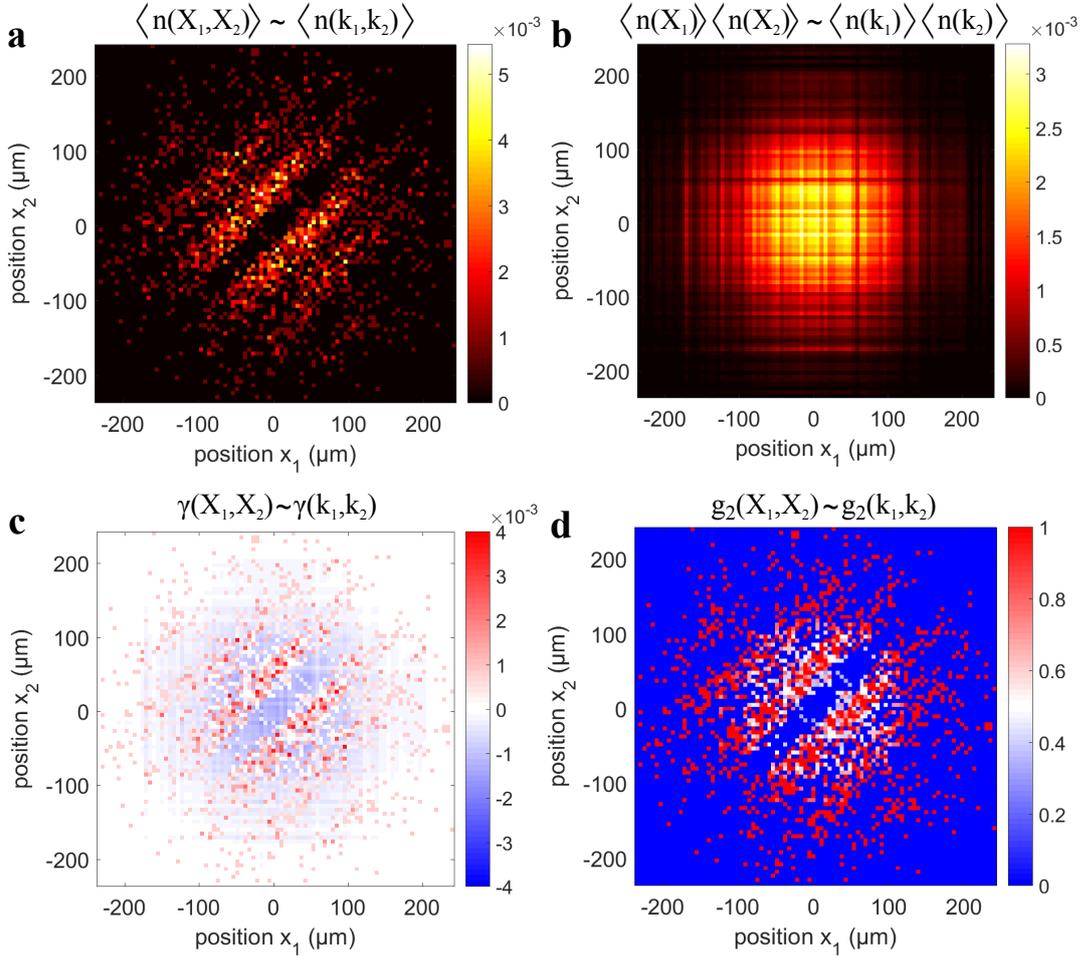
Figure 7.6: Correlation function of two identical fermions. **a)** Normalized distribution of positions where the identical particles are localized $\langle n(X_1, X_2) \rangle$. **b)** Outer product of the uncorrelated part of the distribution $\langle n(X_1) \rangle \langle n(X_2) \rangle$. **c)** Two-dimensional covariance matrix $\gamma_2(X_1, X_2)$ calculated from a) and b). Non-correlated regions and regions with low signal have values around zero. Anti-bunching and bunching correspond to negative and positive values, respectively. **d)** Two-dimensional normalized correlation function $g_2(X_1, X_2)$. Values around 0.5 correspond to no correlation. Values smaller than 0.5 correspond to anti-bunching whereas values larger than 0.5 correspond to bunching. The large variations in the outer part are due to devision through a small signal.

of the extracted position pairs as data points (X_1, X_2) into a diagram. As the fermions are indistinguishable, we mirror the distribution on the diagonal $X_1 = X_2$. The resulting distribution shown in Figure 7.6 a corresponds to the absolute square of the two-particle momentum distribution $\langle n(k_1, k_2) \rangle$. The data shown in Figure 7.6 a is in qualitative agreement with our expectation from the momentum distribution of the two-particle system and we observe interference fringes along the diagonal. Additionally, we do not observe any momentum dependence on the center-of-mass momentum of the particles $X_1 + X_2$ in the data.

To study the correlations between the two identical particles, we want to extract only the correlated part of the data. To do this, we first calculated the uncorrelated part of the single-particle density distribution by summing the data along X_2 and X_1 separately. From this, we obtain two vectors $\langle n(X_1) \rangle$ and $\langle n(X_2) \rangle$ that consist of two Gaussians caused by the single-particle wave functions. By constructing the outer product of the two vectors, we obtain the two-dimensional distribution shown in Figure 7.6 b. We can then subtract this outer product which represents single-particle physics from the data. This is known as the covariant matrix and defined as

$$\gamma_2(X_1, X_2) = \langle n(X_1, X_2) \rangle - \frac{1}{2} \langle n(X_1) \rangle \langle n(X_2) \rangle . \tag{7.16}$$

In the case of totally uncorrelated atoms $\langle n(X_1, X_2) \rangle = (1 - \frac{1}{N}) \langle n(X_1) \rangle \langle n(X_2) \rangle$, with N the number of particles in the quantum state and consequently, the covariant matrix $\gamma_2(X_1, X_2)$ takes the value zero everywhere. In regions with few data points, the resulting values for $\langle n(X_1, X_2) \rangle$ and $\langle n(X_1) \rangle \langle n(X_2) \rangle$ are both small and so, the covariance matrix is not very sensitive to shot noise.

Figure 7.6 d shows the calculated covariant matrix for two identical fermions. We observe clearly visible correlations along the diagonal which corresponds to bunching for $\gamma_2(X_1, X_2)$ having positive values and shows anti-bunching where $\gamma_2(X_1, X_2)$ has negative values. The amplitude of the values in the covariant matrix cannot exceed the one of the initial data set and still shows remnants of the single-particle wave function.

The covariance matrix gives us information about the presence of correlations in the system. However, using a normalized function is more suited to quantify the strength of the correlations. Therefore, we also calculate the two-particle correlation function $g_2(X_1, X_2)$ of our data. It is defined as

$$g_2(X_1, X_2) = \frac{\langle n(X_1, X_2) \rangle}{\langle n(X_1) \rangle \langle n(X_2) \rangle} . \tag{7.17}$$

For uncorrelated states with N atoms, the correlation function $g_2(X_1, X_2)$ has a value of $1 - \frac{1}{N}$ which is close to 1 for large N. Therefore, in the literature, the two-point correlation function is often defined with an additional subtraction of 1.

In our case, the subtraction of 1 does not make much sense. For two uncorrelated particles, we expect a value of ½. Our experimental result is shown in Figure 7.6 c, with clear oscillation between values of zero (anti-bunching) and one (bunching). In the outer region of the distribution, however, shot noise leads to large variations of the values and the division by $\langle n(X_1) \rangle \langle n(X_2) \rangle$ can be problematic. To avoid a division by zero, we add a small positive value on the order of 10^{-5} to the denominator and so the values in the outer region exceed 1 but stay finite.

7.3.4 Extracting the one-dimensional correlation function

The full correlation function $g_2(X_1, X_2)$ of two particles does not show any dependency on the center-of-mass coordinate. Therefore, we do not lose information when we integrate along the diagonal. In that way, we obtain a one-dimensional quantitative observable of the quantum state, which is more comparable to observables used in [Fö05, Rom06]. We use equation 7.17 and integrate over the center-of-mass position $X' = X_1 + X_2$. From this we obtain

$$C(\Delta X) = \frac{\int \langle \hat{n}(X' - \Delta X/2) \, \hat{n}(X' + \Delta X/2) \rangle \, dX'}{\int \langle \hat{n}(X' - \Delta X/2) \rangle \langle \hat{n}(X' + \Delta X/2) \rangle \, dX'} \tag{7.18}$$

Note that also here, we do not subtract unity from the calculated correlation function, in contrast to the definition in [Föl14].

Figure 7.7 a shows the calculated result for our data. We observe oscillations around a value of $1 - 1/N = 0.5$ over the distance which corresponds to about three lattice momenta. Values smaller than 0.5 indicate anti-bunching, whereas bunching is observable if the correlation function is above 0.5. At large distances, the noise on the data points increase. The reason for this is that these events are very rare and have a large relative shot noise. Consequently, the full data as well as the uncorrelated part of the data have large noise which is additionally increase by normalization.

The integration along the center-of-mass coordinate offers the possibity to quantitatively determine the correlations in our system. In case of a perfectly prepared system of two identical fermions in a pure state, we expect the two-point correlation function described by

$$C(\Delta X) = -0.5 \cos(k_{\text{latt}} \Delta X) + 0.5 \,, \tag{7.19}$$

where the resulting function will oscillate between zero (anti-bunching) and 1 (bunching). In our experiment, we observe a visibility of about 70% of the expected amplitude for a pure state. We attribute the reduction of the contrast to the detection of a mixed state with state components that do not show an
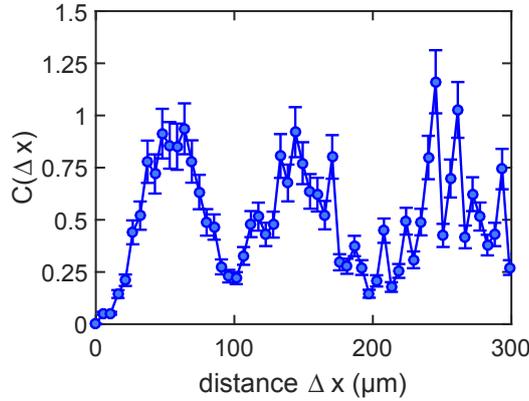
Figure 7.7: Distance correlation of two identical fermions. Normalized correlation function of the detected distances between two identical fermions. We observe oscillations over a distance that corresponds to three lattice momenta. The data show anti-bunching (bunching) at (half integer) integer lattice momenta where the correlation function has values below (above) 0.5. Full bunching and antibunching is expected at $C(\Delta X) = 1$ and $C(\Delta X) = 0$. The two-particle interference fringes reach a visibility of about 70% of the possible amplitude.

interference pattern. All in all, the anti-bunching of two identical fermions is clearly detected.

7.4 Emergence of correlations between two interacting fermions

In the last section, we discussed that identical fermions show two-particle correlations in the form of anti-bunching. A system of fermions in two different spin states does not necessarily show correlations in the spatial degree of freedom. In a non-interacting system, the two particles are independent in the spatial degree of freedom and the Hilbert space can be separated into two subspaces which correspond to the two spin states. Consequently, no correlations are present between the subspaces. Interactions between particles in different spin states couple the Hilbert subspaces and introduce spatial correlations. The strength of these correlations depends on the interaction strength in the system. These correlations are responsible for interesting low-temperature phases [Sac08]. The emergence of spatial correlations can already be observed in a system of two fermions with different hyperfine spin state prepared in a double-well potential.

7.4.1 Uncorrelated fermions

The spatial wave function of two non-interacting fermions with different spins can be described by a product state of the single-particle wave functions $\Phi(x_1, x_2) = \phi(x_1)\phi(x_2)$. In this case, the expectation value of the density distribution can be written as the product of the two subsystems $\langle n(x_1, x_2) \rangle = \frac{1}{2} \langle n(x_1) \rangle \langle n(x_2) \rangle$. As a consequence, the two particles are not correlated and the covariance matrix shows values of zero.

This can be seen for two non-interacting fermions that are simultaneously prepared in the ground state of the double-well potential. Independently from each other, the two fermions show a single-particle interference pattern, as already explained in Section 7.2. Figure 7.8 a shows this single-particle interference in the density distribution $n(X_1, X_2)$ after the expansion of the prepared state into momentum space. As expected, the covariance matrix $\gamma(X_1, X_2)$ which measures the two-particle correlation, has values around zero (see Figure 7.8 d) and the correlation function of the distances $C(\Delta X)$ does not feature oscillations but stays constant around the value expected for an uncorrelated system $C(\Delta X) = 1 - \frac{1}{N} = 0.5$.

7.4.2 Building up correlations

As soon as an interaction is present between the two fermions, the total wave function cannot be written as a product of two single-particle states anymore and the interaction leads to a build-up of correlations between the two particles. One can already observe a qualitative difference looking at the density distribution $n(X_1, X_2)$ of the ground state in the double well. Figure 7.8 b and c shows two realizations with different repulsive interaction strengths between the atoms where we prepared the two fermions in the ground state of the double-well potential according to the technique presented in Section 6. The data shows, that the distribution is not symmetric around the $X_{1,2} = 0$ axes anymore. Instead stripes along the diagonal form.

In contrast to the distribution of the identical fermions, we observe bunching of the repulsively interacting particles in form of constructive interference for integer multiples of the lattice momentum. Such a bunching effect is also expected from identical interacting bosons. The reason for this is that the constructive interference stems from the symmetry of the spatial wave function, which is symmetric for identical bosons, as well as fermions that form a spin singlet.

To make the two-particle correlation visible, we plot the covariance matrix $\gamma(X_1, X_2)$ (Figure 7.8 d-f), where pure two-particle correlations are encoded by deviations from zero. Similar to the system of identical fermions, the emergence of
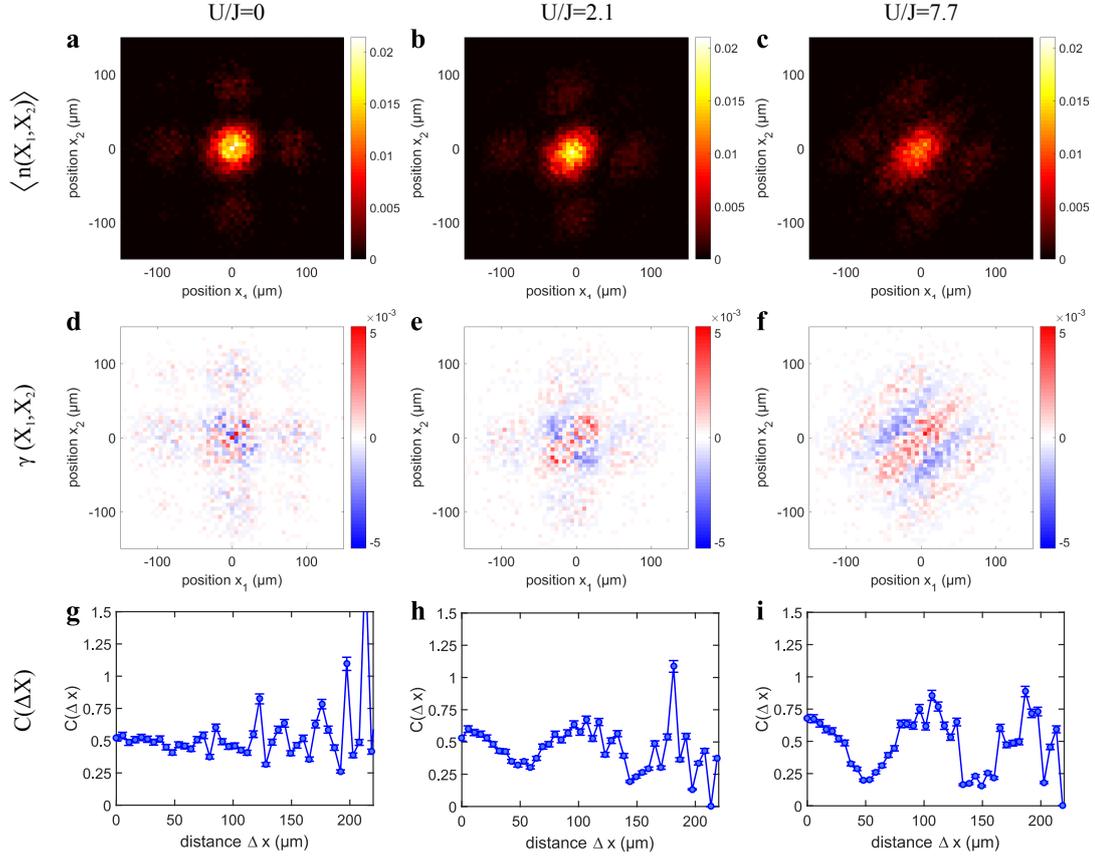
Figure 7.8: Emergence of strong correlations. We prepare two fermions with different spins in the ground state of the double-well potential. We measure the momentum distribution of the system with single-atom resolution as a function of the interparticle interaction. We plot the density distribution $n(X_1, X_2)$ (a-c) after the expansion into momentum space for different interaction strengths. d-f show the two-particle correlations $\gamma(X_1, X_2)$ with anti-bunching for negative and bunching for positive values. The distance correlator $C(\Delta X)$ is shown in (g-i). From left to right, we increase the interaction strength in the system. The emergence of correlations manifests itself in the increasing oscillation amplitude of the correlation function.

the correlations is visible as blue (anti-bunching) and red (bunching) areas, that form longer and longer stripes for increasing repulsive interaction. Figure 7.8 g-i shows the increase in correlations with the interaction strengths as increasing contrast in the oscillations of the distance correlation function $C(\Delta X)$. It shows bunching at distances of zero and integers of the lattice momentum and anti-bunching at half integers of $\mathcal{D}/2$. For the largest interaction strength, we observe a visibility of about 60%.

7.4.3 Comparison with the Hubbard model

With increasing interaction strength, we observed an increasing contrast of the distance correlation function. In order to describe this emergence of correlation in a quantitative way, we choose an appropriate spatial basis to analyse the momentum distribution. The basis of Bell states [Nie04] is especially suited for the description, because all its states show full correlation along the diagonal $X_1 = X_2$ or the anti-diagonal $X_1 = -X_2$. For infinitely strong on-site interaction, they are eigenstates of the two-site Hubbard model

$$|S\rangle = \frac{1}{\sqrt{2}} \left(|LR\rangle + |RL\rangle \right) \tag{7.20}$$

$$|T\rangle = \frac{1}{\sqrt{2}} \left(|LR\rangle - |RL\rangle \right) \tag{7.21}$$

$$|D_+\rangle = \frac{1}{\sqrt{2}} \left(|LL\rangle + |RR\rangle \right) \tag{7.22}$$

$$|D_-\rangle = \frac{1}{\sqrt{2}} \left(|LL\rangle - |RR\rangle \right) \tag{7.23}$$

Usually, they are used to describe two-qubit states and are often called EPR pairs after the Gedankenexperiment of Einstein, Podolsky and Rosen. One of their properties is, that although the measurement of the first qubit is randomly distributed, the result of the second qubit is correlated to the first result. We already observed this in the case of two identical fermions, which have a triplet spatial wave function $|T\rangle$.

In the following, we analyse the ground state of the two-site Hubbard model. To do this, we write the state in the Bell basis

$$|gs\rangle = c_S(U) |S\rangle + c_D(U) |D_+\rangle \tag{7.24}$$

with the prefactors $c_S(U)$ and $c_D(U)$ that depend on the on-site interaction U. For $U = 0$, the singlet and the symmetric doublet state contribute equally to the state as $c_S(U) = c_D(U)$ and we do not expect a two-particle correlation. However, when
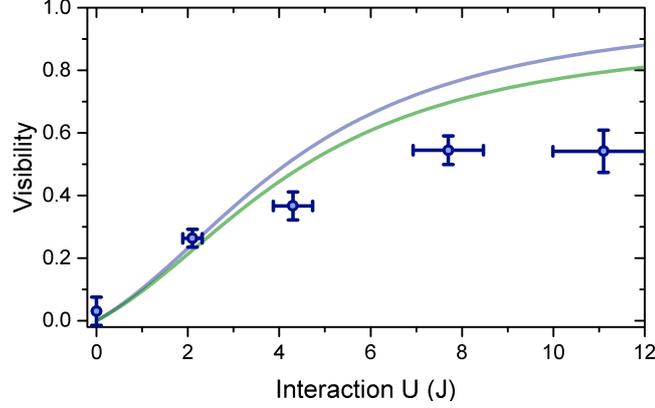
Figure 7.9: Visibility as a function of the on-site interaction. Measured visibilities for two fermions prepared in the ground state of a double-well potential. The data shows measurements at magnetic fields between $568\,\text{G}$ and $655\,\text{G}$. From the data, we calculated the distance correlation function and fitted a sinusoidal oscillation in the range between 0 and $1.5\,k_{\text{latt}}$. The fitted amplitudes are compared to the theoretical expectation for the ground state (blue solid line). The green solid line takes into account a reduction of the contrast by 5% due to the finite momentum resolution.

$U > 0$, then the contribution of the singlet increases ($c_S(U) > c_D(U)$), and the distance correlation function shows an oscillation with increasing contrast $\mathcal{V}(U)$. In the limit of $U \gg J$, the contribution of the singlet governes the momentum distribution and the fringes reach full contrast. We can calculate the expected correlation function $C(\Delta X)$ of the ground state (eq. 7.24) and obtain

$$C(\Delta X) = \frac{\frac{1}{2}(1 + c_S(U)^2 \cos(2\Delta X))}{(1 + 4c_S(U)^2 c_D(U)^2 - 2c_S(U)^2 c_D(U)^2 \cos(2\Delta X))}. \tag{7.25}$$

From this expression, we can deduce the expected visibility to be $\mathcal{V}(U)$.

We want to compare the expected contrast to the experimental observations. For this, we extract the observed correlations for different interaction strengths from the distance correlation function by fitting a sinusoidal oscillation. As the oscillations are only visible in a range from 0 to $1.5k_{\text{latt}}$, we select this region of the fit of the sinusoidal function. Figure 7.9 shows the fitted visibility as a function of the interaction strength. We can clearly observe an increase of contrast as a function of the interaction strength. To compare with a pure state, we show the calculated visibility from the ground state of the Hubbard model. Our measurements cannot completely reproduce the ideal contrast[3]. This can be

---

[3]The experiments presented here were performed at different parameters than the experiments

explained by an admixture from other states in our prepared system. However, the observed contrast has the same scale as the expectations and demonstrates our sensitivity on strong correlations in the system. In the future, we aim for developping an analysis which allows us to determine the density matrix which describes the prepared system. It will allow us to infer the pureness of our preparation technique and maybe quantify entanglement in the system.

Summary and outlook

In this Chapter, we presented measurements of single-particle interference and two-particle correlation functions that showed almost full contrast. We could observe anti-bunching of two fermions in the same hyperfine state which demonstrates their indistinguishability. The observed two-particle interference has a visibility of 69% which is to our knowledge the largest contrast for anti-bunching of identical fermions observed so far. The observation of such a high contrast was possible because of a deterministic state preparation as well as a detection of the quantum state on the single-particle level. For two fermions in different spin states, we could observe the emergence of correlations as a function of the interparticle interaction strength by measuring the contrast of the oscillations in the correlation function.

In the near future, we aim for quantifying the admixture of other states that reduces the contrast in the correlations to obtain a bound on the pureness of the system. To do this, we will use the density matrix formalism to reproduce measured correlation pattern. With this, we obtain all entries of the density matrix for every state, we prepare. This will deliver a new tool to characterize prepared states with larger particle number. Last but not least, this may allow us to gain information about entanglement present in a strongly correlated quantum state.

---

presented in Chapter 6. Therefore, the data are not in contraction with the data from the occupation statistics in the double well.

Chapter 8

Conclusion and Outlook

In this thesis, we investigated few-fermion systems with strong correlations. For two different systems, we developed techniques to deterministically prepare interacting few-fermion quantum states and measure their correlations. In the future, we want to use them to assemble and study larger quantum states.

In a first set of experiments, we studied *one impurity interacting with a number of majority particles* that gradually form a Fermi sea (Chapter 5.3). We prepared the few-particle system in a cigar-shaped confinement in the one-dimensional limit. To probe the impurity system, we measured the wave function overlap between the interacting impurity system and the non-interacting state. We observed the decrease of the overlap with increasing particle number, which manifests the many-body properties of the system and is in agreement with the expectations from the Anderson orthogonality catastrophe. It can be used to benchmark theoretical predictions on one-dimensional systems and is the starting point for further investigation of the impurity problem.

In a second set of experiments, we realized the *two-site Hubbard system* by preparing two fermions in a double-well potential, that we generate by two partially overlapping optical tweezers (Chapter 6). We show full control on the tunnel coupling between the wells and the on-site interaction [Mur15b]. By controlling the wells of the potential separately, we adiabatically ramp two fermions into the ground state of the double-well potential with fidelities that exceed 90%. We adiabatically increased the repulsive (attractive) interaction and observed a decrease (increase) in double occupancies which is expected in a Mott-insulator (charge-density wave) regime. Furthermore we resolved the super exchange energy which causes a system to favor anti-ferromagnetic ordering. By preparing the ground state of the two-site Hubbard model, we can create a state with non-local correlations.

We could study these correlations using a *novel imaging technique* which was developed in the course of this thesis. This technique allows us to detect single atoms in free space and additionally resolve their hyperfine spin state (Ch. 4).

We use fluorescence imaging and collect a fraction of the emitted photons with a high-resolution objective. In that way, we detect about 20 photons per atom with an EMCCD camera. By using image processing, we can identify single atoms with fidelities of 98% and determine their position with an uncertainty of 1.4 pixel. We can apply the new imaging method also after an expansion into momentum space. For this, we let the atoms expand in a large cigar-shaped potential for a quarter of the axial trap period. This expansion maps the initial momentum of the atoms to their position. As this technique works for many atoms, we can obtain full information about few-particle quantum states by measuring their momentum distribution on a single-atom level with spin resolution.

With this imaging we *observe correlations in prepared quantum states* of the double well (Chapter 7). After the expansion, we extract the position of the atoms along the double-well axis for a few thousand realizations. In this way, we obtain the full momentum distribution of the quantum state and can determine its two-particle correlations. For two identical fermions prepared in the double-well potential we observed anti-bunching with a contrast of 70%. Investigating the ground state of the Hubbard model revealed two-particle correlations that emerge when we increase the repulsion between the two fermions. In this way, we could show the creation of a strongly-correlated two-particle state that is the building block of many interesting magnetic phases [Sac08].

Assembling a many-body state

In the future, we want to assemble larger quantum many-body states in a bottom-up approach and probe their correlations. A necessary requirement towards achieving this goal is to create low-entropy systems with a high level of control on the system's parameters such as the external potential and the interaction strength. Starting with several fundamental building blocks of the Hamiltonian of interest, we want to adiabatically merge them to form a mesoscopic state. In particular, we are interested in studying the crossover from few- to many-body physics.

One of the most prominent Hamiltonians, which we want to explore, is the Hubbard model. As Lieb pointed out [Lie89], the ground state of this model is non-degenerate and has a total spin zero. Therefore, it can be constructed by assembling pairs of fermions that form spin singlets. In [Mur15b] we demonstrated the preparation of such a fundamental building block where the spin singlet is spread over the two wells. By preparing several double-well potential containing two spin singlet states with non-local correlation and slowly coupling the double-well systems, we may be able to adiabatically ramp into the non-degenerate ground state of a few-site Hubbard model [Mat01, Lub11].

Another fascinating possibility using our bottom-up approch is to realize bi-layered systems. For preparing the fundamental building block of such bilayered systems, one would start with two optical tweezers that are both filled with two atoms forming a spin singlet state. By increasing the interaction strength to the limit, where the two particles fermionize and simulaneously coupling the two wells, the coupling within the wells could be reduced below the inter-well coupling. Consequently, the singlet correlation could be transferred to particles on different wells. In a similar way as the Hubbard model, one could then prepare an array of coupled wells filled with two fermions each and explore many-body phases of strongly correlated bilayered systems.

Measuring correlations in the many-body state

To probe the deterministically prepared mesoscopic states, we will use the single-atom imaging developed in this thesis. Its capability to detect many atoms with spin resolution enables us to probe many-body systems on the single-atom level and thus determine the full set of correlation functions that characterize the quantum state.

The imaging technique is also suited to measure momentum correlation in two dimensions. This can be achieved by allowing the quantum state to evolve in a radially symmetric two-dimensional harmonic confinement. With this, we have a tool to measure correlations for instance in states confined in finite 2D-arrays.

Due to its simplicity, one can implement the imaging scheme in any ^{6}Li system that features a high-resolution objective and EMCCD camera. Currently, we work on its implementation in the second setup present in our group which soon also offers the possibility to create arbitrary multi-well potentials with a spatial light modulator [Hol14].

Appendix A

Properties of Lithium-6
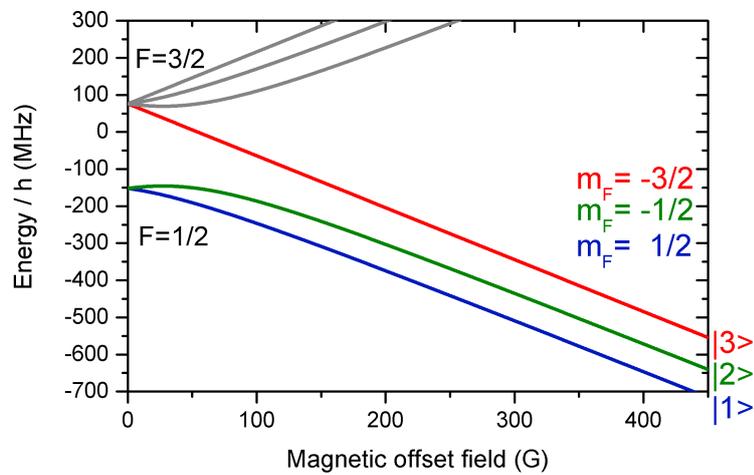
Figure A.1: Energy splitting of the $2S_{1/2}$ ground state manifold as a function of the magnetic offset field. Around $50\,\mathrm{G}$ the electron spin and the nuclear spin $I = 1$ start to decouple. At fields of a few $100\,\mathrm{G}$, the energy differences between the three lowest hyperfine states $|1\rangle$, $|2\rangle$ and $|3\rangle$ are around $80\,\mathrm{MHz}$.
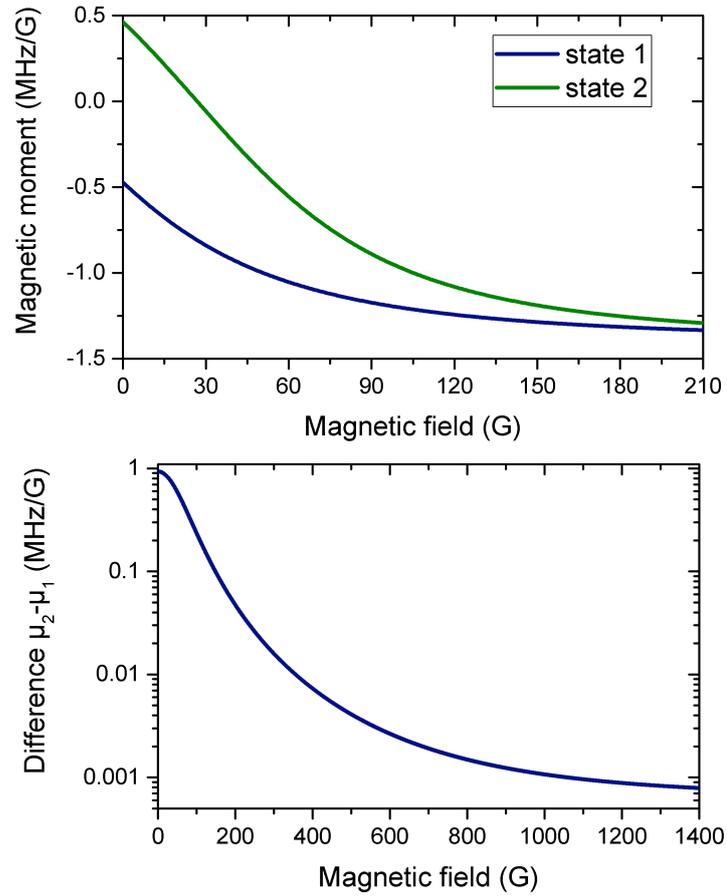
Figure A.2: Magnetic moments (top) and difference between the magnetic moments (bottom) of the hyperfine state $|1\rangle$ and $|2\rangle$. Note that state $|3\rangle$ is a stretched state. Therefore, its magnetic moment is $\mu_{|3\rangle} = -1.4\text{MHz/G}$ and constant.

Appendix B

Experimental parameters

In the course of this thesis, the high-resolution objective had been taken out of the setup several times. For this reason, the trap parameters for the different measurements vary. In the following, the measured and calculated parameters for the different experiments are listed.

B.1 Microtrap parameters

The trap frequencies of the microtrap are measured by parametric heating. To calculate the waist of the microtrap, we compare the measured frequencies with a harmonic approximation of a Gaussian beam.

Microtrap parameters

Parameter	microtrap
measured light power	$(393 \pm 39)\mu\mathrm{W}$
axial frequency ω_{ax}	$\approx 2\pi \times 2.45$ kHz
radial frequency ω_{rad}	$\approx 2\pi \times 16.5$ kHz
aspect ratio η	≈ 7
calculated trap depth V_0	$4.8\mu\mathrm{K}$
calculated waist w_0	$1.65\mu\mathrm{m}$

Table B.1: Microtrap parameters for the experiments presented in Chapter 5 and Chapter 6.

B.2 Quasi-particle residue measurement

Data at weak interaction

Magnetic offset field $B = 589.79$G
Interaction strength $g_{1D} = 0.31355\,\hbar\omega_z a_z$ with $a_z = \sqrt{\hbar/m\omega_z}$

N	ΔE_{int} (Hz)	Ω_N (Hz)	Residue Z
$N = 0$	0 ± 11.21964	3675.00 ± 0.68	$1 \pm 5.23 \times 10^{-4}$
$N = 1$	305.64872 ± 13.28445	3666.12 ± 0.74	$0.99517 \pm 5.45 \times 10^{-4}$
$N = 2$	499.5927 ± 19.17654	3667.00 ± 0.38	$0.99565 \pm 4.22 \times 10^{-4}$
$N = 3$	669.54058 ± 20.04709	3669.60 ± 0.73	$0.99706 \pm 5.42 \times 10^{-4}$

Data at medium interaction

Magnetic offset field $B = 634.84$G
Interaction strength $g_{1D} = 2.43243\,\hbar\omega_z a_z$
Interaction strength $g_{1D} = 0.29965\,\hbar\omega_z a_z$

N	ΔE_{int} (Hz)	Ω_N (Hz)	Residue Z
$N = 0$	0 ± 6.22408	3456.57 ± 0.74	$1 \pm 6.06 \times 10^{-4}$
$N = 1$	1230.7315 ± 15.0017	3282.28 ± 0.4	$0.9017 \pm 4.44 \times 10^{-4}$
$N = 2$	2216.31667 ± 21.15275	3290.42 ± 0.62	$0.90617 \pm 5.17 \times 10^{-4}$

B.3 Parameters for the realization of the fundamental building block

Parameters of the tunnel coupling

Parameter	Overall light power 1.5V	Overall light power 1.0V
Overall light power	$(200 \pm 20)\mu$W	$(130 \pm 13)\mu$W
measured tunnel coupling J	(67.3 ± 0.5)Hz	(142.0 ± 0.5)Hz
calculated axial trap frequency	1.23kHz	1.0kHz
calculated axial trap frequency	18 J	7 J

Table B.2: Double well parameters for the experiments presented in Chapter 6. The two microtraps had a distance of $d \approx 2\mu$m.

Measured on-site interaction

B(G)	$a_{\mathrm{sc}}(\lvert 1\rangle \lvert 2\rangle)$	$-1/g_{\mathrm{1D}}$	U/J	$U/\hbar\omega_{\mathrm{ax}}$
300	-288.1a_0	8.82 ± 0.23	-1.41 ± 0.25	-0.08 ± 0.01
560	131.8 a_0	-18.35 ± 0.46	0.67 ± 0.18	0.04 ± 0.01
600	359.9 a_0	-6.54 ± 0.16	1.37 ± 0.21	0.08 ± 0.01
640	699.9 a_0	-3.22 ± 0.08	3.3 ± 0.12	0.18 ± 0.01
700	1637.1a_0	-1.21 ± 0.03	6.32 ± 0.09	0.35 ± 0.01
740	2973.9 a_0	-0.54 ± 0.01	10.26 ± 0.10	0.56 ± 0.01

Table B.3: On-site interaction for the total light power $P_{\mathrm{tot}} = 1.5$V.

B(G)	$a_{\mathrm{sc}}(\lvert 1\rangle \lvert 2\rangle)$	$-1/g_{\mathrm{1D}}$	U/J	$U/\hbar\omega_{\mathrm{ax}}$
300	-288.1a_0	9.72 ± 0.24	-0.20 ± 0.22	-0.03 ± 0.03
620	512.0 a_0	-5.01 ± 0.16	0.71 ± 0.33	0.10 ± 0.04
700	1637.1a_0	-1.37 ± 0.03	2.31 ± 0.21	0.33 ± 0.03
740	2973.9 a_0	-0.62 ± 0.01	3.46 ± 0.22	0.49 ± 0.03

Table B.4: On-site interaction for the total light power $P_{\mathrm{tot}} = 1.0$V.

B.4 Parameters for the correlation measurements

Trap parameters of the microtrap

Parameter	microtrap
measured light power	$(338 \pm 34)\mu$W
axial frequency ω_{ax}	$\approx 2\pi \times (6.09 \pm 0.04)$ kHz
radial frequency $\omega_{\mathrm{rad},1}$	$\approx 2\pi \times (29.9 \pm 0.04)$ kHz
radial frequency $\omega_{\mathrm{rad},2}$	$\approx 2\pi \times (30.44 \pm 0.07)$ kHz
aspect ratio η	4.9
calculated trap depth V_0	8.4μK
calculated waist w_0	1.16μm

Parameters of the tunnel coupling

Parameter	Overall light power 0.8V	Overall light power 1.0V
Overall light power	$(208 \pm 21)\mu$W	$(260 \pm 26)\mu$W
depth of potential V_0	$\approx 2.6\mu$K	$\approx 3.3\mu$K
measured tunnel coupling J	≈ 250Hz	≈ 100Hz
calculated axial trap frequency	3.2kHz	3.7kHz
calculated axial trap frequency	13 J	37 J

Calculated on-site interaction

B(G)	$a_{\mathrm{sc}}(\vert 1\rangle \vert 3\rangle)$	$-1/g_{\mathrm{1D}}$	U/J	$U/\hbar\omega_{\mathrm{ax}}$
600	584.1 a_0	-3.03 ± 0.16	2.1 ± 0.21	0.164 ± 0.01
620	1233 a_0	-1.26 ± 0.08	4.3 ± 0.43	0.334 ± 0.03
640	2414.3 a_0	-0.48 ± 0.08	7.7 ± 0.77	0.594 ± 0.06
655	4203.2 a_0	-0.13 ± 0.08	11.1 ± 1.1	0.857 ± 0.09

Table B.5: Calculated on-site interaction for the total light power $P_{\mathrm{tot}} = 0.8$V.

Bibliography

[Alb16] A. Alberti, C. Robens, W. Alt, S. Brakhane, M. Karski, R. Reimann, A. Widera, D. Meschede, *Super-resolution microscopy of single atoms in optical lattices*, New Journal of Physics **18**(5), 053010 (2016).

[Alt04] E. Altman, E. Demler, M. D. Lukin, *Probing many-body states of ultracold atoms via noise correlations*, Physical Review A - Atomic, Molecular, and Optical Physics **70**(1) (2004).

[And50] P. W. Anderson, *Antiferromagnetism. Theory of superexchange interaction*, Physical Review **79**(2), 350 (1950).

[And67] P. W. Anderson, *Infrared catastrophe in fermi gases with local scattering potentials*, Physical Review Letters **18**(24), 1049–1051 (1967).

[And97] M. R. Andrews, C. G. Townsend, H. J. Miesner, D. S. Durfee, D. M. Kurn, W. Ketterle, *Observation of interference between two {Bose-Einstein} condensates*, Science **275**(5300), 637–641 (1997).

[And07] M. Anderlini, P. J. Lee, B. L. Brown, J. Sebby-Strabley, W. D. Phillips, J. V. Porto, *Controlled exchange interaction between pairs of neutral atoms in an optical lattice.*, Nature **448**(7152), 452–6 (jul 2007).

[Arn99] M. Arndt, O. Nairz, J. Vos-Andreae, C. Keller, G. van der Zouw, a. Zeilinger, *Wave-particle duality of C(60) molecules.*, Nature **401**(6754), 680–2 (oct 1999).

[Aue98] A. Auerbach, *Interacting Electrons and Quantum Magnetism* (Springer, New York, 1998).

[Bak09] W. S. Bakr, J. I. Gillen, A. Peng, S. Fölling, M. Greiner, *A quantum gas microscope for detecting single atoms in a Hubbard-regime optical lattice.*, Nature **462**(7269), 74–77 (2009).

[Bay98] G. Baym, *The physics of hanbury brown-twiss intensity interferometry: From stars to nuclear collisions*, Acta Physica Polonica B **29**(7), 1839–1884 (1998).

[Bec16] J. H. W. Becher, *Towards Spin and Site-Resolved, Single-Atom Imaging of 6Li Atoms in a Multiwell Potential*, Master thesis, Heidelberg University (2016).

[Bel64] J. S. Bell, *On the Einstein Podolsky Rosen paradox* (1964).

[Ber03] T. Bergeman, M. Moore, M. Olshanii, *Atom-Atom Scattering under Cylindrical Harmonic Confinement: Numerical and Analytic Studies of the Confinement Induced Resonance*, Physical Review Letters **91**(16), 163201 (oct 2003).

[Ber13] A. Bergschneider, *Ultracold few-fermi systems in multiwell potentials*, Master thesis, University of Heidelberg (2013).

[Blo05] I. Bloch, *Ultracold quantum gases in optical lattices*, Nature Physics **1**, 23–30 (2005).

[Blu01] S. Blundell, *Magnetism in condensed matter physics* (Oxford University Press USA, Oxford, 2001).

[Bol16] M. Boll, T. A. Hilker, G. Salomon, A. Omran, J. Nespolo, L. Pollet, I. Bloch, C. Gross, *Spin- and density-resolved microscopy of antiferromagnetic correlations in Fermi-Hubbard chains*, Science **353**(6305), 1257–1260 (2016).

[Bom17] P. L. Bommer, *Identification and Localization of Single Atoms in Fluorescence Images based on Image Processing*, Bachelor thesis, University of Heidelberg (2017).

[Bro13] I. Brouzos, P. Schmelcher, *Two-component few-fermion mixtures in a one-dimensional trap: Numerical versus analytical approach*, Physical Review A - Atomic, Molecular, and Optical Physics **87**(2) (2013).

[Büc09] R. Bücker, A. Perrin, S. Manz, T. Betz, C. Koller, T. Plisson, J. Rottmann, T. Schumm, J. Schmiedmayer, *Single-particle-sensitive imaging of freely propagating ultracold atoms*, New Journal of Physics **11**(10), 103039 (2009).

[Bus98] T. Busch, *Two Cold Atoms in a Harmonic Trap*, Foundations of Physics **28**, 549–559 (1998).

[Cam14] S. Campbell, M. Angel, T. Busch, *Quenching small quantum gases: Genesis of the orthogonality catastrophe* ´ 1–6 (2014).

[Che12] M. Cheneau, P. Barmettler, D. Poletti, M. Endres, P. Schauß, T. Fukuhara, C. Gross, I. Bloch, C. Kollath, S. Kuhr, *Light-cone-like spreading of correlations in a quantum many-body system*, Nature **481**(7382), 484–487 (2012).

[Che15] L. W. Cheuk, M. A. Nichols, M. Okan, T. Gersdorf, V. V. Ramasesh, W. S. Bakr, T. Lompe, M. W. Zwierlein, *Quantum-gas microscope for fermionic atoms*, Physical Review Letters **114**(19) (2015).

[Chi05] C. Chin, P. S. Julienne, *Radio-frequency transitions on weakly bound ultracold molecules*, Phys. Rev. A **71**(1), 12713 (jan 2005).

[Chi10] C. Chin, R. Grimm, P. Julienne, E. Tiesinga, *Feshbach Resonances in Ultracold Gases*, Reviews of Modern Physics **82**, 1225 (2010).

[CT11] C. Cohen-Tannoudji, D. Guéry-Odelin, *Advances in atomic physics: an overview* (World Scientific, 2011).

[Dai10] O. Daigle, P.-O. Quirion, S. Lessard, *The darkest EMCCD ever*, in *SPIE High Energy Optical and Infrared Detectors for Astronomy IV*, Vol. 7742 (2010).

[Dal99] J. Dalibard, *Collisional dynamics of ultra-cold atomic gases*, Proceedings of the International School of Physics- . . . 1–29 (1999).

[Deh16] M. Dehabe, *Creating an optical microtrap with tunable aspect ratio for ultracold fermions*, Master thesis, University of Heidelberg (2016).

[DeM10] D. DeMille, D. Budker, D. F. Kimball, *Atomic physics: an exploration through problems and solutions* (Oxford University Press, 2010).

[Deu14] F. Deuretzbacher, D. Becker, J. Bjerlin, S. M. Reimann, L. Santos, *Quantum magnetism without lattices in strongly interacting one-dimensional spinor gases*, Physical Review A - Atomic, Molecular, and Optical Physics **90**, 1–11 (2014).

[Edg15] G. J. A. Edge, R. Anderson, D. Jervis, D. C. McKay, R. Day, S. Trotzky, J. H. Thywissen, *Imaging and addressing of individual fermionic atoms in an optical lattice*, Physical Review A - Atomic, Molecular, and Optical Physics **92**(6) (2015).

[FA03] S. Franke-Arnold, S. M. Barnett, G. Huyet, C. Sailliot, *Coherence properties of two trapped particles*, European physical Journal D **383**(22), 373–383 (2003).

[Fan16] B. Fang, A. Johnson, T. Roscilde, I. Bouchoule, *Momentum-space correlations of a one-dimensional Bose gas*, Physical review letters **116**(5), 050402 (2016).

[Fey82] R. P. Feynman, *Simulating physics with computers*, International Journal of Theoretical Physics **21**(6-7), 467–488 (1982).

[Föl07] S. Fölling, S. Trotzky, P. Cheinet, M. Feld, R. Saers, A. Widera, T. Müller, I. Bloch, *Direct observation of second-order atom tunnelling.*, Nature **448**(7157), 1029–32 (aug 2007).

[Föl14] S. Fölling, *Quantum Noise Correlation Experiments with Ultracold Atoms*, arXiv preprint 26 (2014).

[Foo11] C. J. Foot, M. D. Shotter, *Double well potentials and quantum gates*, American Journal of Physics **79**(7), 762–768 (2011).

[För15] J. Förste, *The AC-Stark shift of Lithium-6 in a dipole trap*, Bachelor thesis, University of Heidelberg (2015).

[Fox06] M. Fox, *Quantum optics: an introduction*, Vol. 15 (OUP Oxford, 2006).

[Fö05] S. Fölling, F. Gerbier, A. Widera, O. Mandel, T. Gericke, I. Bloch, *Spatial quantum noise interferometry in expanding ultracold atom clouds*, Nature **434**(2005), 481–484 (2005).

[Geh03] M. E. Gehm, *Properties of 6 Lithium*, Dep. of Physics, DUKE University http://www. phy. duke. edu/research/photon/qoptics/ techdocs/pdf/PropertiesOfLi.pdf **21** (2003).

[Gha12] S. E. Gharashi, K. M. Daily, D. Blume, *Three s-wave-interacting fermions under anisotropic harmonic confinement: Dimensional crossover of energetics and virial coefficients*, Physical Review A - Atomic, Molecular, and Optical Physics **86**(4) (2012).

[Gha13] S. E. Gharashi, D. Blume, *Correlations of the Upper Branch of 1D Harmonically Trapped Two-Component Fermi Gases*, Physical Review Letters **111**(4), 045302 (jul 2013).

[Gha14] S. E. Gharashi, X. Y. Yin, D. Blume, *Molecular branch of a small highly elongated Fermi gas with an impurity: Full three-dimensional versus effective one-dimensional description*, Physical Review A - Atomic, Molecular, and Optical Physics **89**(2) (2014).

[Gha15] S. E. Gharashi, X. Y. Yin, Y. Yan, D. Blume, *One-dimensional Fermi gas with a single impurity in a harmonic trap: Perturbative description of the upper branch*, Physical Review A **91**(1), 013620 (jan 2015).

[Gir60] M. Girardeau, *Relationship between Systems of Impenetrable Bosons and Fermions in One Dimension*, Journal of Mathematical Physics **1**(6), 516 (1960).

[Gir10] M. Girardeau, *Two super-Tonks-Girardeau states of a trapped one-dimensional spinor Fermi gas*, Physical Review A **82**, 1–4 (2010).

[Gla62] R. J. Glauber, *Photon Correlations*, Proc. Roy. Soc. (London) A238 Chap. II Phil. Trans. Roy. Soc. London A250 **9**(9), 289–89 (1962).

[Gla63a] R. Glauber, *The quantum theory of optical coherence*, Physical Review **130**(6), 2529–2539 (1963).

[Gla63b] R. J. Glauber, *Coherent and Incoherent States of the Radiation Field*, Phys. Rev. A **49**(638) (1963).

[Goo11] J. Goold, T. Fogarty, N. Lo Gullo, M. Paternostro, T. Busch, *Orthogonality catastrophe as a consequence of qubit embedding in an ultracold Fermi gas*, Physical Review A - Atomic, Molecular, and Optical Physics **84**(6), 1–6 (2011).

[Gre02] M. Greiner, O. Mandel, T. Esslinger, T. W. Hänsch, I. Bloch, *Quantum phase transition from a superfluid to a Mott insulator in a gas of ultracold atoms*, Nature **415**(6867), 39–44 (2002).

[Gre05] M. Greiner, C. A. Regal, J. T. Stewart, D. S. Jin, *Probing pair-correlated fermionic atoms through correlations in atom shot noise*, Physical Review Letters **94**(11), 1–4 (2005).

[Gre11] D. Greif, L. Tarruell, T. Uehlinger, R. Jördens, T. Esslinger, *Probing nearest-neighbor correlations of ultracold fermions in an optical lattice*, Physical Review Letters **106**(14) (2011).

[Gre16] D. Greif, M. F. Parsons, A. Mazurenko, C. S. Chiu, S. Blatt, F. Huber, G. Ji, M. Greiner, *Site-resolved imaging of a fermionic Mott insulator*, Science **351**(6276), 953–957 (2016).

[Gri00] R. Grimm, M. Weidemüller, Y. B. Ovchinnikov, *Optical Dipole traps for neutral atoms*, Advances in atomic, molecular, and optical physics **42**, 95–170 (2000).

Bibliography

[Gro99] J. Grondalski, P. Alsing, I. Deutsch, *Spatial correlation diagnostics for atoms in optical lattices.*, Optics express **5**(11), 249–261 (1999).

[Gua09] L. Guan, S. Chen, Y. Wang, Z. Q. Ma, *Exact solution for infinitely strongly interacting fermi gases in tight waveguides*, Physical Review Letters **102**(16), 1–4 (2009).

[Gua13] X.-W. Guan, M. T. Batchelor, C. Lee, *Fermi gases in one dimension: From Bethe ansatz to experiments*, Reviews of Modern Physics **85**(4), 1633 (2013).

[Hal15] E. Haller, J. Hudson, A. Kelly, D. A. Cotta, B. Peaudecerf, G. D. Bruce, S. Kuhr, *Single-atom imaging of fermions in a quantum-gas microscope*, Nature Physics **11**(9), 738–742 (2015).

[Han56] R. Hanbury Brown, R. Q. Twiss, *A test of a new type of stellar interferometer on Sirius* (1956).

[Har12] K. B. W. Harpsøe, M. I. Andersen, P. Kjægaard, *Bayesian photon counting with electron-multiplying charge coupled devices (EMCCDs)*, Astronomy & Astrophysics **537**, A50 (2012).

[Har15] R. A. Hart, P. M. Duarte, T.-L. Yang, X. Liu, T. Paiva, E. Khatami, R. T. Scalettar, N. Trivedi, D. A. Huse, R. G. Hulet, *Observation of antiferromagnetic correlations in the Hubbard model with ultracold atoms*, Nature **519**(7542), 211–214 (2015).

[Hei27] W. Heitler, F. London, *Wechselwirkung neutraler Atome und homöopolare Bindung nach der Quantenmechanik*, Zeitschrift für Physik A Hadrons and Nuclei **44**(6), 455–472 (1927).

[Hir13] M. Hirsch, R. J. Wareham, M. L. Martin-Fernandez, M. P. Hobson, D. J. Rolfe, *A Stochastic Model for Electron Multiplication Charge-Coupled Devices - From Theory to Practice*, PLoS ONE **8**(1) (2013).

[Ho09] A. F. Ho, M. Cazalilla, T. Giamarchi, *Quantum simulation of the Hubbard model: The attractive route*, Physical Review A **79**(3), 033620 (mar 2009).

[Hod11] S. S. Hodgman, R. G. Dall, A. G. Manning, K. G. H. Baldwin, A. G. Truscott, *Direct Measurement of Long-Range Third-Order Coherence in Bose-Einstein Condensates*, Science **331**(6020), 1046–1049 (2011).

152

[Hod17] S. Hodgman, R. Khakimov, R. Lewis-Swan, A. Truscott, K. Kheruntsyan, Others, *Solving the quantum many-body problem via correlations measured with a momentum microscope*, arXiv preprint arXiv:1702.03617 (2017).

[Hol14] M. Holten, *Hamiltonian Engineering in Ultracold Atom Experiments using a Spatial Light Modulator*, Bachelor thesis, University of Heidelberg (2014).

[Hon87] C. K. Hong, Z.-Y. Ou, L. Mandel, *Measurement of subpicosecond time intervals between two photons by interference*, Physical Review Letters **59**(18), 2044 (1987).

[Hu94] Z. Hu, H. J. Kimble, *Observation of a single atom in a magneto-optical trap.*, Optics letters **19**(22), 1888 (1994).

[Hub63] J. Hubbard, *Electron Correlations in Narrow Energy Bands*, Proceedings of the Royal Society A: Mathematical, Physical and Engineering Sciences **276**(1365), 238–257 (nov 1963).

[Hum13] D. B. Hume, I. Stroescu, M. Joos, W. Muessel, H. Strobel, M. K. Oberthaler, *Accurate Atom Counting in Mesoscopic Ensembles* 1–5 (2013).

[Idz05] Z. Idziaszek, T. Calarco, *Two atoms in an anisotropic harmonic trap*, Physical Review A - Atomic, Molecular, and Optical Physics **71**(5), 1–4 (2005).

[Idz06] Z. Idziaszek, T. Calarco, *Analytical solutions for the dynamics of two trapped interacting ultracold atoms*, Physical Review A **74**(2), 022712 (aug 2006).

[Jak98] D. Jaksch, C. Bruder, J. I. Cirac, C. W. Gardiner, P. Zoller, *Cold bosonic atoms in optical lattices*, Physical Review Letters **81**(15), 3108–3111 (1998).

[Jak05] D. Jaksch, P. Zoller, *The cold atom Hubbard toolbox*, Annals of Physics **315**(1), 52–79 (2005).

[Jel07] T. Jeltes, J. M. McNamara, W. Hogervorst, W. Vassen, V. Krachmalnicoff, M. Schellekens, A. Perrin, H. Chang, D. Boiron, A. Aspect, C. I. Westbrook, *Comparison of the Hanbury Brown-Twiss effect for bosons and fermions.*, Nature **445**(January), 402 (2007).

[Jör08]   R. Jördens, N. Strohmaier, K. Günter, H. Moritz, T. Esslinger, *A Mott insulator of fermionic atoms in an optical lattice*, Nature **455**(7210), 204–207 (2008).

[Kau14]   A. M. Kaufman, B. J. Lester, C. M. Reynolds, M. L. Wall, M. Foss-Feig, K. R. a. Hazzard, a. M. Rey, C. a. Regal, *Two-particle quantum interference in tunnel-coupled optical tweezers.*, Science (New York, N.Y.) **306** (jun 2014).

[Kes10]   J. P. Kestner, L. M. Duan, *Effective single-band models for strongly interacting fermions in an optical lattice*, Physical Review A - Atomic, Molecular, and Optical Physics **81**(4) (2010).

[Ket99]   W. Ketterle, D. S. Durfee, D. M. Stamper-Kurn, *Making, probing and understanding Bose-Einstein condensates*, Proceedings of the International School of Physics "Enrico Fermi" 67 (1999).

[Ket08]   W. Ketterle, M. W. Zwierlein, *Making, probing and understanding ultracold Fermi gases* (June 2006), 20–30 (2008).

[Kie02]   H. Kiesel, A. Renz, F. Hasselbach, *Observation of Hanbury Brown–Twiss anticorrelations for free electrons*, Nature **418**(6896), 392–394 (2002).

[Kim77]   H. J. Kimble, M. Dagenais, L. Mandel, *Photon antibunching in resonance fluorescence*, Physical Review Letters **39**(11), 691 (1977).

[Kli12]   V. M. Klinkhamer, *An apparatus for few-fermion systems in multiple well potentials* (2012).

[Koh12]   C. Kohstall, M. Zaccanti, M. Jag, A. Trenkwalder, P. Massignan, G. M. Bruun, F. Schreck, R. Grimm, *Metastability and coherence of repulsive polarons in a strongly interacting Fermi mixture*, Nature **485**(7400), 615–618 (2012).

[Kra34]   H. A. Kramers, *L'interaction entre les atomes magnetogenes dans un cristal paramagnetique*, Physica **1**, 182–192 (1934).

[Kra15]   G. Krause, *Simultaneous absorption imaging of two Li-6 hyperfine states*, Bachelor thesis, University of Heidelberg (2015).

[Lak15]   D. Lake, *Stabilizing Light Intensity Patterns with a Camera Feedback Loop*, Bachelor thesis, University of Heidelberg (2015).

[Lan08] E. Lantz, J. L. Blanchet, L. Furfaro, F. Devaux, *Multi-imaging and Bayesian estimation for photon counting with EMCCDs*, Monthly Notices of the Royal Astronomical Society **386**(4), 2262–2270 (2008).

[Lev14] J. Levinsen, P. Massignan, G. M. Bruun, M. M. Parish, *Strong-coupling ansatz for the one-dimensional Fermi gas in a harmonic potential*, arXiv preprint arXiv:1408.7096v1 15 (2014).

[Lie89] E. H. Lieb, *Two theorems on the Hubbard model*, Physical Review Letters **62**(10), 1201–1204 (1989).

[Lie93] E. Lieb, *The Hubbard Model: Some Rigorous Results and Open Problems*, arXiv:cond-mat/9311033 **1993**, 1–20 (1993).

[Lom08] T. Lompe, *An apparatus for the production of molecular Bose-Einstein condensates*, Diploma thesis, University of Heidelberg (2008).

[Lom11] T. Lompe, *Efimov Physics in a three-component Fermi gas*, Dissertation (2011).

[Lub11] M. Lubasch, V. Murg, U. Schneider, J. I. Cirac, M. C. Bañuls, *Adiabatic preparation of a Heisenberg antiferromagnet using an optical superlattice*, Physical Review Letters **107**(16), 1–10 (2011).

[Mas15] P. Massignan, *Private communication* (2015).

[Mat01] M. Matsumoto, C. Yasuda, S. Todo, H. Takayama, *Ground-state phase diagram of quantum Heisenberg antiferromagnets on the anisotropic dimerized square lattice*, Physical Review B **65**(1), 14407 (2001).

[Maz16] A. Mazurenko, C. S. Chiu, G. Ji, M. F. Parsons, M. Kanász-Nagy, R. Schmidt, F. Grusdt, E. Demler, D. Greif, M. Greiner, *Experimental realization of a long-range antiferromagnet in the Hubbard model with ultracold atoms*, arXiv preprint arXiv:1612.08436 (2016).

[McG65] J. B. McGuire, *Interacting Fermions in One Dimension. I. Repulsive Potential*, Journal of Mathematical Physics **6**(3), 432 (1965).

[McK11] D. C. McKay, B. DeMarco, *Cooling in strongly correlated optical lattices: prospects and challenges*, Reports on Progress in Physics **74**(5), 54401 (2011).

[Met99] H. J. Metcalf, P. der Straten, *Laser cooling and trapping* (Springer Verlag, 1999).

[Mir15] M. Miranda, R. Inoue, Y. Okuyama, A. Nakamoto, M. Kozuma, *Site-resolved imaging of ytterbium atoms in a two-dimensional optical lattice*, Physical Review A - Atomic, Molecular, and Optical Physics **91**(6) (2015).

[Mur14] P. A. Murthy, D. Kedar, T. Lompe, M. Neidig, M. G. Ries, A. N. Wenz, G. Zürn, S. Jochim, *Matter-wave Fourier optics with a strongly interacting two-dimensional Fermi gas*, Phys. Rev. A **90**(4), 43611 (2014).

[Mur15a] S. Murmann, *Few-particle quantum magnetism with ultracold atoms*, Dissertation (2015).

[Mur15b] S. Murmann, A. Bergschneider, V. M. Klinkhamer, G. Zürn, T. Lompe, S. Jochim, *Two fermions in a double well: Exploring a fundamental building block of the Hubbard model*, Physical Review Letters **114**(8) (2015).

[Mur15c] S. Murmann, F. Deuretzbacher, G. Zürn, J. Bjerlin, S. M. Reimann, L. Santos, T. Lompe, S. Jochim, *Antiferromagnetic heisenberg spin chain of a few cold atoms in a one-dimensional trap*, Physical Review Letters **115**(21) (2015).

[Nie04] M. A. Nielsen, I. L. Chuang, *Quantum Computation and Quantum Information (Cambridge Series on Information and the Natural Sciences)* (2004).

[Oli99] W. D. Oliver, J. Kim, R. C. Liu, Y. Yamamoto, *Hanbury Brown and Twiss-type experiment with electrons*, Science **284**(5412), 299–301 (1999).

[Ols98] M. Olshanii, *Atomic Scattering in the Presence of an External Confinement and a Gas of Impenetrable Bosons*, Physical Review Letters **81**(5), 938–941 (aug 1998).

[Omr15] A. Omran, M. Boll, T. A. Hilker, K. Kleinlein, G. Salomon, I. Bloch, C. Gross, *Microscopic Observation of Pauli Blocking in Degenerate Fermionic Lattice Gases*, Physical Review Letters **115**(26) (2015).

[Oss14] A. Ossipov, *Entanglement entropy in Fermi gases and Anderson's orthogonality catastrophe* **130402**(September), 6 (2014).

[Ott16] H. Ott, *Single atom detection in ultracold quantum gases: a review of current progress*, Reports on Progress in Physics **79**, 054401 (2016).

[Par15] M. F. Parsons, F. Huber, A. Mazurenko, C. S. Chiu, W. Setiawan, K. Wooley-Brown, S. Blatt, M. Greiner, *Site-resolved imaging of fermionic* ^{6}Li *in an optical lattice.*, Physical review letters **114**(21), 213002 (2015).

[Per12] A. Perrin, R. Bücker, S. Manz, T. Betz, C. Koller, T. Plisson, T. Schumm, J. Schmiedmayer, *Hanbury Brown and Twiss correlations across the Bose–Einstein condensation threshold*, Nature Physics **8**(3), 195–198 (2012).

[Pre15] P. M. Preiss, R. Ma, M. E. Tai, J. Simon, M. Greiner, *Quantum gas microscopy with spin, atom-number, and multilayer readout*, Physical Review A - Atomic, Molecular, and Optical Physics **91**(4) (2015).

[Pur56] E. M. Purcell, *The question of correlation between photons in coherent light rays*, Nature **178**, 1449–1450 (1956).

[Qui09] J. Quintanilla, C. Hooley, *The strong-correlations puzzle*, Physics World **22**(6), 32–37 (2009).

[Rom06] T. Rom, T. Best, D. van Oosten, U. Schneider, S. Fölling, B. Paredes, I. Bloch, *Free fermion antibunching in a degenerate atomic Fermi gas released from an optical lattice*, Nature **444**(7120), 733–736 (2006).

[Rom09] T. Rom, *Bosonische und fermionische Quantengase in dreidimensionalen optischen Gittern*, Dissertation, Ludwig-Maximilians-Universität München (2009).

[Sac08] S. Sachdev, *Quantum magnetism and criticality*, Nature Physics **4**(3), 173–185 (2008).

[Saf12] M. S. Safronova, U. I. Safronova, C. W. Clark, *Magic wavelengths for optical cooling and trapping of lithium*, Physical Review A **86**(4), 42505 (2012).

[Sch26] E. Schrödinger, *Quantisierung als Eigenwertproblem*, Annalen der physik **385**(13), 437–490 (1926).

[Sch05] M. Schellekens, R. Hoppeler, A. Perrin, J. V. Gomes, D. Boiron, A. Aspect, C. I. Westbrook, *Hanbury Brown Twiss Effect for Ultracold Quantum Gases*, Science **310**(5748), 648–651 (2005).

[Sch08] U. Schneider, L. Hackermüller, S. Will, T. Best, I. Bloch, T. A. Costi, R. W. Helmes, D. Rasch, A. Rosch, *Metallic and insulating phases of repulsively interacting fermions in a 3D optical lattice*, Science **322**(December), 1520–1525 (2008).

[Sch09] A. Schirotzek, C.-H. Wu, A. Sommer, M. W. Zwierlein, *Observation of Fermi Polarons in a Tunable Fermi Liquid of Ultracold Atoms*, Physical Review Letters **102,**, 230402 (2009).

[Sch17] T. Schweigler, I. Kasper, Valentin Erne, Sebastian Mazets, B. Rauer, T. Cataldini, Federica Langen, T. Gasenzer, J. Berges, J. Schmiedmayer, *Experimental characterization of a quantum many-body system via higher-order correlations*, Nature **545**(7654), 323–326 (2017).

[Ser07] F. Serwane, *The setup of a magneto optical trap for the preparation of a mesoscopic degenerate fermi gas*, Diploma thesis, University of Heidelberg (2007).

[Ser11a] F. Serwane, *Deterministic preparation of a tunable few-fermion system*, Dissertation, Ruperto-Carola-University of Heidelberg, Germany (2011).

[Ser11b] F. Serwane, G. Zürn, T. Lompe, T. B. Ottenstein, A. N. Wenz, S. Jochim, *Deterministic preparation of a tunable few-fermion system*, Science **332**(6027), 336–338 (2011).

[She10] J. F. Sherson, C. Weitenberg, M. Endres, M. Cheneau, I. Bloch, S. Kuhr, *Single-atom-resolved fluorescence imaging of an atomic Mott insulator*, Nature **467**(7311), 68–72 (2010).

[SK98] D. M. Stamper-Kurn, H.-J. Miesner, A. P. Chikkatur, S. Inouye, J. Stenger, W. Ketterle, *Reversible Formation of a Bose-Einstein Condensate*, Phys. Rev. Lett. **81**(11), 2194–2197 (sep 1998).

[Sow13] T. Sowiński, T. Grass, O. Dutta, M. Lewenstein, *Few interacting fermions in a one-dimensional harmonic trap*, Physical Review A **88**(3), 033607 (sep 2013).

[Ste16] T. Steinle, *Implementation of Simultaneously Imaging two Hyperfine States of Ultracold 6Li Atoms in a Magnetic Field*, Bachelor thesis, University of Heidelberg (2016).

[Tho16] L. J. Thormählen, *Implementation of a Versatile Digital Laser Lock for Imaging Ultracold Lithium*, Bachelor thesis, University of Heidelberg (2016).

[Ton89]   A. Tonomura, J. Endo, T. Matsuda, T. Kawasaki, H. Ezawa, *Demonstration of single-electron buildup of an interference pattern*, American Journal of Physics **57**(2), 117–120 (1989).

[Tro08]   S. Trotzky, P. Cheinet, S. Fölling, M. Feld, U. Schnorrberger, a. M. Rey, A. Polkovnikov, E. a. Demler, M. D. Lukin, I. Bloch, *Time-resolved observation and control of superexchange interactions with ultracold atoms in optical lattices.*, Science (New York, N.Y.) **319**(5861), 295–9 (jan 2008).

[Tro10]   S. Trotzky, Y.-A. Chen, U. Schnorrberger, P. Cheinet, I. Bloch, *Controlling and detecting spin correlations of ultracold atoms in optical lattices*, Physical review letters **105**(26), 265303 (2010).

[Vol14]   A. G. Volosniev, D. V. Fedorov, A. S. Jensen, M. Valiente, N. T. Zinner, *Strongly interacting confined quantum systems in one dimension*, Nature Communications **5**, 5300 (2014).

[Wen13a] A. N. Wenz, *From Few to Many: Ultracold Atoms in Reduced Dimensions*, Dissertation, Ruperto-Carola-University of Heidelberg (2013).

[Wen13b] A. N. Wenz, G. Zürn, S. Murmann, I. Brouzos, T. Lompe, S. Jochim, *From Few to Many: Observing the Formation of a Fermi Sea One Atom at a Time*, Science **342**(6157), 457–460 (2013).

[Yan67]   C.-N. Yang, *Some exact results for the many body problems in one dimension with repulsive delta function interaction*, Phys. Rev. Lett. **19**(23), 1312–1314 (1967).

[You02]   T. Young, *The Bakerian Lecture: On the Theory of Light and Colours.* (Philosophical Transactions of the Royal Society of London., London, 1802), 92th Edn.

[Zim11]   B. Zimmermann, T. Mueller, J. Meineke, T. Esslinger, H. Moritz, *High-resolution imaging of ultracold fermions in microscopically tailored optical potentials*, New Journal of Physics **13**(4), 43007 (2011).

[Zür09]   G. Zürn, *Realization of an optical microtrap for a highly degenerate fermi gas*, Diploma thesis, University of Heidelberg (2009).

[Zür13]   G. Zürn, A. N. Wenz, S. Murmann, A. Bergschneider, T. Lompe, S. Jochim, *Pairing in few-fermion systems with attractive interactions*, Physical Review Letters **111**(17) (2013).

[Zü12a]   G. Zürn, *Few-fermion systems in one dimension*, Dissertation, Ruperto-Carola-University of Heidelberg (2012).

[Zü12b]   G. Zürn, F. Serwane, T. Lompe, A. N. Wenz, M. G. Ries, J. E. Bohn, S. Jochim, *Fermionization of two distinguishable fermions*, Phys. Rev. Lett. (November 2012).

[Zü13]   G. Zürn, T. Lompe, A. N. Wenz, S. Jochim, P. S. Julienne, J. M. Hutson, *Precise Characterization of* ^{6}*Li Feshbach Resonances Using Trap-Sideband-Resolved RF Spectroscopy of Weakly Bound Molecules*, Phys. Rev. Lett. **110**, 135301 (Mar 2013).

Danksagung

An dieser Stelle möchte ich bedanken bei all den Menschen, die mich in den letzten Jahren begleitet haben. Durch Eure Motivation und Eure Unterstützung habt Ihr wesentlich zum Gelingen dieser Arbeit beigetragen. Vielen Dank!

Besonders bedanke ich mich bei *Selim* für die exzellente Betreuung meiner Doktorarbeit. Deine Begeisterung an der Physik hat mich von Anfang an angesteckt und über so manche Unwegsamkeit gebracht und die zahlreichen Diskussionen haben mich immer wieder inspirierend.

Ganz herzlich bedanke ich mich bei meinen Kollegen vom alten Experiment *Thomas, Gerhard, Simon, Vincent, Jan Hendrik, Michael, Jonathan, Lennert, Alexander, Philine, Marius, Justin* und nicht zuletzt unser neuer PostDoc *Philipp*. Ihr seid mit mir in den letzten Jahren durch dick und dünn gegangen. Zusammen haben wir fünf Mal die Feshbachspulen repariert, 200ml öliges Wasser aus dem Viewport geholt, einen 200 Watt Laser ausgetauscht und beim Paperschreiben geschwitzt. Und wir haben aufregende Momente im Labor erlebt als alles wieder funktioniert hat und wir interessante Daten nehmen konnten. Weiterhin danke ich den ehemaligen Mitgliedern am alten Experiment *Timo Ottenstein* und *Friedhelm Serwane* für die exzellente Vorarbeit.

Beim Team vom neuen Experiment *Martin, Andre, Puneet, Mathias, Luca, Dhruv, Sebastian, Ralf, Marvin, Georg, Rodrigo, Benjamin, Peter und Thomas* bedanke ich mich für die interessanten Diskussionen und so mancher Experise, die in das alte Labor migriert ist.

Der ganzen Gruppe danke ich für die tolle Atmosphäre und den vielen Spaß, den wir zusammen hatten beim Bauen von rauchenden Doktorhüten, beim Pizza backen im Akkord, interessanten Diskussionen und entspannenden Kaffeepausen und den vielen Tischkickerspielen, Grillparties, außergewöhnlichen Gruppen retreats und schönen gemeinsamen Abenden.

Besonderen Dank gilt *Philipp, Vincent, Ralf, Puneet, Julia* und *Uli* für das Korrekturlesen dieser Arbeit.

Bei *Markus Oberthaler* möchte ich mich für die Übernahme der Zweitkorrektur bedanken. *Tilman Enss* und *Peter Bachert* danke ich für die Bereitschaft Teil meines Prüfungskomitees zu sein.

Das zuverlässige Funktionieren des Experiments ist nicht zuletzt den präzise gefertigten und robusten Teilen aus der *Mechanischen Werkstatt* um *Herrn Ziegler*

Erklärung:

Ich versichere, dass ich diese Arbeit selbstständig verfasst habe und keine anderen als die angegebenen Quellen und Hilfsmittel benutzt habe.

Heidelberg, den (Datum) . . . .